2016

Impact of Gamma-Irradiation on the Characteristics of III-N/GaN Based High Electron Mobility Transistors

Anupama Yadav
University of Central Florida

IMPACT OF GAMMA-IRRADIATION ON THE CHARACTERISTICS OF III-N/GaN BASED HIGH ELECTRON MOBILITY TRANSISTORS

by

ANUPAMA YADAV
B.Sc., University of Delhi, 2007
M.Sc., Indian Institute of Technology, 2010
M.S., University of Central Florida, 2012

A dissertation submitted in partial fulfillments of the requirements
for the degree of Doctor of Philosophy
in the Department of Physics
in the College of Sciences
at the University of Central Florida
Orlando, Florida

Summer Term
2016

Major Professor: Elena Flitsiyan
Leonid Chernyak

ABSTRACT

In this study, the fundamental properties of AlGaN/GaN based High Electron Mobility Transistors (HEMTs) have been investigated in order to optimize their performance in radiation harsh environment. AlGaN/GaN HEMTs were irradiated with ^{60}Co gamma-rays to doses up to 1000 Gy, and the effects of irradiation on the devices' transport and optical properties was analyzed. Understanding the radiation affects in HEMTs devices, on carrier transport, recombination rates and traps creation play a significant role in development and design of radiation resistant semiconductor components for different applications.

Electrical testing combined with temperature dependent Electron Beam Induced Current (EBIC) that we used in our investigations, provided critical information on defects induced in the material because of gamma-irradiation. It was shown that low dose (below ~250 Gy) and high doses (above ~250 Gy) of gamma-irradiation affects the AlGaN/GaN HEMTs due to different mechanisms. For low doses of gamma-irradiation, the improvement in minority carrier diffusion length is likely associated with the irradiation-induced growing lifetime of the non-equilibrium carriers. However, with the increased dose of irradiation (above ~ 250 Gy), the concentration of point defects, such as nitrogen vacancies, as well as the complexes involving native defects increases which results in the non-equilibrium carrier scattering. The impact of defect scattering is more pronounced at higher radiation, which leads to the degradation in the mobility and therefore the diffusion length. In addition for each device under investigation, the temperature dependent minority carrier diffusion length measurements were carried out. These measurements allowed the extraction of the activation energy for the temperature-induced enhancement of the minority carrier transport, which (activation energy) bears a signature of defect levels involved

the carrier recombination process. Comparing the activation energy before and after gamma-irradiation identified the radiation-induced defect levels and their dependences.

To complement EBIC measurements, spatially resolved Cathodoluminescence (CL) measurements were carried out at variable temperatures. Similar to the EBIC measurements, CL probing before and after the gamma-irradiation allowed the identification of possible defect levels generated as a result of gamma-bombardment. The observed decrease in the CL peak intensity after gamma-irradiation provides the direct evidence of the decrease in the number of recombination events. Based on the findings, the decay in the near-band-edge intensity after low-dose of gamma-irradiation (below ~250 Gy) was explained as a consequence of increased non-equilibrium carrier lifetime. For high doses (above ~250 Gy), decay in the CL intensity was observed to be related to the reduction in the mobility of charge carriers. The results of EBIC are correlated with the CL measurements in order to demonstrate that same underlying process is responsible for the changes induced by the gamma-irradiation.

DC current-voltage measurements were also conducted on the transistors to assess the impact of gamma-irradiation on transfer, gate and drain characteristics. Exposure of AlGaN/GaN HEMTs to high dose of ^{60}Co gamma-irradiation (above ~ 250 Gy) resulted in significant device degradation. Gamma-rays doses up to 1000 Gy are shown to result in positive shift in threshold voltage, a reduction in the drain current and transconductance due to increased trapping of carriers and dispersion of charge. In addition, a significant increase in the gate leakage current was observed in both forward and reverse directions after irradiation.

Post-irradiation annealing at relatively low temperature was shown to restore the minority carrier transport as well as the electrical characteristics of the devices. The level of recovery of

gamma-irradiated devices after annealing treatment depends on the dose of the irradiation. The devices that show most recovery for a particular annealing temperature are those exposed to the low doses of gamma-irradiation, while those exposed to the highest doses results in no recovery of performance. The latter fact indicates that a higher device annealing temperature is needed for larger doses of gamma-irradiation.

To my family and my husband Jitender Yadav

ACKNOWLEDGMENTS

First, I wish to express my sincere appreciation to my supervisors, Dr. Elena Flitsiyan and Dr. Leonid Chernyak, for their constant guidance and encouragement. It was due to Dr. Flitsiyan's valuable guidance, cheerful enthusiasm and ever friendly nature that I was able to complete my research work in a respectable manner. I am also very grateful to Dr. Leonid Chernyak, who has put his valuable experience and wisdom at my work. I hold deep admiration for their high standards in every aspect of their work, for heartfelt concern for their students and for boundless patience they have shown me during my research work.

I would also like to thank my committee member, Dr. Robert Peale, for providing me assistance and helpful feedback. Over the years, he has given me lot of scientific guidance, many insightful suggestions and demonstrated a sincere interest in my work. I would always be grateful to him for letting me use his lab machinery whenever I needed.

Thanks to my father, Om Parkash Yadav, for encouraging me in all of my pursuits and supporting me to follow my dreams. You are my inspiration and motivation for continuing my knowledge and move my career forward. I always knew that you believed in me and wanted the best for me. Also, I express my thanks to my younger brother and mother, who helps me through hard times and always manage to put a smile on my face. I also like to express my gratitude to my family in-law for their encouragement and continued support over the last year.

Very special thanks to my best friend, Broc Scaramella, who has offered me unlimited encouragement and unconditional love. You are always around me when I need you, always willing to listen when I need to talk, and always ready to organize something fun when I need a

break. I admire you for giving me the friendship and strength that I needed while working on my thesis. You have made the world a better place for me, just by being in it.

I would like to thank my former group member, Dr. Casey Schwarz, who always made time to help and instruct me. It is my fortune to gratefully acknowledge the support of my friends, Mahtab Khan, Neha Kohli, Udai Bhanu, Smita Sahu and Rahul Kapoor for their support and generous care throughout the research tenure. They were always beside me during the happy and the hard moments to push me and motivate me.

Lastly, but certainly not least, I wish to express my unfailing gratitude and love to my dearest husband, Jitender Yadav, for making my career most important priority in our lives. There are no words that can express my appreciation for all you have done and been for me. I am forever indebted to you for giving me your love and support. I am so grateful to have you as my life-partner!

TABLE OF CONTENTS

LIST OF FIGURES

LIST OF TABLES

LIST OF ABBREVIATIONS

Al	Aluminum
AlGaN	Aluminum Gallium Nitride
AlN	Aluminum Nitride
CL	Cathodoluminescence
Co	Cobalt
e	Electron
DC	Direct Current
EBIC	Electron Beam Induced Current
eV	Electron Volt
Ga	Gallium
GaAs	Gallium Arsenide
GaN	Gallium Nitride
Gy	Gray
GPa	Gigapascal
HCP	Hexagonally Closed Packed
HEMT	High Electron Mobility Transistor
K	Kelvin
MDFET	Modulation Doped Field Effect Transistors
meV	Milli Electron Volt
MeV	Mega Electron Volt
MOCVD	Metal Organic Chemical Vapor Deposition
MOVPE	Metal Organic Vapor Phase Epitaxy
L	Minority Carrier Diffusion Length
MBE	Molecular Beam Epitaxy

N	Nitrogen
P_{pz}	Piezoelectric Polarization
P	Polarization
SEM	Scanning Electron Microscope
Si	Silicon
P_{sp}	Spontaneous Polarization
Wz	Wurtzite
ZB	Zinc Blende
τ	Minority carrier life time
ρ_p	Polarization Induced Charge Density
n_s	Sheet Charge Carrier Concentration
2DEG	Two Dimensional Electron Gas

CHAPTER ONE: INTRODUCTION

1.1 Background

Group III-N semiconductor and their related alloys such as AlN, GaN and AlGaN are attractive for the development of microelectronic devices capable of reliable device operation at high temperatures and in radiation environments. The high cohesive strength of the N-Ga and N-Al bonds as well as the remarkably high thermal and mechanical stability of these compounds [1-4] result in relatively high energy threshold displacement damage (19–25 eV) [5-7]. In addition, a relatively large band gap of these materials leads to high energy threshold for the generation of the electron-hole pairs that can be induced by ionizing radiation [8]. Thus, GaN and its related alloys are ideal materials for the development of radiation hard electronic devices. They have potential to operate in radiation environments without the need for the cumbersome and expensive cooling systems and/or radiation shielding.

Among other promising, yet less developed III-N based technologies, AlGaN/GaN High Electron Mobility Transistors (HEMTs) have progressed vertiginously over the last decades towards greater levels of performance, resulting in a foreseeable deployment in satellite, military and nuclear applications, high energy physics as well as in other industrial applications requiring high speed, high output power, and high tolerance to radiation-induced degradation [9, 10]. Also, AlGaN/GaN HEMTs are capable of operating over a very wide temperature range, from cryogenic temperatures, prevailing in deep space, to temperature beyond 700 K, and thus expected to be stable in the space radiation environments.

While studies of radiation-induced defects in GaN–based devices have attracted significant interest, a limited data exists on the behavior of III-N based transistors after exposure to energetic ionizing radiation. To date, most investigations of the radiation effects in

AlGaN/GaN have employed energetic protons. These studies have consistently reported that proton irradiation results in a decrease in two-dimensional electron gas (2DEG) sheet carrier concentration and a positive threshold voltage shift with increasing proton dose [11-17]. In contrast to the behavior observed in proton irradiated HEMTs, negative threshold voltage shifts and increase in 2DEG sheet concentration have also been observed in AlGaN/GaN HEMTs after exposed to 1 MeV neutron irradiation with doses up to 2.5 x 10^{15} cm^{-2} [18].

Table 1 Summary of the prior and current state-of-the-art in radiation studies of semiconductor devices.

Device	**Material**	**Radiation exposed to / Energy**	**Dose**	**Ref.**
Memoristive Junctions	TiO_2	Gamma (~ 1 MeV)	45 Mrad 23 Mrad	[19]
EEPROM/Flash Cell	Metal-nitride-Oxide Semiconductor	Gamma (~1MeV)	1 Mrad	[20]
Implantable Floating-Gate EEPROM	Complementary metal-oxide semiconductors (CMOS)	X-rays	100 krad	[21]
Acoustic- wave resonator based radiation sensor	ZnO/SiN	Gamma (~1.2 MeV)	(20 – 200) krad	[22]
HEMT	AlGaN/GaN	Gamma	10^7 rad	[23]
HEMT	AlGaN/GaN and AlN/GaN	Electrons (10 MeV)	$5x10^{15}$ $3x10^{16}cm^{-2}$	[24]
Schottky diodes	ZnO	Protons (40 MeV)	up to $5x10^{10}cm^{-2}$	[25]
HEMT	InAlN/GaN	Protons (5MeV)	up to $2x10^{15}cm^{-2}$	[26]
HEMT	AlGaN/GaN	Protons (40 MeV)	up to $5x10^{10}cm^{-2}$	[27, 28]
HBT	InGaP/GaAs	Protons (40 MeV)	up to $5x10^{9}cm^{-2}$	[29]
HFET	AlGaN/GaN	Protons (68 MeV) Carbon (68 MeV) Oxygen (68 MeV) Krypton (120 MeV)	$1x10^{13}cm^{-2}$ $1x10^{10}cm^{-2}$ $1x10^{10}cm^{-2}$ $1x10^{10}cm^{-2}$	[30]
HEMT	AlGaN/GaN	Neutrons (1 MeV)	$1x10^{15}cm^{-2}$	[31]
HEMT	AlGaN/GaN	Protons (3 MeV)	up to $1x10^{15}cm^{-2}$	[32]

Table 1 summarizes the prior and current state-of-the-art for radiation induced effects in GaN devices. As can be seen from the Table 1, the largest efforts in study of radiation induced defects in III-N/GaN heterostructures are devoted to proton, neutron, electron and high energetic ion irradiation. However, almost all kind of material matter interactions generates secondary gamma-photons in the material.

While studies of radiation-induced defects in GaN-based devices have attracted significant interest, information concerning the response of AlGaN/GaN based HEMTs to gamma-irradiation is restricted to a few reports. The mechanism of interaction between gamma-rays with material is well known in literature [23, 33, 34]. The interaction of ^{60}Co gamma-photons with GaN generate Compton electron, having mean energy of about 600 keV, which in turn dissipate their energy by creating large number of secondary electron-hole pairs through various mechanisms. In this respect, gamma-irradiation is equivalent to internal electron irradiation [35]. The effects related to external electron-beam irradiation of III-Nitrides and electron trapping due to electron injection has already been studied in literature [36-38].

The lack of information regarding the effects induced by the exposure to energetic gamma-rays, together with the apparent discrepancies highlight the need for further investigation. This thesis, therefore, intends to fill in the gap as far as gamma-irradiation is concerned. Understanding the defects arising under irradiation not only going to provide new information about the charge carrier transport and polarization effect in such devices but will provide substantial information for improving device performance.

1.2 Overview of GaN material

1.2.1 Crystal Structure

Gallium Nitride (GaN) is a binary III-V direct wide band gap semiconductor having a bandgap of 3.4 eV at room temperature. GaN has three kinds of structures: hexagonal wurtzite (Wz), cubic zinc blende (ZB) and rock salt. From technological point of view, wurtzite structure is the most important form as it is the thermodynamically stable form and easiest to grow [39-41]. Therefore among other forms of GaN, wurtzite structure is preferred for research and device applications. The zinc-blende structure of GaN is metastable. Though the energy difference between the wurtzite and zinc-blend phases is relatively small and this phase can be stabilized by growth on compatible substrates such as (001) crystal-plane Si and GaAs [42]. The rock salt structure of GaN can be produced only under very high pressure of approximately 37 GPa [43]. High pressure results in the structural phase transformation of tetrahedrally coordinated wurtzite structure into a six fold coordinated rock salt structure.

The unit cell of wurtzite structure can be defined by the two lattice parameters a and c, with ratio of $c/a = \sqrt{8/3} \cong 1.633$ (in an ideal wurtzite structure). The structure is formed by two interpenetrating hexagonally close packed (HCP) sublattices, with each of the sublattice occupied by one of the atom species and offset along the c-axis by 5/8 of the cell height relative to the other sublattice. Each sublattice includes four atoms per unit cell, and every atom of one kind (group III atom) is surrounded by four atoms of the other kind (group V), or vice versa, which are tetrahedrally coordinated at the edges. The crystal structure of unit cell of wurtzite GaN is shown in Figure 1. By convention, the [0001] direction is given by a vector pointing from the Ga atom to the N atom along the c-axis. Due to the strong ionicity of the cation-N bonds,

GaN wurtzite structure deviates from the ideal wurtzite structure. The ratio of lattice parameters (c/a) of the real GaN crystal deviate from the ideal value, and thus the lattice is distorted from the ideal geometry to some extent (as shown in Table 2). A summary of some crystalline properties of wurtzite III-nitrides is presented in Table 2 together with those of the most commonly used 6H-SiC and sapphire substrates.

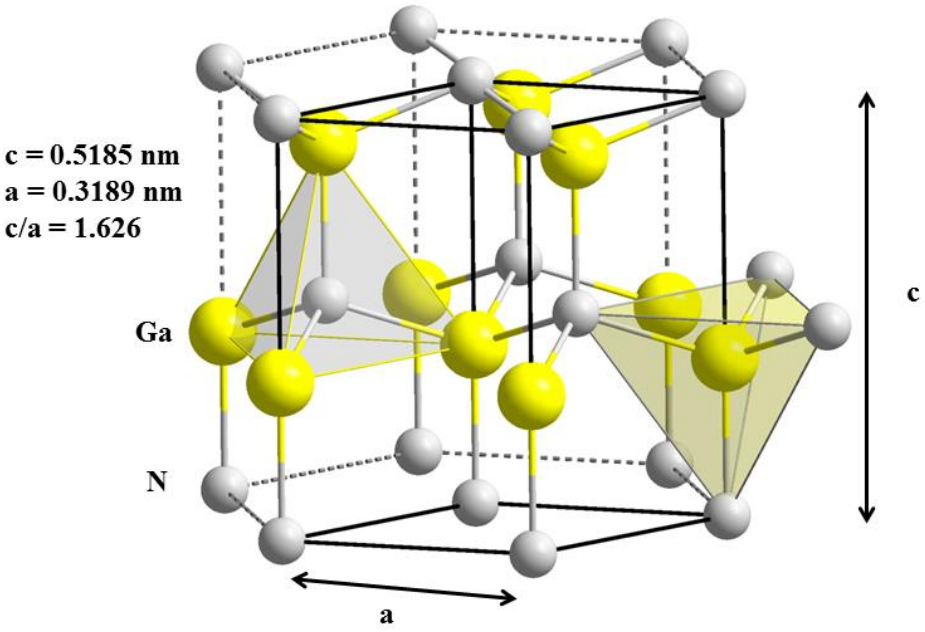

Figure 1. The wurtzite crystal structure of GaN. This structure consists of two interpenetrating hexagonally close packed sublattices offset along c-axis by 5/8 [44].

Table 2 Lattice parameters, thermal coefficients and lattice mismatch relevant to basal-plane epitaxy of hexagonal GaN, AlN and InN on α-Al_2O_3 (sapphire) and 6H-SiC [45] . Coefficients of thermal expansion vary non-linearly with temperature.

Property		GaN	AlN	InN	α-Al_2O_3	6H-SiC
Lattice parameter (Å)	a	3.186	3.1114	3.5446	4.758	3.081
	c	5.178	4.9792	5.7034	12.991	15.092
	c/a	1.6252	1.6003	1.6090	2.730	1.633 ($\times$3)
Thermal expansion coefficient (10^{-6} K^{-1})	a	5.59	4.2	5.7	7.5	4.2
	c	3.17	5.3	3.7	8.5	4.68
Lattice mismatch with (%)	α-Al_2O_3	14.8	12.5	25.4	21.9	—
	6H-SiC	3.3	1.0	14.0	−11.5	—
	GaN	—	−2.4	10.6	−14.8	−3.3

1.2.2 Polarity of GaN

The polar (0001) c-plane, non-polar $(000\bar{1})$ a-plane, non-polar $(11\bar{2}0)$ m-plane of wurtzite structures exhibits quite different behavior in terms polarization and atomic arrangement in respective planes (Figure 2). As shown in the Figure 2, wurtzite structure is not symmetric along the c-direction; thus, GaN surface can have two inequivalent polarities. The two polarities are referred as a Ga-face polarity with designation of (0001) and N-face polarity with designation of $(000\bar{1})$ as shown in Figure 3. The polarity depends on whether the Ga-atoms or N-atoms of GaN forming the crystal face the substrate. Studies have shown that the two polar faces have vastly differing growth and surface properties.

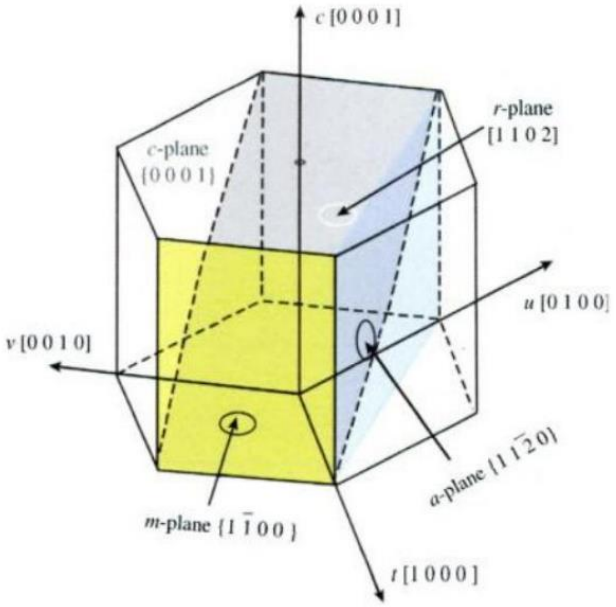

Figure 2. Schematic diagram to represent the a-, c-, m-, and r-planes of GaN wurtzite crystal structure.

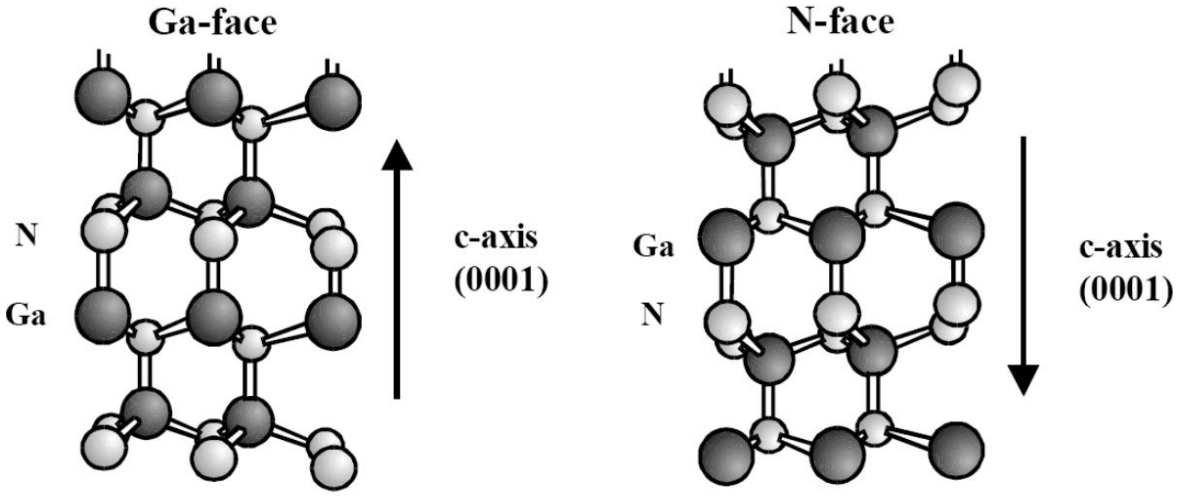

Figure 3. Schematic drawing showing the Ga- face and N-face of GaN wurtzite crystal structure. The asymmetry of GaN along the c-direction leads to the strong spontaneous polarization effects [46].

The distinction between GaN material polarities is essential since both bulk and surface properties depend significantly on it, and because during growth, surface adsorption kinetics can also impact the incorporation rate of impurities [42, 47-52]. It has been demonstrated that the polarity of GaN films can be classified by the growth method used to obtain them, in that films grown by Metal Organic Chemical Vapor Deposition (MOCVD) and Molecular Beam Epitaxy (MBE) have Ga and N polarity, respectively. Studies have shown that the epitaxial growth of GaN by MOCVD retains the polarity of the substrate, while it has also been demonstrated that the buffer layer deposition condition can be used to manipulate one polarity over the other during material growth using Molecular Beam Epitaxy (MBE) [50, 52-54]. In case of Metal Organic Vapor Phase Epitaxy (MOVPE) on sapphire substrate, low temperature buffer layers of GaN or AlN lead to Ga-face polarity. However for MBE growth technique, studies show that GaN buffer layer leads to N-face polarity while AlN buffer layer leads to Ga-face polarity. Ga-polar surfaces typically grow faster than N-face and due to the high deposition rates achievable, GaN grown with Hydride Vapor Phase Epitaxy (HVPE) are usually Ga-face [55]. Under optimized growth conditions, specular epitaxial GaN films with superior characteristics resulted to be unipolar Ga-faced. Although, minor changes in growth conditions can also result in the formation of opposite polarity and inversion domains, which can lead to rough surfaces and poor material characteristics [55]. However, sometimes using the same growth technique has found that there are conflicts between the polarities that result from their experiments. For example, GaN films grown by MBE (where nitridation is commonly used) results in Ga-face polarity, while former studies had showed that nitridation is often regarded as a way to obtain N-face polarity films. On the other hand, although the sapphire substrate was not intentionally nitride, a hexagonally-facetted surface (N-face polarity) was observed for GaN film grown by MOCVD on a GaN

buffer layer [56] . In other report, a smooth surface (indicating Ga-face) was obtained for a GaN film by MOCVD grown on a thicker buffer layer, even though the substrate was intentionally nitrided [57]. This shows that the different deposition conditions play a significant role in controlling the polarity of GaN films.

1.2.3 Spontaneous and Piezoelectric Polarization

Polarization is the most important feature in III-N heterostructures that enables and determines the actual operation of various nitride based devices. The lack of inversion symmetry of the wurtzite structure and characteristics of the ionic bond between Ga and N atoms in GaN results in a naturally distorted crystal structure which exhibits permanent polarization along the c-axis even in the absence of strain and/or external fields [58, 59]. This permanent polarization is conventionally referred to as Spontaneous Polarization, $\mathbf{P_{sp}}$.

Table 3 Axial ratio (c/a) and internal parameter u of wurtzite structure [60]

	c/a	**u**
Ideal	**1.633**	**0.375**
GaN	1.626	0.376
AlN	1.601	0.38

In the GaN wurtzite structure, axial ratio value c/a (c and a represents the lattice parameters) is smaller than the ideal of 1.633 and u (anion–cation bond length also known as nearest neighbor distance) is larger than ideal value of 0.375 (Table 3). The deviation in the structural deformation along c axis of thermodynamically stable wurtzite structure results in a large spontaneous polarization [61]. The increase in the deviation of (c/a and u values) going

from GaN to AlN results in an increase in the spontaneous polarization. The spatial variation of such large spontaneous polarization can induced two dimensional lattice charge distribution which can values between 10^{13} and 10^{14} e/cm^2 located on the two surfaces of the samples. The direct consequence of this large polarization and the corresponding surface density is the appearance of large internal electric field. In Ga-face samples, the crystallographic c-axis and the internal electric field point away from the substrate towards the surface, whereas the polarization has the opposite direction. The polarization-induced fixed lattice charges are negative at the surface and positive at the substrate interface. For N-face material, all charges and directions are inverted (Figure 4).

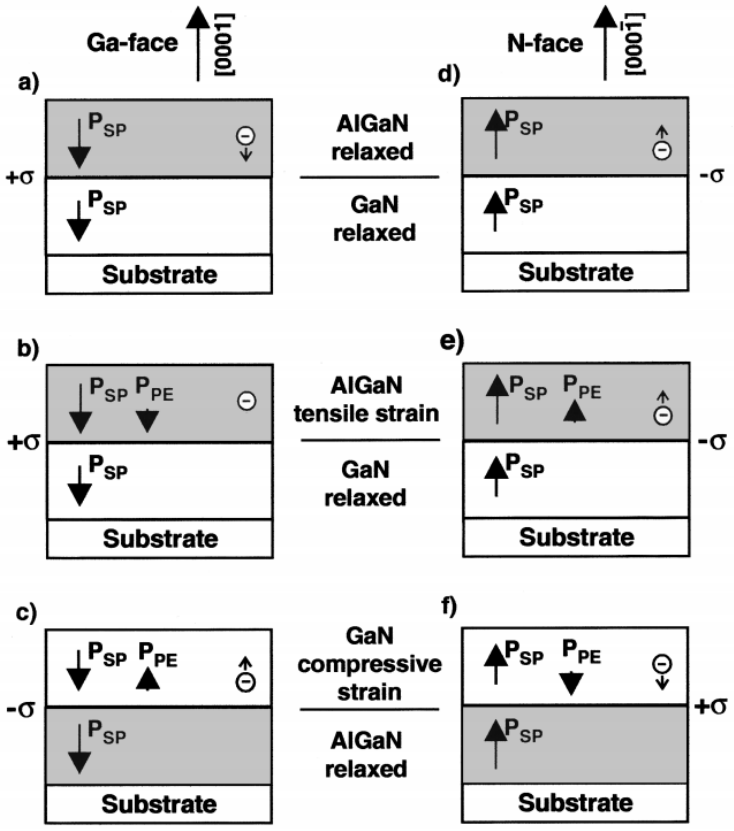

Figure 4. Directions of the spontaneous (P_{sp}) and piezoelectric (P_{pz}) polarization in Ga- and N-face for strained and relaxed AlGaN/GaN heterostructures. [62].

In addition to the spontaneous polarization, lattice distortions such as those induced by externally applied stress or by strained epitaxy, can result in significant changes in the polarization of the material [63]. This means external stress can modify the axial ratio (c/a) and cation-anion bond length (u) which can induce strong piezoelectric polarization in Group III-Nitrides wurtzite crystal. While the generalized piezoelectric tensor has three independent non-vanishing components, only polarizations along the (0001) direction are of technological importance, as this is the conventional growth direction used in both bulk and hetero-epitaxially deposited III-Nitride materials [42]. The piezoelectric constants of III-Nitrides are almost an order of magnitude larger than III-V and II-VI semiconductor compounds [64]. The piezoelectric polarization $\mathbf{P_{pz}}$ is the product of the piezoelectric coefficients e_{ij} and the stress tensor σ_{ij}. For wurtzite structure in the [0001] direction $\mathbf{P_{pz}}$ is calculated by

$$P_{PZ} = e_{33}\,\boldsymbol{\varepsilon_z} + e_{31}\left(\boldsymbol{\varepsilon_x} + \boldsymbol{\varepsilon_y}\right) \quad (1)$$

where ε_z is the strain along the c axis and $\varepsilon_x = \varepsilon_y$ is the isotropic in-plane strain.

$$\boldsymbol{\varepsilon_z} = -2\frac{C_{13}}{C_{33}}\,\boldsymbol{\varepsilon_x} \quad (2)$$

where C_{13} and C_{33} are elastic constants .

$$\boldsymbol{\varepsilon_x} = \boldsymbol{\varepsilon_y} = \frac{a - a_o}{a_o} \quad (3)$$

where a is the in-plane lattice constant and a_o is its equilibrium value. Using equation (1) and (2) the piezoelectric polarization in the [0001] direction is given by:

$$P_{pz} = 2\boldsymbol{\varepsilon_x}\left(e_{31} - \frac{C_{13}}{C_{33}}e_{33}\right) \quad (4)$$

Since $\left[e_{31} - \frac{C_{13}}{C_{33}}e_{33} < 0\right]$ for whole range of compositions of AlGaN, the piezoelectric polarization is negative under tensile strain and positive for compressive strained barriers for lattice mismatched growth such as AlGaN on GaN, respectively (Figure 4). Table 4 summarizes

the various coefficients needed to calculate the piezoelectric polarization. The usefulness of total polarization in AlGaN/GaN heterostructures will be discussed in more details in next section.

Table 4 Piezoelectric Polarization Parameters [65, 66]

Wurtzite	**AlN**	**GaN**	**InN**
C_{13}(GPa)	94	68	70
C_{33}(GPa)	377	354	205
e_{31}(C/m^2)	-0.53	-0.34	-0.41
e_{33} (C/m^2)	1.50	0.67	0.81
a (Å)	3.108	3.0197	4.580
a_o (Å)	4.983	5.210	5.792

1.2.4 Physical Properties of GaN

For high frequency and high power output amplification, parameters like large band gap, high breakdown field, high thermal conductivity, high charge carrier mobility, high saturation velocity and low dielectric constant are desirable. Electrical parameters of several binary semiconductor materials are summarized in Table 5.

Table 5 Physical parameters of group III nitrides compared with other semiconductors.

Properties	GaN	GaAs	AlN	Si	Diamond
Band Gap (eV)	3.4	1.42	6.03	1.11	5.46 - 5.6
Breakdown field (MV/cm)	3.3	0.4	8.4	0.3	5
Dielectric constant ε_r	9.5	12.5	8.5	11.9	5.5
Thermal conductivity (W/Km)	130	54	285	148	2500
Saturated Velocity (10^7 cm/s)	2.5	0.74	1.4	1	1.56
Hole mobility (cm^2/Vs)	150	400	14	450	1800
Electron mobility (cm^2/Vs)	990	8500	135	1400	2200

Because of GaN inherent material characteristics, devices based on GaN can provide considerably superior performance as compared to broadly employed silicon or GaAs materials. The main advantages of GaN material can be outlined as follows:

- Wide band-gap of GaN results in high critical breakdown field of 3.3 MV/cm compared to the 0.3 and 0.4 MV/cm for Si and GaAs respectively. High critical breakdown field of GaN permits the device to sustain high DC and RF terminal voltages, which generates high RF output power [67].

- Dielectric constant values of the wide band gap semiconductors are comparatively lower than those for the conventional semiconductors. The dielectric constant ε_r represents the capacitive loading of a transistor which affects the device terminal impedances. The values of ε_r are about 20% lower in GaN whereas it is about 55 % lower in diamond. This means for given impedance GaN device can be about 20% larger in area. As a consequence, the increased GaN area permits the generation of larger currents and higher microwave output power.
- The high thermal conductivity of GaN can easily extract the heat from the device. Thermal conductivity is an important parameter for the design of the high power devices. Poor thermal conductivity can results in the degradation of device operation at elevated temperatures.
- The DC and RF currents flowing in the device are directly dependent on the slope (mobility) of the charge carrier velocity versus electric field transport characteristics. GaN has relatively low mobility (990 cm^2/Vs) but has high value of the saturation velocity which is observed at high electric field. However, the ternary alloy AlGaN is the key for the fabrication of AlGaN/GaN heterostructures which form the basis of modulation doping with enhanced mobility. Due to reduced scattering and two-dimensional confinement effects, the two dimensional gas formed at the interface has much higher value of mobility compared to bulk GaN [68, 69].
- High saturation velocity of GaN allowed for high frequency of operation. The bulk GaN has saturation drift velocity of 2.5 $\times 10^7$ cm/s whereas for Si it is 1 $\times 10^7$ cm/s and for GaAs only 0.74 $\times 10^7$ cm/s. As can be seen Table 4, AlGaN/GaN heterostructure has even higher saturation velocity (about 3 $\times 10^7$ cm/s).

1.3 Basic AlGaN/GaN HEMTs Physics

A High Electron Mobility Transistor (HEMT), also known as Modulation Doped Field Effect Transistor (MODFET), is a field effect transistor consists of two different semiconducting materials brought into intimate contact. The differing band gaps of the two materials, and their relative alignment to each other creates a triangular quantum potential well near the boundary of the interface. Within the potential well, electrons are free to move parallel to the interface but tightly confined in the perpendicular direction, and thus occupy well defined energy levels. Electrons appear to be a 2D sheet and are therefore referred to as a two dimensional electron gas (2DEG). Figure 5 shows the basic structure of AlGaN/GaN HEMTs.

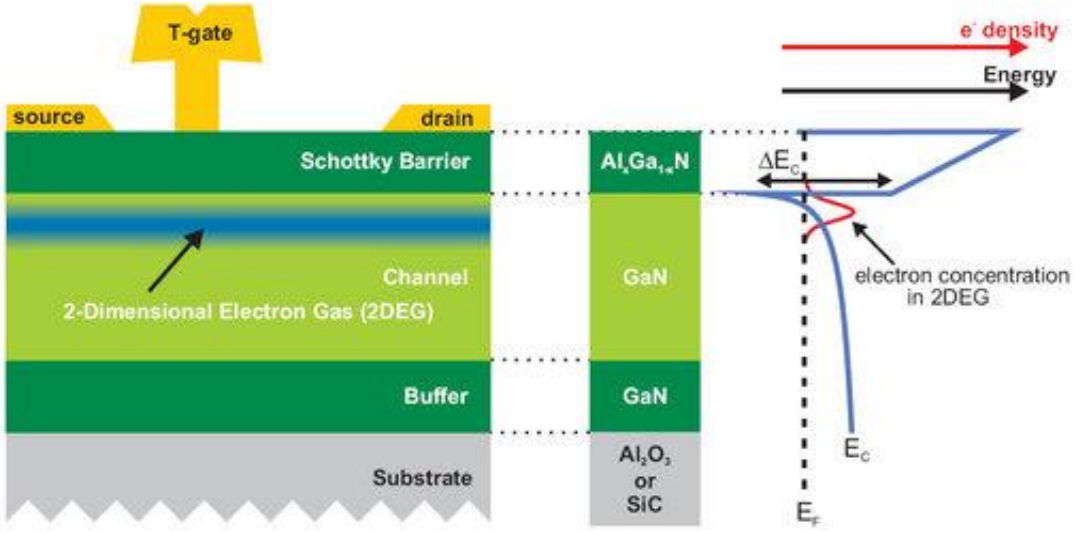

Figure 5. Basic AlGaN/GaN HEMT structure.

In conventional III-V semiconductor, 2DEG channel is formed from the carriers accumulated along an asymmetric heterojunction, i.e. a heavily doped wide band gap semiconductor and a lightly doped low band gap semiconductor. To equalize the Fermi level charge transfer takes place across the interface and therefore electrons are separated from the

donor atoms and collected as 2DEG below the hetero-interface region. The channel region has very few ionized impurities to scatter the electrons, and consequently a very high mobility and a high saturation velocity can be achieved. Unlike the channel being formed in the conventional III-V semiconductor where a doped layer is necessary, the 2DEG in the AlGaN/GaN is induced by the strong polarization fields as discussed in the following section.

The AlGaN/GaN heterostructure is created when a thin epi-layer of AlGaN is grown on a relatively thick GaN layer. The 2DEG in AlGaN/GaN based HEMT is induced by the spontaneous ($\mathbf{P_{sp}}$) and strain induced piezoelectric ($\mathbf{P_{pz}}$) polarization [59, 62, 70]. The two distinct polarization effects in GaN based HEMT devices are large enough to produce 2DEG even without intentional doping of AlGaN layer. Under the right conditions, the conduction band edge dip below the fermi level and produce a region whose states are occupied by the conduction electrons that forms a 2DEG. GaN-based HEMTs can achieve a high mobility and high 2-DEG sheet carrier density (n_s) of typically $5x10^{12} - 1.5x10^{13}$ cm^{-2} very easily as compared to other III–V compound semiconductor based devices [71-74].

In AlGaN/GaN heterostructures, the total macroscopic polarization ($\mathbf{P}$) is the sum of the spontaneous ($\mathbf{P_{sp}}$) and the strain induced piezoelectric polarization ($\mathbf{P_{pz}}$). In the absence of external applied electric field or strain, spontaneous polarization constitutes a non-zero volume dipole moment in the crystal. For zero strain, spontaneous polarization exists because of the non-ideality of GaN wurtzite crystal structure. However, the strained induced piezoelectric polarization exists because of the difference between lattice constants at the heterostructure, and thus increases as the strain at the interface increases. Therefore, the total polarization of strained AlGaN layer is stronger than that of the underlying relaxed GaN buffer layer.

For Ga(Al)-face, the spontaneous polarization for GaN and AlGaN was found to be negative, meaning P_{sp} is pointing towards the substrate (Figure 6). Therefore, the direction of the piezoelectric and spontaneous polarization is parallel in the case of tensile strain and anti-parallel in the case of compressively strained top layers. While for N-face, the piezoelectric as well as spontaneous polarization changes its direction, and is directed towards the surface.

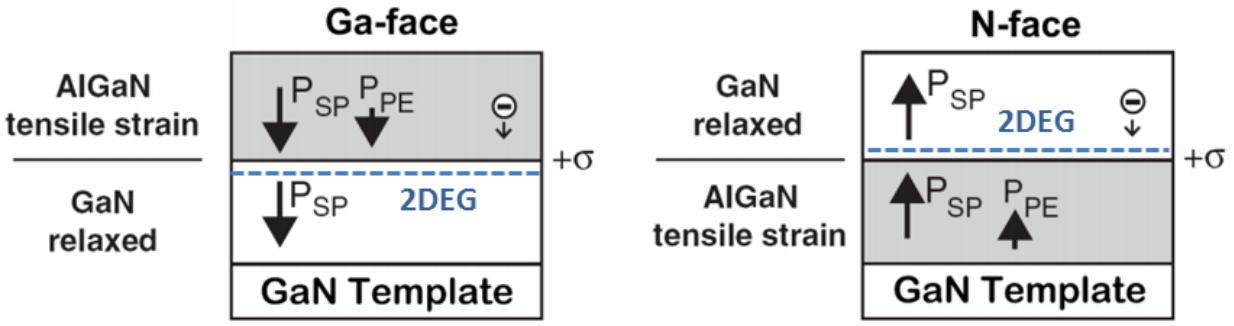

Figure 6. Structure of AlGaN/GaN showing combined spontaneous and piezoelectric polarization in Ga- and N- face heterostructures. In both the cases, AlGaN layer is assumed to be under tensile strain by the GaN substrate layer. 2DEG forms at the interface of materials and slightly offset into the GaN layer. After Reference [46].

At AlGaN/GaN interface the gradient of total polarization in space is a polarization induced charge density which is given by $\rho_P = -\nabla . \mathbf{P}$. The abrupt interface of AlGaN/GaN heterostructure causes a polarization sheet charge density which is positive for AlGaN on top of GaN with Ga-face polarity and GaN on top of AlGaN with N-face polarity (Figure 6). The sheet charge density is defined by [46]:

$$\sigma = P\,(AlGaN) - P\,(GaN)$$
$$= (P_{pz}(Al_xGa_{1-x}N) + P_{sp}(Al_xGa_{1-x}N) - P_{sp}(GaN)$$
$$= [\,(3.2\,x - 1.9x^2) \times 10^{-6} - 5.2 \times 10^{-6}x]Ccm^{-2} \quad (5)$$

Increase in the Al-content of the heterostructure increase the net polarization of the AlGaN layer and thus increases the sheet density. Free electrons will tend to compensate this positive sheet charge density (+σ) by forming a 2DEG at the hetero-interface of the two nitrides with sheet carrier concentration, n_s. A negative polarization induced sheet charge density causes the accumulation of holes at the junction. Even for the relaxed AlGaN, the difference in the spontaneous polarization of AlGaN and GaN material can confine electrons at the interface.

1.4 Defects in GaN

In the ideal semiconductor crystal, the periodic potential associated with the atomic arrangement of the crystal lattice results in the formation of allowed and forbidden energy bands. The allowed electron values for such a crystal are regarded as continuous and their corresponding wave-functions are extended all across the crystal. However, atoms in a real semiconductor do not follow the perfect crystalline arrangement. The arrangement is broken by the presence of defects, lattice imperfections and/or foreign chemical impurities, which induce localized perturbations in the periodic atomic potential. The perturbation results in the formation of bound states in the forbidden energy gap that can significantly affect the physical, chemical, electrical and optoelectronic properties of the material. However, the existence of defects does not necessarily have adverse effects on the properties of the materials. It is useful as long as their concentration and spatial localization can be controlled. It is thus that the controlled introduction of defects (that is, doping with foreign chemical impurities) plays an important role in various technological processes as it enables the manipulation of the magnitude and type of conductivity making possible the realization of devices such as light emitters and detectors, transistors, etc.

All defects in crystalline semiconductors can be conveniently classified according to their behavior (donors, acceptors, traps, generation/recombination centers, compensating and passivation centers, and scattering centers), the energy position of their bound states in the energy gap (shallow- or deep-level defects), their origin (native defects, impurities, and radiation/processing induced defects) or their microstructure (point, line, planar/surface or volume defects). Theoretical studies on defects generally explore the electronic and optical properties of defects, which are based on the microstructure of vacancies, interstitials and impurities. While, charge trapping studies are generally focused on the identification of defects in terms of their thermal activation energies and concentrations and their effects on material properties and consequently the device performance. In the following section, defects in GaN are briefly reviewed in terms of their impact as shallow or deep level, dislocations and defects introduced in GaN by interaction with high-energy particles.

1.4.1 Prior Studies of Radiation Induced Defects

As mentioned earlier, GaN is a wide-bandgap material that has high breakdown voltage and high saturation velocity. Therefore these materials have attracted interest for their potential applications for high-frequency, high power, high temperature electronic devices. These materials are relatively resistant to radiation damage and thus used for space and terrestrial environments where irradiation is strong. A clear understanding of how defects are created in GaN by any irradiation can provide necessary background knowledge for predicting the behavior of these materials in radiation environments. The most primary defects created in GaN by any irradiation are Frenkel pairs in Ga and N sublattices by the Compton electrons, having mean energy of 600 keV [6, 75, 76]. These defects include vacancies, interstitials, antisites as well as complexes between defects and impurities.

Theoretical calculations showed that nitrogen vacancies in GaN are electrical resonances with levels in the conduction band. After capturing electrons, they turned into effective-mass (EM) like shallow donors [77]. Experimental measurements show that nitrogen vacancies (V_N) are shallow donor in GaN having ionization energy of 40-60 meV below the conduction band [77-79], but in AlN the same defect is a deep trap. Nitrogen interstitials (N_i) is a deep acceptor having energy level near 1eV below the conduction band [80, 81]. Gallium vacancies (V_{Ga}) is a doubly charge state which act as a trap for both electrons and holes. The energy level for the gallium vacancies lies near 1 eV above the valence band [82]. However, Ga interstitials (Ga_i) forms negative-U type donors whose transition level is located near 0.8 eV below the conduction band [81]. Figure 7 represents the schematic representation of defect levels introduced in the band gap of GaN by various ionizing radiations.

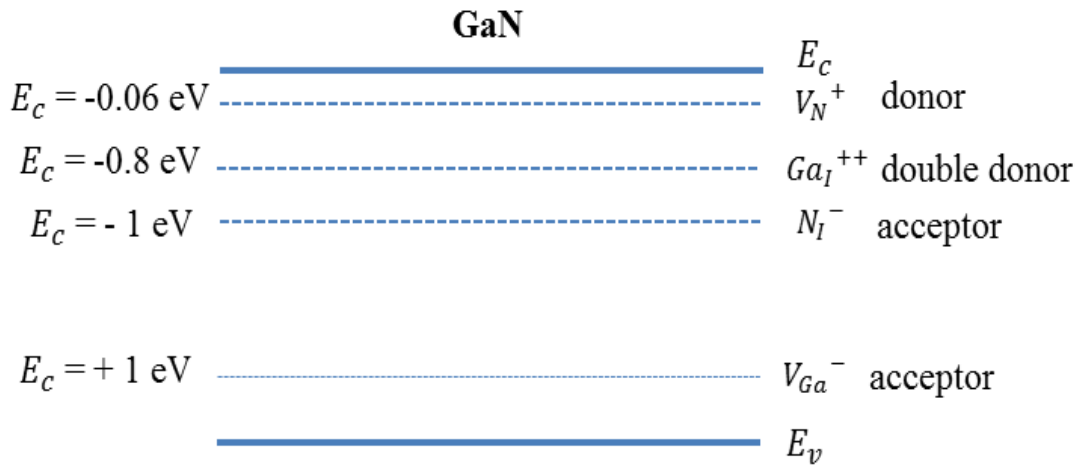

Figure 7. Schematic representation of irradiation induced defect levels in the GaN bandgap.

Look et. al. showed that electron irradiation (0.7-1 MeV) in GaN introduces new shallow donors and shallow or deep acceptor with same introduction rate of 1 cm^{-1}[6]. Shallow donors with ionization energy of 64 meV were attributed to nitrogen vacancies and acceptor being the nitrogen interstitials. It was shown that electron irradiation in GaN hardly change the electron

concentration while the mobility of the electrons decreased with increasing dose. The results were explained from the N-Frenkel pair model, with the donor and acceptor are components of the N Frenkel pair, i.e., the N vacancy, and N interstitial, respectively. High energy electron irradiation (> 1.5 MeV) creates deeper acceptors Ga vacancies related defects in GaN. Such acceptors compensate the nitrogen vacancy donors and are responsible for the slight change in the charge density [83]. Deep level transient spectroscopy (DLTS) characterization showed that 1 MeV electron irradiation on AlGaN/GaN heterostructures induced deep electron traps with activation energy of 0.9 eV. These deep traps were shown to mostly likely relate to the nitrogen interstitials [84]. Irradiation with ^{60}Co gamma-rays also showed the presence of electron traps with activation energy of 80 meV. The electron traps were observed for the V_N donors [85]. Implantation of 150 keV with proton fluence up to 5 x 10^{15} cm^{-2} in n-GaN also create deep electron traps with activation energies near 0.2 at low dose and 0.95 eV at progressively higher dose. The presence of deep hole traps with activation energies of 0.25, 0.6 and 0.9 eV were also observed from deep level spectra measurements. The results were explained by the formation of large complexes with the addition of new radiation defects to the simple radiation defects formed at the low doses. Strong degradation in minority carrier diffusion length and strong decrease in the NBE intensity were also observed for highly implanted samples [86].

A common set of electron traps with activation energies of 130 meV, 160 meV and 180-200 meV were observed in GaN after irradiating with electrons, gamma-rays and protons in the mega-electron-volt range. 180-200 meV electron traps activation energy is the sum of 60 meV trap ionization energy and 140 meV capture activation energy. The high activation energy traps are the complexes of nitrogen vacancies with other native point defects, such as antisite defects

or nitrogen interstitials. The 60-70 meV shallow donor defects are most likely the nitrogen vacancy [79]. 130 meV and 180-200 meV traps are assumed to be donor like.

On AlGaN/GaN heterostructures, the research regarding the effects of irradiation has not been investigated systematically in the literature. However, Chernyak et. al. showed the effects of electron irradiation on the diffusion length of Mg-doped p-AlGaN/GaN super-lattices grown by MOCVD. Diffusion length was shown to increase during 1500 s of electron beam irradiation. The observed changes were attributed to the increase in the minority carrier lifetime, which is related to the charging of the metastable centers associated with Mg doping [87]. The other proton irradiation studies carried out on AlGaN/GaN structures showed that 2 MeV proton irradiation results in a conductor to (Mott) insulator transition in 2DEG. The transition was related to degradation in the mobility [12]. It was shown that the sheet carrier density decreases by a factor of 2 while the mobility by a factor of 1000. In a 2-D system, the carrier scattering by charged defects is more dominant factor than the tapping of carriers. This explains the fact that irradiation is more harmful to mobility then to the decrease of the carrier density. After a certain high-irradiation fluence level, the resistivity reaches values typical of insulators, but the mobility degradation is the main mechanism which contributes to the change in resistivity.

1.5 Outline of Dissertation

This dissertation focusses on understanding how the minority carrier transport and optical properties are affected by the gamma-irradiation, particularly for the low doses (below ~ 250 Gy). Investigation of gamma-irradiated device properties gives important information about defects in semiconductor heterostructures, especially if additional traps are introduced under external irradiation. At the same time, such investigation is very important not only from the

fundamental point of view, due to obtaining substantial information on the physical properties of semiconductor materials, but it also gives the values of the device performance for application in radiation harsh environments.

Chapter 2 describes the experimental techniques used in this thesis for each of the experimental rounds of irradiation and measurements. This includes both hardware and software employed in the experiments. The interaction of gamma-irradiation with material is described in details. Electron Beam Induced Current (EBIC) and Cathodoluminescence (CL) methods are explained, and how these methods can be used to calculate experimental diffusion length and thermal activation energy are discussed. The data collection procedures and why those procedures were applied are also laid out in detail.

Chapter 3 presents the results of the experimental measurements. The experimental results include the one high (above ~250 Gy) and four low doses (below ~250 Gy) gamma-irradiation experiments are described in details. The results of the multiple irradiation measurements and gamma-irradiation that the devices received are discussed. This chapter also proposed the description of the physical models that link the effects of gamma-irradiation to observed changes in AlGaN/GaN HEMTs characteristics.

Chapter 4 offers a conclusion to the thesis. It also provides a summary of the results obtained in this study and recommended future areas of research interest in the phenomenon of gamma-irradiation.

CHAPTER TWO: EXPERIMENTAL PROCEDURES

This chapter describes the details about the devices used in this study, the irradiations and the experimental methods contributing for this thesis. Metal Organic Vapor Phase Epitaxy (MOVPE) and Metal Organic Chemical Vapor Deposition are the main methods used for the AlGaN/GaN HEMTs preparation. Description about the HEMT's specifications for individual devices will be addressed in Chapter 3. First section describes the procedures by which gamma-irradiation doses were applied to the samples. Finally, the two main characterization techniques; Electron Beam Induced Current (EBIC) and Cathodoluminescence (CL) are introduced along with specific procedures followed when applying these characterization techniques.

2.1 Irradiation Procedures

Devices under test were exposed to cumulative ^{60}Co gamma-irradiation doses starting from 50 Gy to a maximum total dose of 1000 Gy. Device irradiations were performed in the NORDION Science Advance Health ^{60}Co-irradiator at the irradiation temperature less than <50°C. During device irradiation, the samples were held in nitrogen ambient, with drain, source and gate contacts kept electrically shorted. The density of photo-electrons generated from the interaction of ^{60}Co-gamma rays with the protective lead walls of the Nordion irradiator is expected to be low due to the Al filter of the irradiation chamber [88]. Since it is not possible to measure the spectral photon distribution in the irradiation chamber, Compton-scattering of the main ^{60}Co gamma-photons lines, at 1.17 MeV and 1.33 MeV, could contribute a significant density of low energy photons ($E_\gamma \leq 0.60$ MeV). These photons may result in dose-enhancement effects in the vicinity of device's metalized contacts [19, 89].

It is important to note that, 600 keV Compton electrons, generated by the interaction of the material with ^{60}Co gamma-photons with average energy of 1.25 MeV, are likely to introduce donor-type nitrogen-vacancy-related defects in III-N layers. These type of defects have been reported after low-energy proton irradiations, in particular, after 1 MeV electron irradiations [90, 91]. Such defects have been reported to be affected by annealing at temperatures as low as 400 K [92], the effect of radiation-induced nitrogen-vacancy-related defects would be significantly affected by any characterization conditions under which self-heating could increase the device temperature near 400 K. Similar conditions are applicable to radiation induced hole trapping at pre-existing defects, as an increase in temperature will accelerate the emission of trapped carriers and their transport to the gate contact.

The gamma-ray fluence can be calculated from the total ionizing dose using the relation 1rad (Si) = 2.0 x 10^9 photons/cm^2 [88]. The concentration of point defects introduced via displacement damage in the thin-barrier layer of AlGaN film can be expressed in terms of an effective Frenkel-pair generation rate per incident gamma-rays photon [93, 94]:

$$N_F = N_0 \sigma_d \varphi_\gamma \quad (6)$$

where N_F is the concentration of generated Frenkel-pairs and $N_0\sigma_d$ is the effective defect production rate, with σ_d and N_0 being the effective displacement cross section and the number of lattice atoms per unit volume, respectively. A conservative value of $N_0\sigma_d$ can be obtained by allowing N_F to be equal to an effective increase of the density of ionized donor-like defects in the AlGaN layer, ΔN_T. Thus according to equation 6, ΔN_T should scale linearly with φ_γ. Note that our results cannot be described by a single defect production rate for the range of the doses. The defect production rates estimated for two doses range- below and above 1 Mrad (Si) are 413 ± 45

defects/cm and 28 ± 6 defects/cm, respectively. The diagram in Figure 8 shows the main energies of gamma-photons and beta-particles to be taken into account. The considered mechanisms and possible radiation induced defects are summarized in the Table 6.

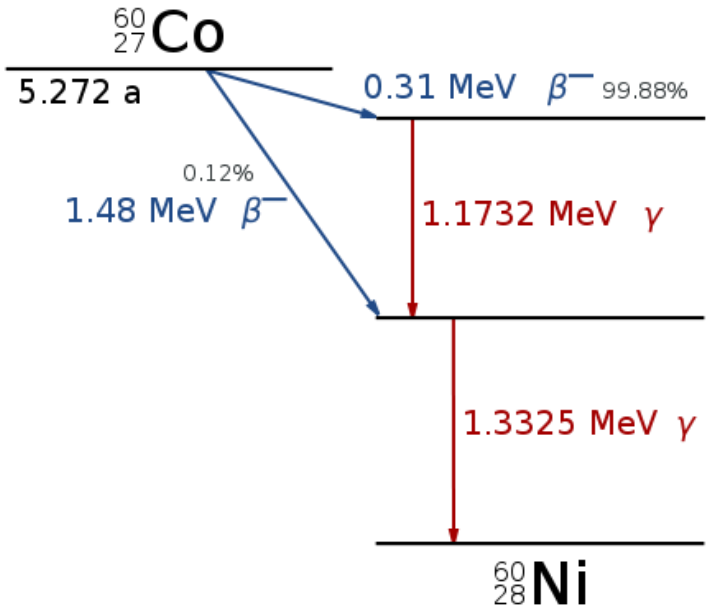

Figure 8. Cobalt-60 decay diagram.

Among all the ionization radiations, ^{60}Co gamma-rays have an important advantage in irradiation studies because:

(1) The created defects are uniformly distributed throughout relatively large specimens.

(2) No secondary irradiation is induced by irradiation of the material with gamma rays at the maximum energy of 1.33 MeV, and, therefore, the samples can be safely handled after the irradiation.

Table 6 Possible radiation induced effects in III-Nitrides

Energy of Gamma-photons or Secondary generated particles	Possible defects	References
^{60}Co gamma-photons: 1.33 MeV; 1.17 MeV (1.25 MeV at average)	Activation of dislocation-related defects, acting as sinks and sources of point defects during irradiation; Displacement damage: shallow nitrogen vacancy donor like defects in III-N region	[90, 91] [95, 96]
Compton electrons (600 keV), generated via the interaction of 1.25 MeV gamma-photons with material	Donor-like nitrogen vacancy related defects	[92, 97]
Electrons with energy ~ 300 keV photo-generated from metalized contacts	Ionization of pre-existing defects by injection of photo-generated electrons into the 2DEG channel and trapping of photo-generated holes in the III-N region	[19, 89]

2.2 Electron Beam-Specimen Interaction

A number of different types of signals are produced in the Scanning Electron Microscope as the electron beam interacts with atoms within the specimen. The interaction results in large variety of emitted signals: backscattered electrons, secondary electrons, X-rays, Auger electrons, Cathodoluminescence (Figure 9). The electrons-specimen interaction can provide information on:

1) Specimen composition

2) Topography

3) Crystallography

4) Electrical Potential

5) Local Magnetic Field

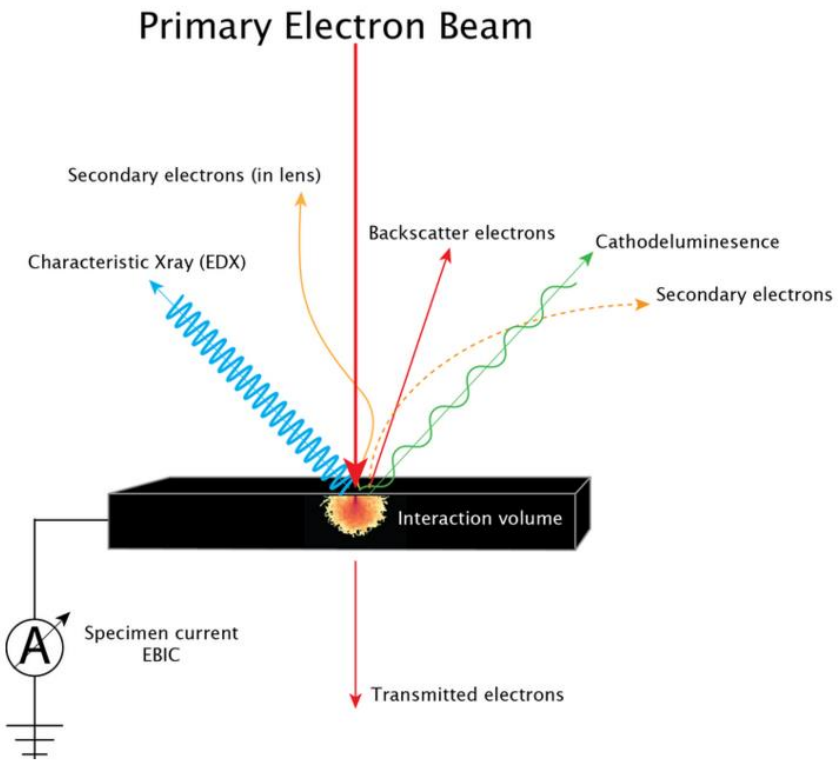

Figure 9. Electron energy distribution for 5 keV electrons in (a) silicon and (b) gallium nitride. ((a) and (b) not on the same scale).

Each interaction results in a loss of energy or change in a momentum of the primary electron. In semiconductors, this is determined by the interaction volume of the beam electrons, which is the volume in which the primary electron beam have sufficient energy to undergo a series of elastic and inelastic scattering events in the specimen. The interaction volume depends on the following factors:

1) Atomic number of the material being examined; higher atomic number materials absorb or stop more electrons and so have a smaller interaction volume.

2) Accelerating voltage being used; higher voltages penetrate farther into the sample and generate larger interaction volumes

3) Angle of incidence for the electron beam; the greater the angle (further from normal) the smaller the volume.

The depth of penetration to which these events happen is determined by the energy of the electron beam, which is in its most general form derived by Kanaya and Okayama [98]:

$$R_e(\mu m) = (\frac{0.0276\,A}{\rho\, Z^{0.889}})E_b^{1.67} \quad (7)$$

with E_b the electron energy in keV, A the atomic weight in g/mol, ρ the material density in g/cm^3 and Z is the atomic number. In silicon, 5 keV electron beam gives the penetration depth of 0.47 µm. At 30 kV, the electron beam typically penetrates 10 µm into a low atomic number specimen like carbon. Figure 10 shows simulations on the electron generation volume in Si and GaN for 5 keV SEM electrons. Note that the scale is different for both specimens; the maximum width of the generation volume in silicon is 400 nm, while in gallium nitride it is 150 nm. Since $A/Z^{0.889}$ roughly remains constant for different materials, the difference in generation volume is mainly caused by the density differences between Si (ρ = 2.33 g/cm^3) and GaN (ρ = 6.10 g/cm^3).

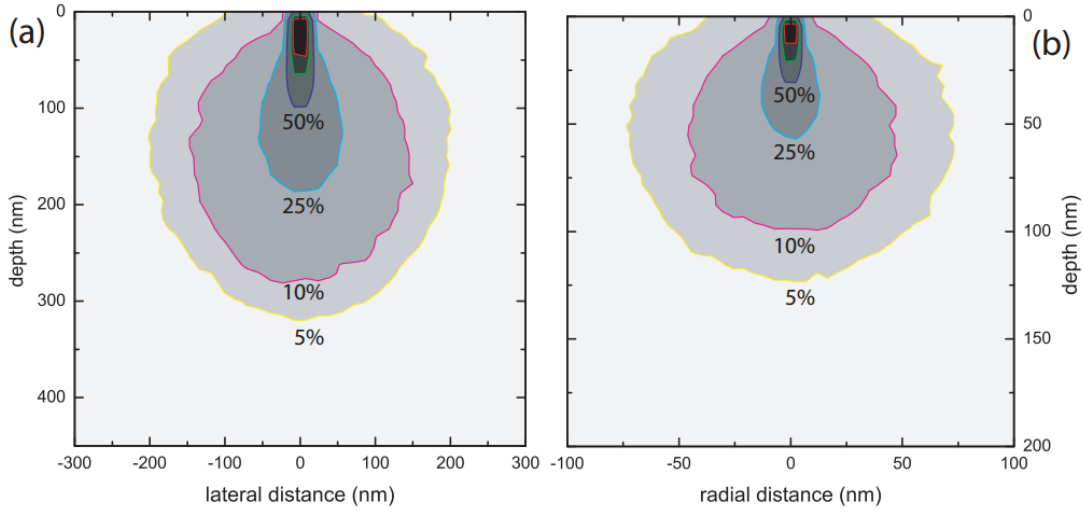

Figure 10. Electron energy distribution for 5 keV electrons in (a) silicon and (b) gallium nitride. ((a) and (b) not on the same scale).

2.3 Electron Beam Induced Current

Electron Beam Induced Current (EBIC) is a semiconductor analysis technique that characterizes the electrical behavior of semiconductor materials by measuring an induced current signal when sample is exposed to an electron beam. Electron-hole pairs created by the SEM electron beam diffuse in random motion and will eventually recombine or annihilate each other if there is no localized electric field. But if the semiconductor sample has an internal built-in potential, as will be present in the depletion region of a p-n junction or Schottky junction, these pairs can be separated and drifted relative to the field orientation. By electrically contacting the sample through a current amplifier, a current will flow that is referred as Electron Beam Induced Current. EBIC measurement has been mostly performed inside the conventional scanning electron microscopes (SEMs) equipped with an electrical stage. Typical EBIC technique can be used to identify buried junctions or electrical defects in semiconductor devices (such as grain boundaries or single dislocations); as well as to measure non-radiative recombination activity and minority charge carrier properties.

2.3.1 EBIC Experimental Setup

There are basically two basic configurations for observing EBIC and these are illustrated in Figure 11. The two configurations are the planar configuration and the perpendicular configuration [99]. In the parallel configuration, the electron beam is scanned normal to the charge collecting barrier (Figure 11(a)). This configuration of EBIC is mainly used for defect characterization. However in the perpendicular configuration, the electron beam is scanned parallel to the charge collection barrier. (Figure 11(b)). The detection of the defects is not very straightforward in the perpendicular configuration. The presence of defects in the vicinity of a

junction is detected in a line scan mode over the sample surface. In the absence of defects, the non-equilibrium electron–hole pairs generated by the SEM diffuse over a longer distance before reaching the junction. The presence of a localized defect causes a reduction in the collected EBIC signal due to increased recombination at the defect. The perpendicular configuration is used to measure the diffusion length simultaneously with the lifetime. As this thesis concentrates on the minority carrier diffusion length measurements, therefore the perpendicular configuration as shown in Figure 11 (b) will be used and discussed.

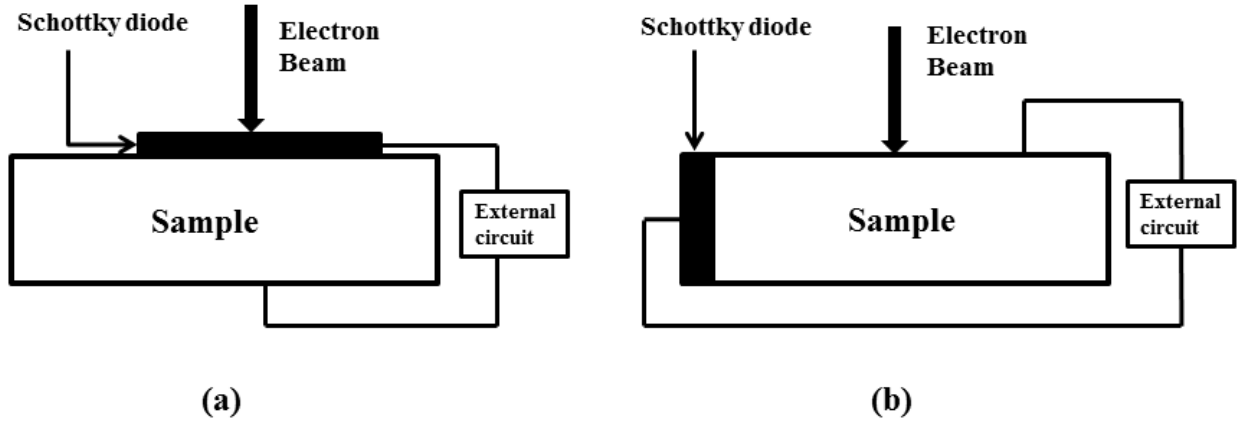

Figure 11. Experimental schematic illustration of SEM-EBIC charge collection configuration. (a) illustrate the planar Schottky barrier configuration used mainly for defect studies. (b) illustrate the perpendicular Schottky barrier configuration used for minority carrier lifetime and diffusion length measurements.

In the present work, EBIC measurements were performed in-situ in Philips XL 30 SEM under 20 keV electron beam accelerating voltage. This voltage corresponds to a penetration depth of 1.2 µm. The temperature of the sample was varied by 25°C to 125°C by specially designed hot stage and the external temperature controller. For EBIC observation, the variation of induced current at a Schottky junction is measured in a line scan mode over the specimen area

of interest. External circuit to record the EBIC signal was consists of: (1) SRS current preamplifier, used to adjust the sensitivities. (2) Keithley 2000 voltmeter, used to digitize the signal before displayed on a computer. The PC displays the voltage versus distance from the junction scanned by the SEM, starting from the end of the Schottky junction.

2.3.2 Diffusion Length and Activation Energy from EBIC

Electron Beam Induced Current can be used to measure the minority carrier diffusion length and the activation energy [100, 101]. Non-equilibrium charge carriers created at a point by the SEM will diffuse in all the directions and some fraction will recombine along the way, over a characteristic distance given by the minority carrier diffusion length. Minority carrier diffusion length measurements using EBIC was first demonstrated by Higuchi and Tamura in 1965 [102]. In this technique, if non-equilibrium electron hole pairs are generated inside a depletion region, the electric field of the space charge separates the charge carriers and electron beam induced current can be measured externally. When the beam is slowly moved away from the barrier/junction in a line-scan mode, the EBIC current, I_{EBIC} , decays as less and less minority carriers are able to diffuse to the space charge region. For the n-type material, holes reaching the zero-bias depletion region under the Schottky contact are collected as EBIC signal but if the material is p-type then the opposite applies, with electrons being collected. The exponential decay of the I_{EBIC} with the distance from the junction can be analyzed by the following expression:

$$I_{EBIC} = Ad^{\alpha} exp\,(-\frac{d}{L}) \quad (8)$$

Where A is a scaling constant, d is beam-to-junction distance, α is an exponent related to surface recombination velocity and L is the diffusion length. The exponential decay of the EBIC signal as a function of distance is shown in Figure 12.

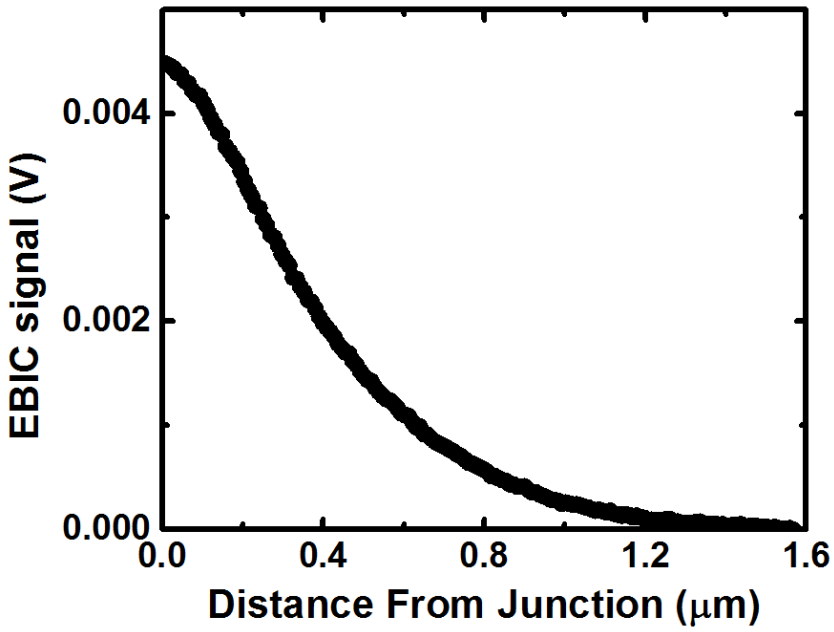

Figure 12. Experimental decay of the EBIC signal with distance from the junction.

Taking natural logarithm of the equation (7) gives:

$$ln(Id^{-\alpha}) = -\frac{d}{L} + ln(A) \quad (9)$$

The plot of Ln ($Id^{-\alpha}$) as a function of d is a straight line with slope equal to $-\frac{1}{L}$ as shown in Figure 13. The approach is accurate as long as d > 2L. The two asymptotic cases of $v_s = 0$ and $v_s = \infty$ were analyzed in reference [103] and found that $\alpha = -1/2$ for the former and $\alpha = -3/2$ for the latter. The exponential term in equation (7) is independent of α and dominates the values of I_{EBIC}, and therefore the chosen value of α between -1/2 and -3/2 can altered the value of diffusion length by only less than 20%. [104].

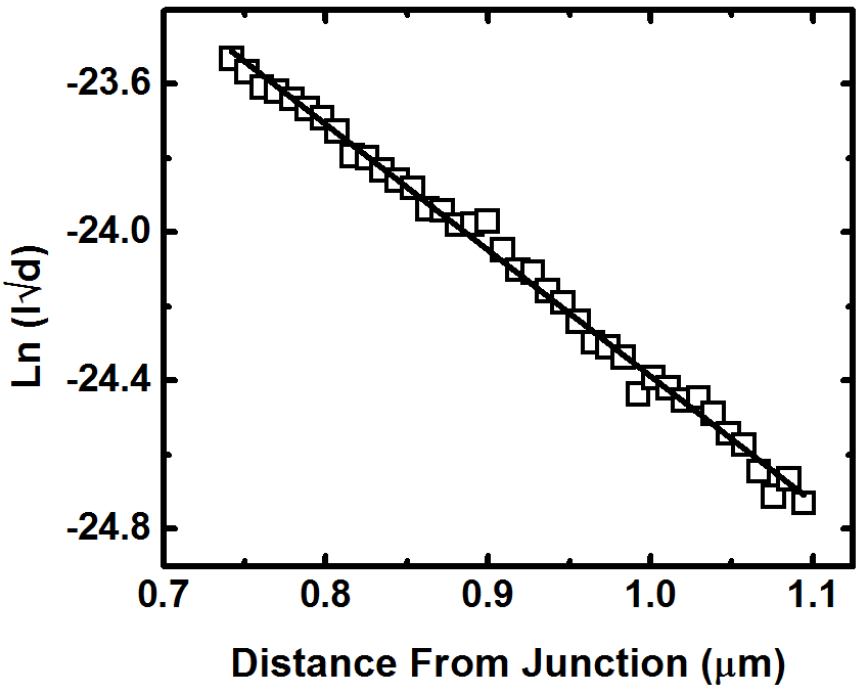

Figure 13. Diffusion length, L, can be determined from the linear relation between Ln (I√d) and d.

Also for III-Nitrides the diffusion coefficient is related to the temperature according to the equation:

$$D = D_o \, exp\,(-\frac{\Delta E_a}{kT}) \tag{10}$$

where ΔE_a is the activation energy for the process.

Using equation 8 and 9, Diffusion length can be related to the temperature by:

$$L = L_o \, exp\,(-\frac{\Delta E_a}{2\,kT}) \tag{11}$$

If Ln(L) is plotted as a function of 1/2kT then the slope of the curve is equal to the activation energy of the sample as shown in Figure 14.

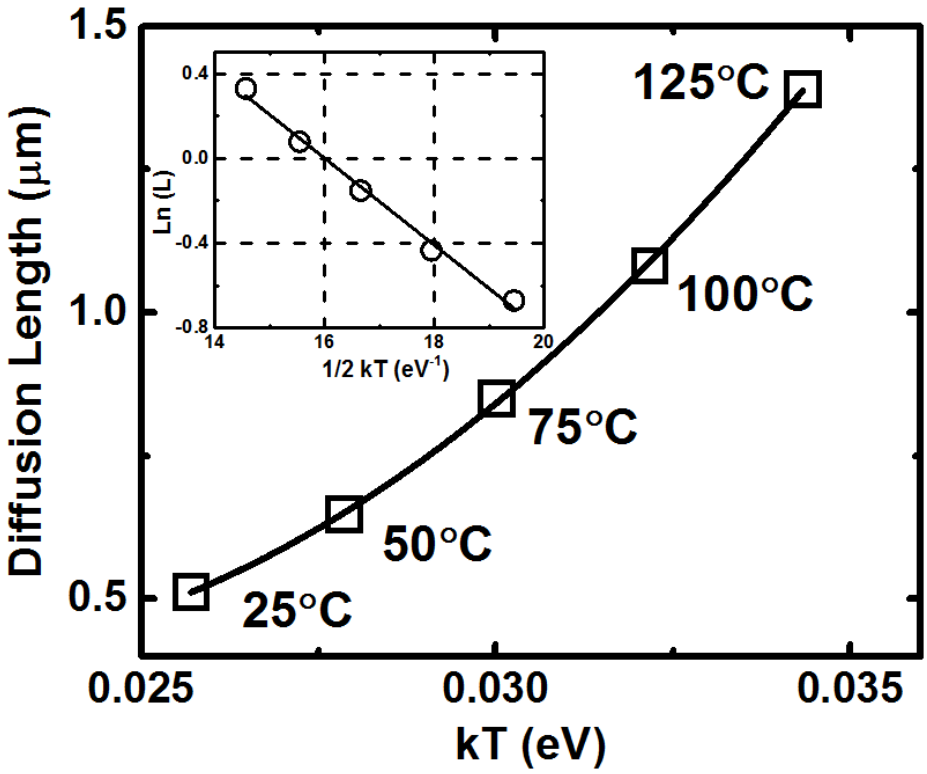

Figure 14. Temperature dependence of the diffusion length in AlGaN/GaN HEMTs. Inset: Arrhenius plot of the same data resulting in a value for activation energy of 204 ± 10 meV.

2.4 Cathodoluminescence

Cathodoluminescence (CL) is an optical and electromagnetic phenomenon which results in the emission of photons of characteristic wavelength when a semiconductor is bombarded by a high energy electron beam. Interaction of the electron beam with a semiconductor results in the promotion of electrons from the valence band, across the forbidden gap, into the conduction band. Electron-hole pairs are originated directly by the primary electron beam but also to a large extent by the other charge carriers created in the electron beam interaction volume. When the promoted electron and a hole recombine, it is not necessary that a photon has to be emitted. The probability of an emission of a photon and not a phonon depends on the material, its purity, and its defect state. The energy of the photon emitted has the characteristic of the composition and

structure of the exposed semiconductor, which provides information about its optical and electric properties. Figure 15 shows the schematic diagram of CL system.

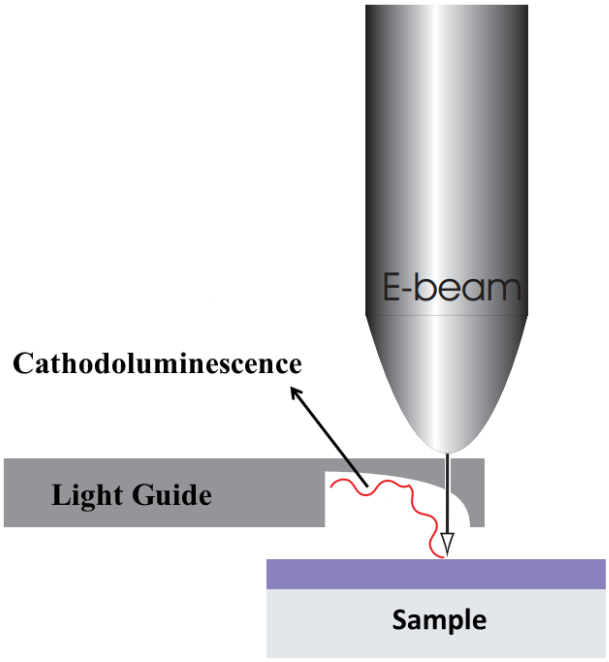

Figure 15. Schematic diagram of typical CL detection system with parabolic shape mirror.

2.4.1 CL Experimental Setup

CL measurements for this research were carried out in a Philips XL 30 Scanning Electron Microscope (SEM) equipped with Gatan monoCL3 system. This CL system collects the emitted photons using a retractable parabolic collection mirror followed by an optical monochromator. The mirror has a hole in it which allows the electron beam to pass directly to the sample while still allowing secondary electron imaging at a reduced efficiency. To get the most efficient collection, the sample should be placed on the focal point of the mirror. The parabolic shape of the mirror reflects the light as a parallel beam into the waveguide. There are two modes of detection for MonoCL3 system. To get a spectrum or to make an image at one particular wavelength, the monochromator mode is used in which light is led through a monochromator,

while in the panchromatic mode all the emitted light is collected by the detector. Two mirrors are used to switch between these two modes. The entrance and exit slits of the monochromator system can be changed from outside using micrometers to adjust the signal strength and spectral resolution. The emitted photons were collected using a single grating (1200 lines/mm, blazed at 500nm) and a Hamamatsu photomultiplier tube (PMT) sensitive to wavelengths ranging from 185-850. Gatan Digital MicrographTM software is used for the visualization and manipulation of CL spectrum. Step-size, dwell time and other spectral parameters can be controlled using the software. The temperature of the sample was varied by 25° C in-situ by the external temperature controller. Figure 16 shows the systematic diagram photo of the installed apparatus and a schematic diagram of the CL system optics is shown in Figure 17. The electron beam can be used either in a spot mode or scan mode. New positon is chosen for each measurement in order to avoid contamination from the SEM electron beam.

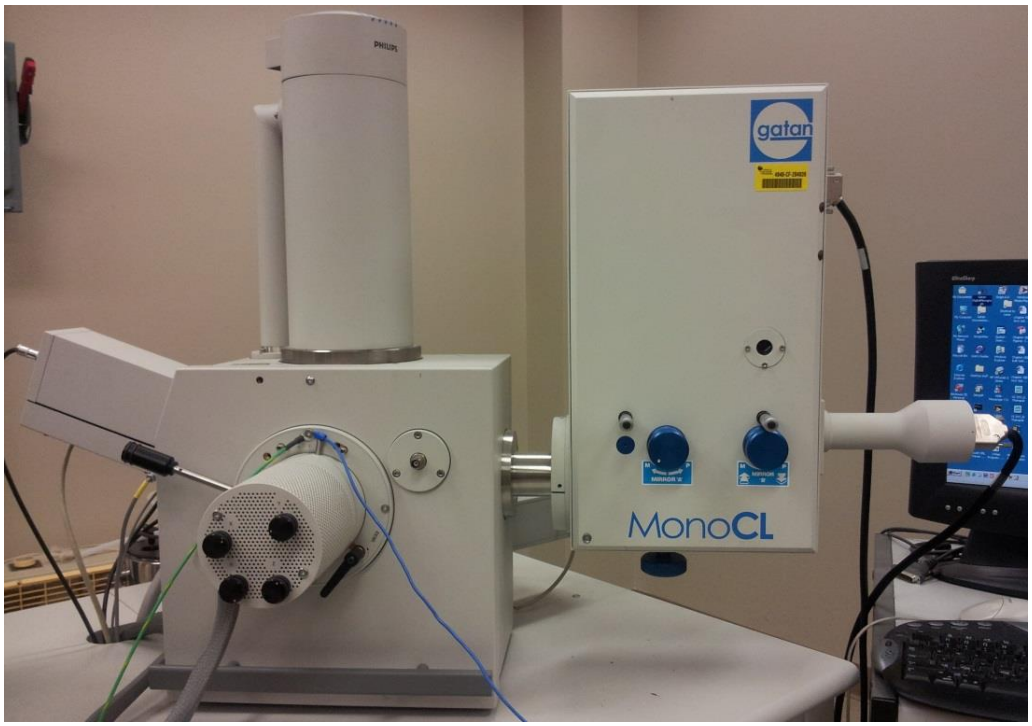

Figure 16. Gatan MonoCL3 cathodoluminescence system installed on the SEM located.

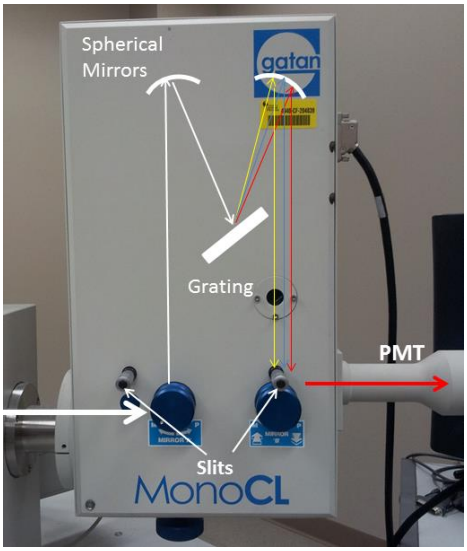

Figure 17. A diagram showing the path of the light through the Gatan MonoCL3.

2.4.2 Activation Energy from CL

To calculate the thermal activation energy, temperature dependent CL measurements are performed. Near band edge intensities approximately follow an exponential decay with increasing temperature, as expected from the formula [105, 106]:

$$I = \frac{A}{(1 + B\ exp\ (-\frac{\Delta E_a}{kT})} \tag{12}$$

where I is the intensity, A and B are temperature independent constant, ΔE_a is the activation energy, k is the Boltzmann constant, and T is the temperature in kelvin. The activation energy must represent either a barrier to capture a carrier at non-radiative combination centers, or the thermal activation energy of such centers. At higher temperatures there is subsequent annihilation of non-equilibrium electron hole pairs generated by the SEM electron beam. It is observed that the frequency of recombination events (CL peak intensity) decreases as the temperature increases since the hole capture cross section is inversely proportional to temperature.

CHAPTER THREE: EXPERIMENTAL RESULTS AND ANALYSIS

3.1 Introduction

The radioactive decay of ^{60}Co yields gamma-photons, with energies of 1.17 and 1.33 MeV (with average energy of 1.25 MeV), which can cause indirect ionization in semiconductor materials through the Compton scattering. The average energy of the Compton electrons is approximately 600 keV, which is sufficiently energetic to displace Ga and N atom from their sub-lattice sites.

In this chapter, the results from the impact of gamma-irradiation on AlGaN/GaN HEMTs are presented. First section (Section 3.2) is devoted to understand the effects of high dose (above ~250 Gy) of ^{60}Co gamma-irradiation on AlGaN/GaN HEMTs. In this section, fundamental minority carrier transport properties of HEMTs were investigated before and after the gamma-irradiation through EBIC measurements. These measurements were able to provide critical information on defects induced in the material as result of gamma-irradiation. DC I-V measurements were also conducted in parallel to assess the impact of gamma-irradiation on transfer, gate and drain characteristics. Further insight into the nature of radiation-induced defects, and the mechanisms involved in radiation-induced device degradation, has been obtained from post-irradiation thermal annealing after exposure to gamma-ray doses. Annealing experiments were performed with the goal of improving device performance and minority carrier transport after gamma-irradiation.

Second section (Section 3.3) presents the primary results from the four low dose (below ~250 Gy) experiments on AlGaN/GaN HEMTs. The first and second low dose gamma-irradiation experiments focused on the minority carrier transport characteristics of AlGaN/GaN

devices. The HEMT devices for these two experiments were grown by Molecular Beam Epitaxy and Metal Organic Chemical Vapor Deposition technique respectively. Temperature dependent EBIC measurements conducted on the devices to monitor the electronic carrier transport properties of the devices before and after exposure to gamma-irradiation. The low dose of gamma-irradiation measurements were made to separate the impact of internal Compton electron irradiation on transport properties and that of energetic gamma-irradiation induced extended and point defects. This investigation was conducted to assess the reproducibility of the observed effects, as well as to further gain insight into the enhancement induced by the primary gamma-photons.

The third and fourth low dose gamma-irradiation measurements were designed to extend and amplify the results from the first two experiments of low doses. Temperature dependent EBIC measurements were conducted to demonstrate the repeatability of the first two low dose experiments (Section 3.3.1 and 3.3.2). To complement EBIC measurements spatially resolved Cathodoluminescence measurements were carried out at variable temperatures. Similar to EBIC measurements, CL probing before and after gamma-irradiation provided the direct of evidence of the growing life time of non-equilibrium carriers. The results from the EBIC measurements are correlated with the CL measurements in order to demonstrate that same underlying process is responsible for the observed changes. The observations also help to understand the difference in effects induced by the low dose and high dose of gamma-irradiation.

Investigation of the gamma-irradiated device properties gives important information about defects in semiconductor heterostructures, especially if additional traps are introduced under external irradiation. At the same time, such investigation is very important not only from the fundamental point of view, due to obtaining substantial information on the physical

properties of semiconductor materials, but it also gives values of the device performance for application in radiation harsh environments.

3.2 High Dose Gamma-Irradiation Induced Effects on AlGaN/GaN HEMTs

The objective of this work was to understand the impact of high dose (above ~ 250 Gy) ^{60}Co gamma-irradiation on AlGaN/GaN HEMT's fundamental properties including carrier transport and recombination. The effects of ^{60}Co gamma-rays doses up to 1000 Gy on the transport properties of devices are reported through EBIC measurements, and then predictions are made to understand what defects may be responsible for the radiation effects. DC current-voltage measurements were also conducted on the transistors to assess the impact of gamma-irradiation on transfer, gate and drain characteristics. In addition, the effect of post-irradiation annealing at 200°C for 25 min was studied with the goal of improving device performance.

The following work was originally published in Applied Physics Letters [107] and Radiation Effects and Defects in Solids [108].

3.2.1 Experimental Details

The HEMTs employed in this study were epitaxially grown by Metal Organic Vapor Phase Epitaxy (MOVPE) technique on sapphire substrates using a Thomas Swann Reactor. A 2µm-thick carbon doped GaN buffer layer was followed by a 5 nm thick undoped GaN channel layer, 20 nm of $Al_{0.25}Ga_{0.75}N$, and capped with 2.5 nm GaN layer.

The devices were exposed to ^{60}Co gamma-rays doses starting from ~ 300 Gy to a maximum total dose of 1000 Gy. The device irradiations were carried out at room temperatures in nitrogen ambient. In order to avoid the influence of self-heating and high electric stress

effects, during the device's irradiation drain, source and gate contact kept electrically shorted. After the completion of the irradiation, the devices were kept at room temperatures for at least 48 hours to ensure settling the possible short-term instabilities due to irradiation.

A series of variable temperature dependent EBIC measurements were carried out in the vicinity of the HEMT gate. EBIC data were acquired by scanning the SEM electron beam along a line perpendicular to the edge of the gate contact. Line scan of 48 seconds were performed on the devices while EBIC measurements were performed to extract the diffusion length. The temperature dependent minority carrier diffusion length measurements were carried out from 25°C to 125°C using a hot stage and external temperature controller (Gatan). These measurements allowed the extraction of the activation energy for the temperature-induced enhancement of minority carrier transport which bears a signature of defect levels involved in the carrier recombination process. To refrain from unintentional influence of the electron beam, line scans were measured at different locations for each temperature. Figure 18 (a) and 18 (b) shows the device layout and the locations for the measurements. Figure 18 (c) represents the superimposed EBIC line scan and secondary electron image in the vicinity of the gate.

The DC current-voltage (I-V) characteristics of AlGaN/GaN HEMTs were carried measured predominately at room temperature using HP 4145 Semiconductor Parameter Analyzer. HEMTs characterization was carried out before as well as after the gamma-irradiation.

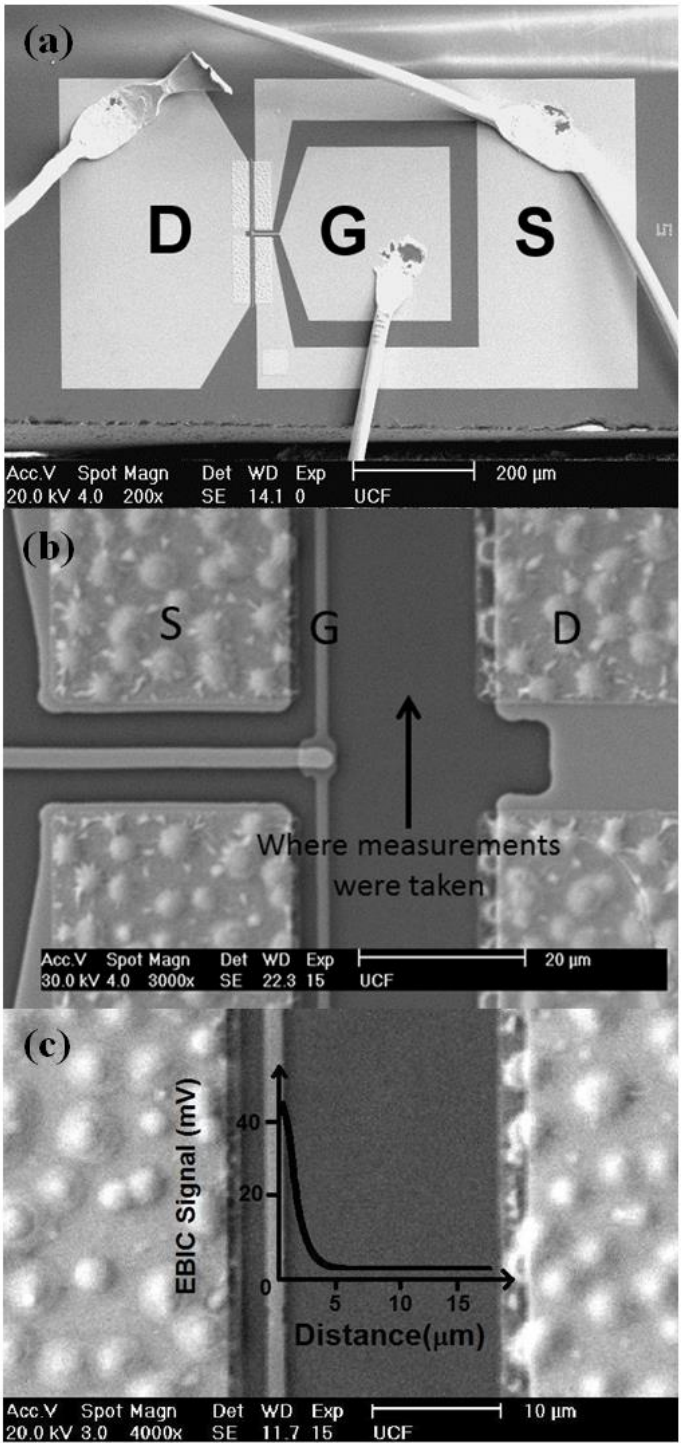

Figure 18. (a) SEM image of the AlGaN/GaN HEMT device layout. (b) SEM image indicating location for the EBIC measurements (c) SEM image with superimposed EBIC signal Vs distance.

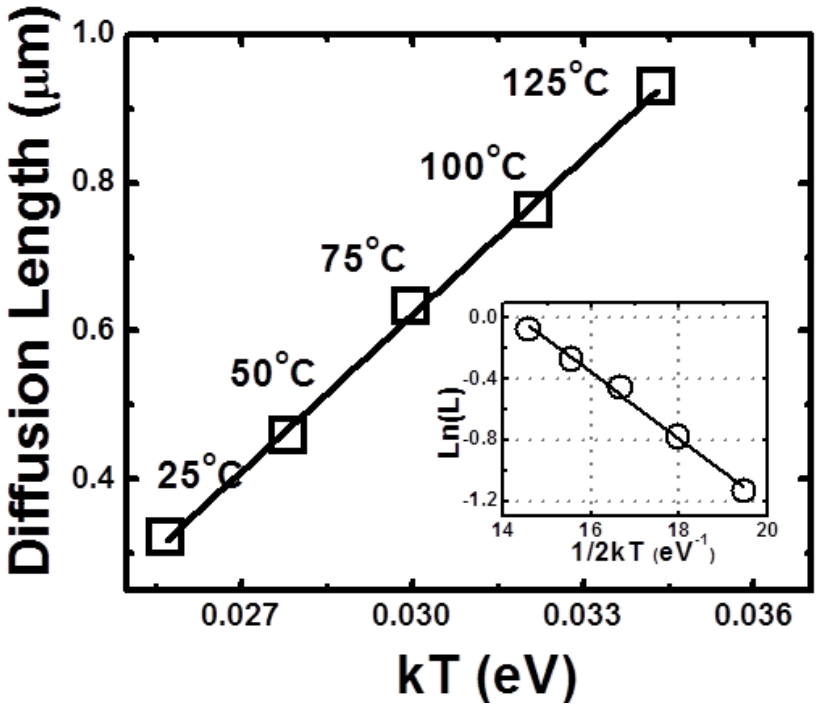

Figure 19. Temperature dependence of L for the AlGaN/GaN HEMT subjected to the highest dose of gamma-irradiation. Note: room temperature L values decreased from ~1 μm before irradiation, to ~0.35 μm after 1000 Gy dose of gamma- irradiation. Inset: Arrhenius plot of the same data yielding the activation energy, ΔE_a, of 216 ± 10 meV. ΔE_a, represents the carrier delocalization energy, which is related to the carrier recombination.

3.2.2 Impact of Gamma-Irradiation on Minority Carrier Transport Properties

By recording the exponential decay of EBIC as a function of distance from the gate, one can extract the value for the minority carrier diffusion length from equation (8). Minority carrier diffusion length, L, is an important temperature dependent parameter, which is sensitive to the density of the defects, created for example, as a result of gamma-irradiation. Figure 19 shows the typical dependence of minority carrier (hole) diffusion length on temperature for one of the AlGaN/GaN HEMTs subjected to the highest dose of gamma-irradiation. In semiconductors, an

exponential increase in the diffusion length with temperature is a common phenomenon and is modelled with the equation (11). The thermal activation energy was found from the Arrhenius plot to be 216 ± 10 meV. The increase in L at elevated temperature is associated with smaller recombination capture cross section for the non-equilibrium carriers. At high temperature there is subsequent annihilation of non-equilibrium electron hole pairs generated by the SEM electron beam. The frequency of recombination events decreases as the temperatures increases. This means that non-equilibrium hole carriers exists in the valence band for a longer period of time and therefore diffuse longer distance before recombination.

The influence of gamma-irradiation on minority carrier transport properties was monitored by the EBIC technique. The EBIC measurements were started prior to gamma-irradiation and then continued on the devices subjected to various doses of irradiation. Temperature dependent EBIC measurements yielded a decrease in diffusion length with dose, from 0.83 μm from the standard device to 0.32 μm from the device exposed to the highest dose, with a corresponding increase in activation energies, 106 meV for the standard to 216 meV for the device exposed to the highest dose as shown in Figure 20. An increase in activation energy with gamma-irradiation provides insights into the creation of deeper gamma-irradiation induced defect levels in the AlGaN/GaN devices. 0.6 MeV Compton electrons, generated by the gamma-irradiation are likely to create nitrogen vacancy-related defects in GaN layers. These types of defects are reported after low-energy proton, electron and gamma-irradiation [6, 34, 95].

Electron- irradiation induced nitrogen vacancy related defects have been reported with activation energy values ranging from 150 meV to 260 meV in GaN after 1 MeV electron irradiation [95]. In this work, activation energies were also seen to increase from 106 ± 5 meV, for the reference device, to 216 ± 10 meV, for the device subjected to highest dose gamma-

irradiation dose. This increase of approximately 110 meV is most likely related to the creation of additional deep traps due to nitrogen vacancies, induced in AlGaN/GaN by gamma-irradiation. By forming these traps, these vacancies reduce the carrier concentration, thus, increasing the recombination related activation energy in the irradiated devices, which exhibits more degradation with gamma-irradiation dose. It should be noted that similar to this observation, an increase in activation energy with dose was previously reported for proton radiation defects in III-N layers [95].

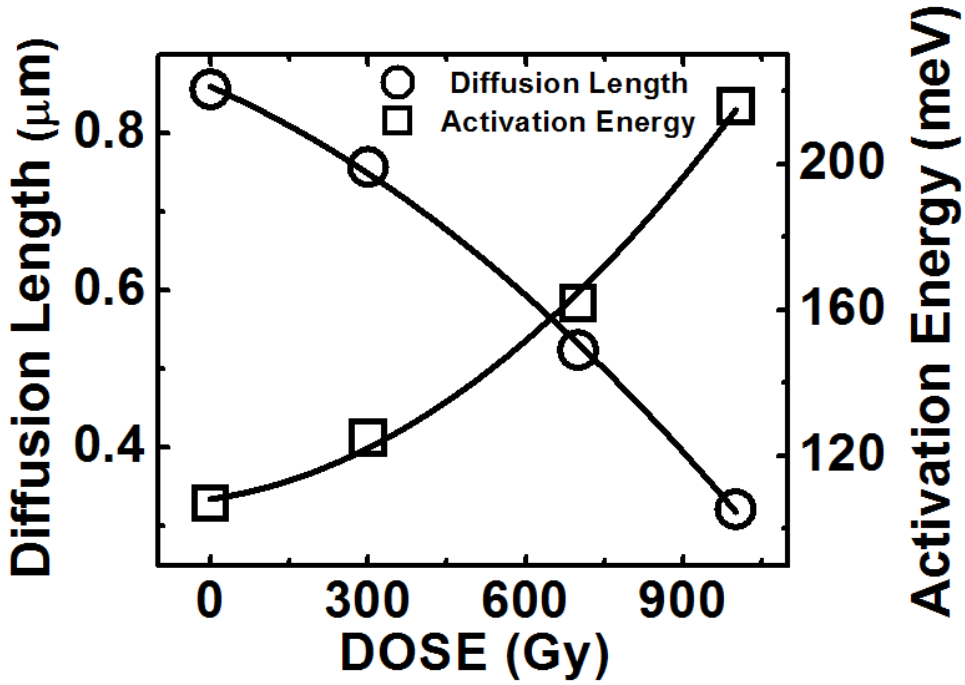

Figure 20. Left: Experimental dependence of minority carrier diffusion length in AlGaN/GaN HEMT on irradiation dose. The diffusion length consistently decreases as the dose of gamma-irradiation increases. Right: Dependence of calculated activation energy, ΔE_a, on irradiation dose. Note: activation energy increase indicates creation of deeper defects with the levels in the semiconductor forbidden gap as a result of gamma-irradiation.

3.2.3 Impact of Gamma-Irradiation on DC I-V Characteristics

Figure 21 (a) illustrates the drain I-V curves of AlGaN/GaN HEMT before and after 700 Gy dose of gamma-irradiation. The drain I-V curves were modulated by sweeping the gate voltage from 0 to -3 V with a step of -1 V. A reduction (after gamma-irradiation) in the drain current and transconductance as a function of device gate voltage was observed, due to an increased trapping of carriers and dispersion of charge. A positive shift of threshold voltage, V_{th}, is also seen in Figure 21 (a). Positive shift of 0.67 V, after 1000 Gy dose of gamma-irradiation, in the threshold voltage is mainly due to a decrease in the gate Schottky barrier height and a reduction of carrier concentration in the 2DEG channel, most likely because of radiation-induced damage at the metal-semiconductor interface. The shift in threshold voltage can be described using equation [23]:

$$V_{th} = V_{bi} - \frac{q(N_d + N_t)A^2}{2\varepsilon} \quad (13)$$

where V_{bi} is the built-in voltage ; q is the charge of the electrons; N_d is the carrier density in the 2-dimensional electron gas channel; N_t is the trap density; A is the thickness of the 2DEG channel; and ε is the dielectric constant of the AlGaN layer. Gamma-irradiation produces a net increase in (N_d + N_t) which results in positive shift of threshold voltage. Figure 21 (b) compares I_{DS} versus V_{DS} characteristics of pre-irradiated and device irradiated with 700 Gy gamma-ray dose. Decrease in the drain current is related to the dispersion of charge. Figure 21 (c) illustrates the gate I-V characteristics of AlGaN/GaN HEMTs before and after the irradiation. The gate I-Vs were measured by sweeping the gate voltage from +1 to -10 V, grounding the source electrode and floating the drain electrode. A significant increase in gate leakage current after irradiation was observed for both forward and reverse directions.

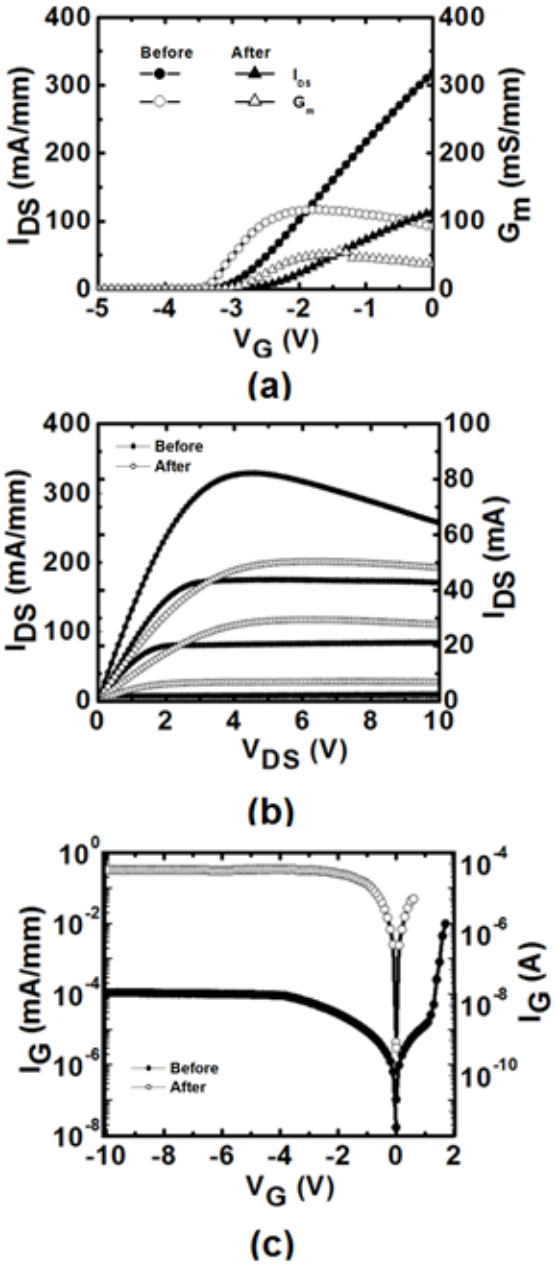

Figure 21. DC I-V characteristics of AlGaN/GaN HEMTs before and after the gamma-irradiation with a dose of 700 Gy. (a) Transfer characteristics measured under V_{DS} = +5 V. (b) Drain characteristics measured under the initial V_G = 0V (upper curve) with the increment of -1 V. (c) Gate characteristics under forward and reverse bias before and after irradiation.

Table 7 summarizes the relation between dose, diffusion length decrease, activation energy increase, and changes in DC I-V characteristics. The decrease in diffusion length and increase in activation after gamma-irradiation are related the creation of deeper gamma-irradiation induced defect levels most likely associated with nitrogen vacancies. Gamma-irradiation causes a decrease in the drain current, trans-conductance, an increase in gate leakage current. Table 7 shows the drain current and transconductance percentage decrease as a function of gamma-irradiation dose The HEMTs degrades, because gamma-irradiation introduces deeper defect levels, which leads to an increased trapping of carriers and dispersion of charge.

Table 7 Impact of gamma-irradiation on the figures of merit of AlGaN/GaN HEMTs. ΔI_{DS} (%) was calculated from Figure 21 (b) at V_{DS} = 5V for the top I-V branches before and after irradiation. ΔG_m (%) was calculated from Figure 21 (a) using the peak trans-conductance values before and after the irradiation.

	Reference Sample	**Sample A**	**Sample B**	**Sample C**
γ-dose	0	300	700	1000
Diffusion length (μm)	0.85 ± 0.07	0.76 ± 0.03	0.52 ± 0.05	0.32 ± 0.03
Activation Energy (meV)	105.7 ± 5.1	125.2 ± 3.8	162.3 ± 9.9	216.1 ± 10
ΔI_{DS} (%)	0	-16.5	-37.5	-56.9
ΔG_m (%)	0	-37.9	-54.0	-74.1
ΔV_{th} (%)	0	0.1	0.44	0.67

3.2.4 Post Irradiation Annealing

Gamma-irradiated MOVPE grown AlGaN/GaN HEMTs were annealed at 200° C for 25 minutes following irradiation. The DC and EBIC measurements were then repeated to study the impact of annealing on these devices. The results of EBIC measurements after gamma-irradiation and after annealing treatment are summarized in Table 8.

Table 8 Impact of gamma-irradiation and annealing (200°C / 25 min) on the minority carrier diffusion length and activation energy of MOVPE AlGaN/GaN HEMTs.

	Reference Sample	**Sample A**	**Sample B**	**Sample C**
γ-Dose (Gy)	0	300	700	1000
Diffusion Length, L (μm) after irradiation	0.85± 0.07	0.76 ± 0.03	0.52 ± 0.05	0.32 ± 0.03
ΔE_a (meV) after irradiation	105.7 ± 5.1	125.2 ± 3.8	162.3 ± 9.9	216.1 ± 10.0
Diffusion Length, L (μm) after irradiation followed by annealing	0.85 ± 0.07	0.82 ± 0.06	0.64 ± 0.02	0.44 ± 0.04
ΔE_a (meV) after irradiation followed by annealing	105.7 ± 5.1	100.4 ± 6.4	115.6 ± 10.2	131.6 ± 4.0

The decrease in diffusion length and increase in the activation energy after the gamma-irradiation is related to the creation of deeper gamma-irradiation induced defect levels most likely associated with nitrogen vacancies. The increase in diffusion length from 0.32 μm to 0.44 μm and decrease in the activation energy from 216.1 to 131.6 meV for the highest dose of gamma-irradiation after annealing indicates device recovery. It is evident from Table 8 that annealing of gamma-irradiated HEMTs at 200°C for 25 minutes leads to the recovery (depending

on the dose) of minority carrier diffusion length. The recovery is also reflected in the activation energy returning to its pre-irradiated value.

Figure 22 shows the experimental dependence of diffusion length and activation energy on the dose of gamma-irradiation both before and annealing treatment. Upon annealing, all gamma-irradiated devices show an increase in diffusion length with a corresponding decrease in the activation energy. Increases in diffusion had been attributed to a reduction in point defects (nitrogen vacancies) induced in AlGaN/GaN by gamma-irradiation.

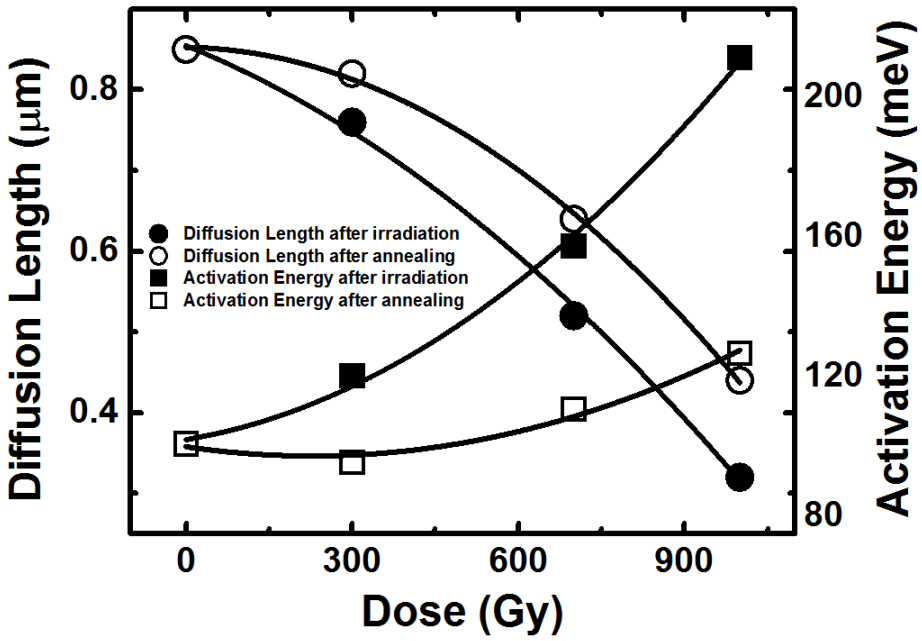

Figure 22. Left Axis: Experimental dependence of minority carrier diffusion length, L, in AlGaN/GaN HEMTs, grown by MOVPE, on irradiation dose. Right Axis: Dependence of calculated activation energy, ΔE_a, on irradiation dose. L and ΔE_a after annealing following irradiation are shown by open squares and circles, respectively.

The level of recovery of gamma-irradiated devices after annealing depends on the dose of the irradiation. The devices that show most recovery for this particular annealing temperature are those exposed to low doses. On the material's level, the recovery of devices is evident from the significant increase in the diffusion length after annealing. Induced nitrogen vacancy defects after the gamma-irradiation reduce the carrier concentration and mobility of charge carriers and therefore increase the activation energy related to carrier recombination. After annealing, the number of defects is reduced, resulting in an increase in diffusion length.

Figure 23 shows the results of the transfer, gate and drain characteristics for AlGaN/GaN HEMT before irradiation, after irradiation with a dose of 800 Gy and after annealing following gamma-irradiation. Gamma-irradiation causes a decrease in the drain current, trans-conductance and an increase in gate leakage current. The HEMT devices degrade, because gamma-irradiation introduces deeper defect levels. However, annealing of gamma-irradiated HEMT at 200°C for 25 min shows that partial recovery of device performance is possible at this temperature. Figure 23 (a) and 23 (b) exhibits the recovery of the drain current and trans-conductance after annealing. Figure 23 (c) illustrates that moderate annealing leads to the slight decrease in the gate leakage current.

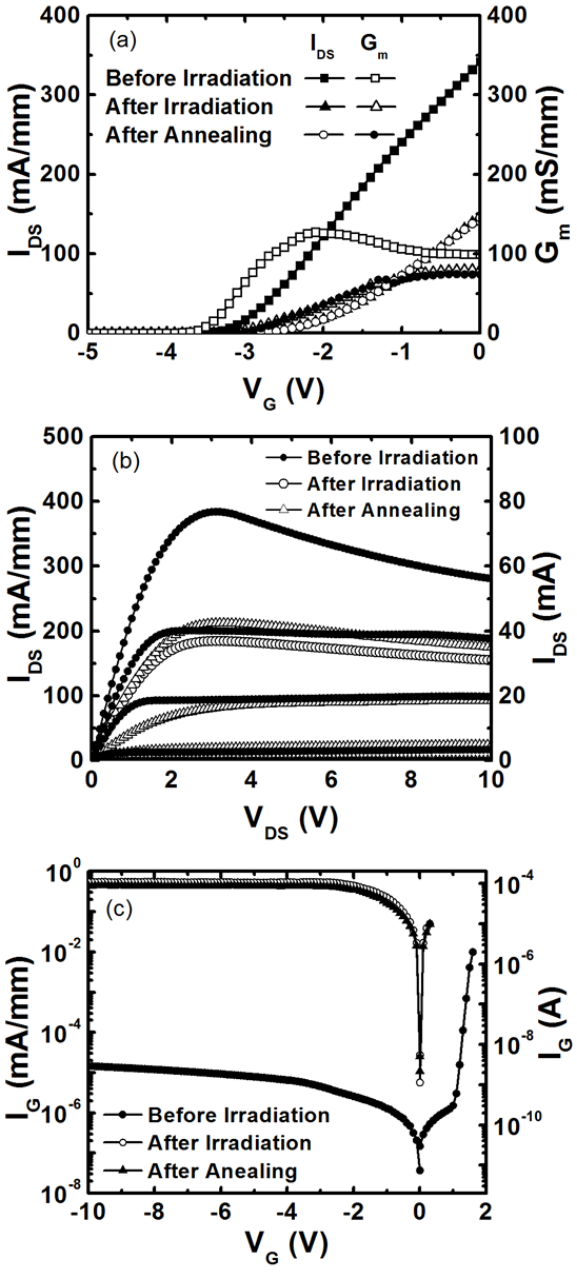

Figure 23. DC I-V characteristics for MOVPE AlGaN/GaN HEMT before irradiation after irradiation with a dose of 800 Gy and after annealing (200° C for 25 min) following gamma-irradiation. (a) Transfer characteristics measured under V_{DS} = +5 V. (b) Drain characteristics measured under the initial .V_G = 0V with the increment of -1 V. (c) Gate characteristics under forward and reverse bias.

Table 9 Impact of annealing (200°C/25 min) on gamma-irradiated MOVPE HEMT performance.

γ-Dose (Gy)	100	500	800	1000
Δ I_{DS} after irradiation (%)	-18	-36	-44	-56.9
Δ I_{DS} after annealing (%)	+17	+15	+13	0
Δ G_m after irradiation (%)	-31	-44	-45	-74.1
Δ G_m after annealing (%)	+14	+10	0	0
Δ V_{th} after irradiation (V)	+0.1	+0.38	+0.41	+0.67
Δ V_{th} after annealing (V)	-0.05	-0.01	0	0

Table 9 summaries the impact of annealing on HEMTs performance. The changes in parameters for irradiated devices were compared with those before irradiation. The changes in the same parameters after annealing following the irradiation were compared with those before annealing (after irradiation). After the devices were annealed at 200° C, we observed an increase in both the drain current and the trans-conductance, suggesting that the atoms in the gamma-irradiated device were rearranged due to the annealing effect. After annealing, a change of 5% is observed in the threshold voltage of the device irradiated with 100 Gy gamma-ray dose. As seen from Table 9, the recovery of the device depends on the dose of the gamma-irradiation. The devices that show the most recovery for a particular annealing temperature are those exposed to the lowest dose of the gamma-irradiation, while those exposed to the high dose of gamma-irradiation results in no recovery of performance. The latter fact indicates that a higher device annealing temperature is needed for larger doses of gamma-irradiation.

3.3 Low Dose Gamma-Irradiation Induced Effects in AlGaN/GaN HEMTs

Previous section considers the effects of high dose ^{60}Co gamma-irradiation on AlGaN/GaN HEMTs. The results obtained shows the degradation of the devices, which is related to the creation of deep defect levels due to nitrogen vacancies induced by gamma-irradiation. But the obtained results in the last section did not consider the information between 0 and 300 Gy. However, this section fills the informational gap as far as low dose gamma-irradiation between 0 and 300 Gy is concerned.

This section presents the results obtained in the investigation of four low dose (below ~250 Gy) gamma-irradiation induced effects in AlGaN/GaN HEMTs. The results are grouped according to individual set of measurements performed on different devices. Analysis is presented along with the experimental observations. In contrast to results obtained from the high doses, irradiation by low dose gamma-photons demonstrate improvement of minority carrier transport characteristics due to internal irradiation by Compton electrons, induced by the gamma-irradiation.

The low dose of gamma-irradiation was needed to separate the impact of Compton-electron irradiation effect and that of energetic gamma-irradiation induced extended and point defects. Understanding the effects arising under low dose of gamma-irradiation has not only provided the information about the charge carrier transport but has given substantial information for improving the device performance. This finding has significant importance in wide band gap technology, since understanding the radiation defects with various doses of gamma-irradiation provides an opportunity in determining device performance and reliability, especially for space borne applications.

The following work was originally published in Radiation Effects and Defects in Solids [108], Material Research Proceedings [109] and Electrochemical Society Transactions [110].

3.3.1 First Low Dose Gamma-Irradiation Experiment

The influence of ^{60}Co gamma-irradiation on minority carrier transport and DC characteristics of MBE grown HEMTs were conducted prior to and after the gamma-irradiation. Main effects on the HEMTs after low dose irradiation (below ~250 Gy) were increase of both drain current and diffusion length. The increase in diffusion length and drain current for gamma-irradiated devices could be due to the induced Compton electrons, which will be discussed in details in subsequent section.

3.3.1.1 Device Preparation

AlGaN/GaN HEMTs layer structures were grown on c-plane Al_2O_3 substrate by Molecular Beam Epitaxy (MBE) at the University of Florida. The layer structure consisted of a thin AlGaN nucleation layer followed with a 2 μm thick undoped GaN buffer topped by a 25 nm thick unintentionally doped AlGaN layer. The mobility was determined to be 1080 $cm^2/V\text{-}s$ with a sheet carrier concentration of ~ 1 x 10^{13} cm^{-2} by Hall measurements conducted at room temperature. Mesa isolation was achieved by using an inductively coupled plasma system with Ar/Cl_2- based discharges. The Ohmic contacts were formed by lifting-off e-beam evaporated Ti (200 Å)/Al (1000 Å)/Ni (400Å)/Au (800 Å). The contacts were annealed at 850° C for 45 s under a flowing N_2 ambient in Heatpulse 610T system. Standard lift-off of e-beam deposited Ni/Au was used for gate metallization. Plasma enhanced chemical vapor deposited SiN_x of 1000Å was used for device passivation and the crossover between the gate finger and gate contact pad. The final step was the deposition of e-beam evaporated Ti/Pt/Au (300 Å/ 200 Å/

2000 Å) metallization for interconnection contacts. Figure 21 shows SEM image of the circular AlGaN/GaN HEMT. The diameter of the circular gate finer was 100 µm, and the gate dimensions were 1.5 µm x 314 µm. The gate to source and gate to drain distance was kept at 2 and 4 µm, respectively.

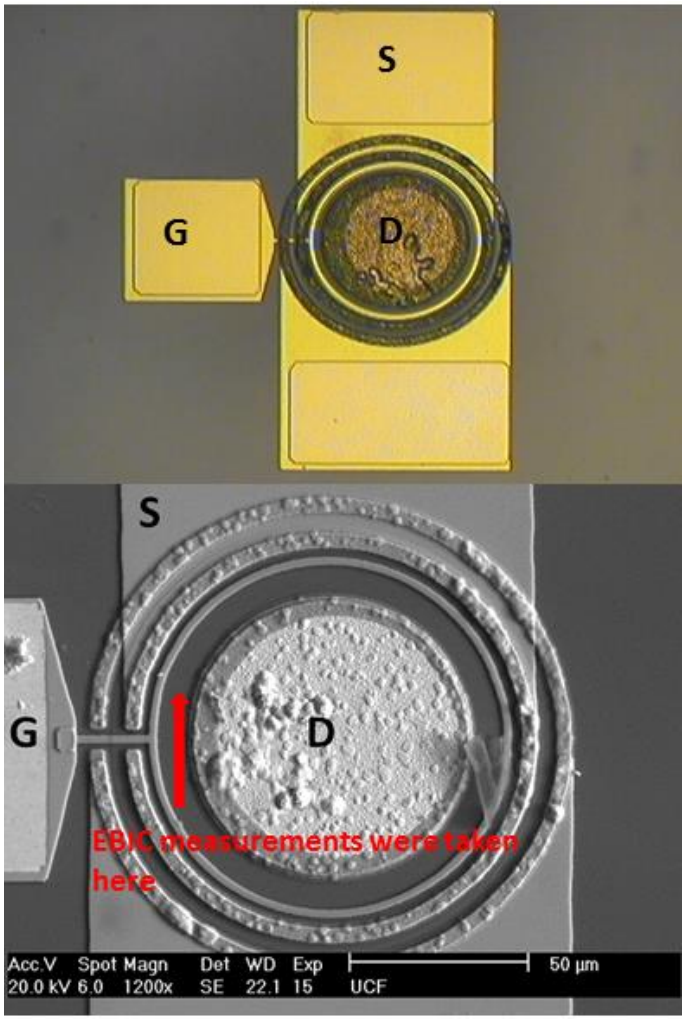

Figure 24. Device Configuration and SEM image of the circular AlGaN/GaN HEMTs showing the position of the EBIC measurements.

Anticipating possible charge-trapping effects at low doses, the devices studied in this Section (3.3.1) were exposed to cumulative ^{60}Co gamma-irradiation doses starting from a relatively low dose of 50 Gy to a maximum total dose of 700 Gy. Sample irradiation was performed in Nordion Science Advance Health ^{60}Co-irradiator, at 14 dose points at irradiation temperature <50° C. During device irradiation, the samples were held in nitrogen ambient, with drain, source and gate contacts kept electrically shorted during irradiation. It is noted that the density of photo electrons generated from the interaction of ^{60}Co-gamma rays with the protective lead wall of the Co-irradiator is expected to be low due to the Al filter of the chamber.

Minority carrier transport properties, before and after the irradiation, were studied using variable temperature EBIC measurements. The device dc performance was characterized using an Agilent 4156 Parameter Analyzer. Figure 24 shows the device layout and locations for the measurements.

3.3.1.2 Impact of Gamma-Irradiation on Minority Carrier Transport Properties

EBIC measurements were applied to study the temperature dependence of diffusion length. Data were acquired by scanning the electron beam of the SEM along a line perpendicular to the edge of the gate contacts and recording the exponential decay of the current. Scan time for all measurements were 48 second which is too short to induce any electron irradiation effect. The temperature of the sample was varied from 25^{o}C to 125^{o}C using a hot stage and an external temperature controller (Gatan). EBIC measurements performed on these MBE grown AlGaN/GaN HEMTs also revealed that the value of L increases exponentially as the temperature is raised, as seen in Figure 25. This behavior is consistent with that observed in earlier temperature dependent experiments on AlGaN/GaN HEMTs (Section 3.2.1) and also described

by the equation (11) using $\alpha = -1/2$. Measurements were carried out between the gate and source under a 20 kV accelerating voltage. These measurements allowed for the extraction of the activation energy for the temperature-induced enhancement of minority carrier transport. Similar to MOVPE grown AlGaN/GaN HEMTs, ΔE_a, represents carrier delocalization energy and serves as a parameter for determining the increase in diffusion length due to the reduction in recombination efficiency. Earlier EBIC studies on AlGaN/GaN HEMTs had also shown that the increase in minority carrier hole life-time with temperature is related to the smaller recombination capture cross section.

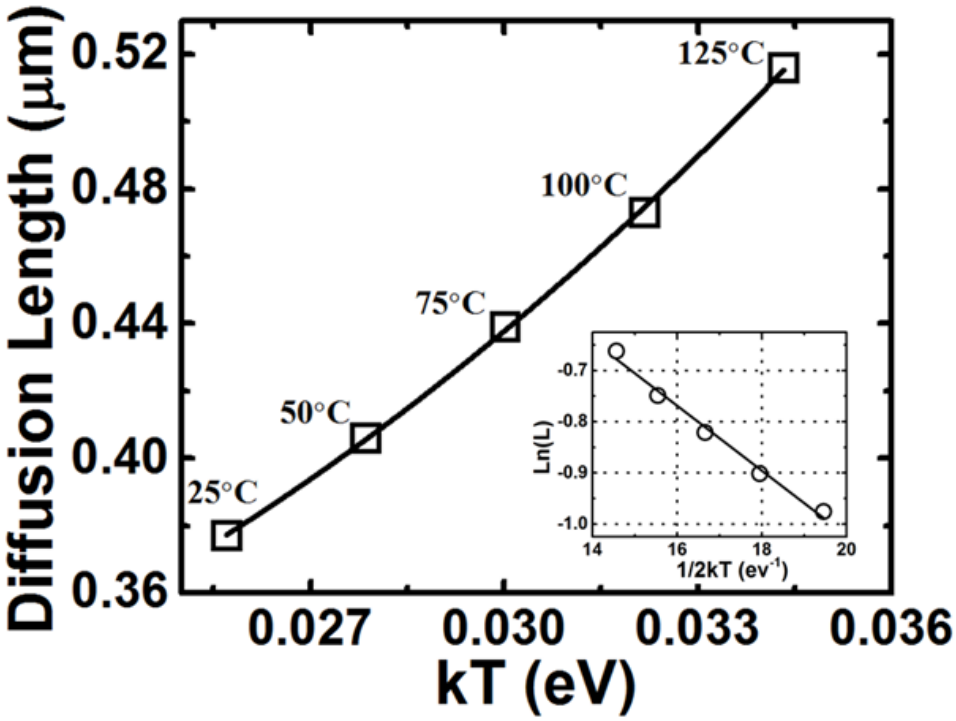

Figure 25. Diffusion length of minority holes as a function of temperature in AlGaN/GaN HEMTs (open squares) and the fit using equation (10) (solid line). Inset: Arrhenius plot of the same data yielding activation energy.

To understand the low dose gamma-irradiation effects on minority carrier transport properties, EBIC measurements were performed on AlGaN/GaN HEMTs. The EBIC measurements were started prior to gamma-irradiation and then continued on devices subjected to various doses of irradiation. Comparing the activation energy before and after gamma-irradiation identified the defect levels and their dependence on the dose of irradiation.

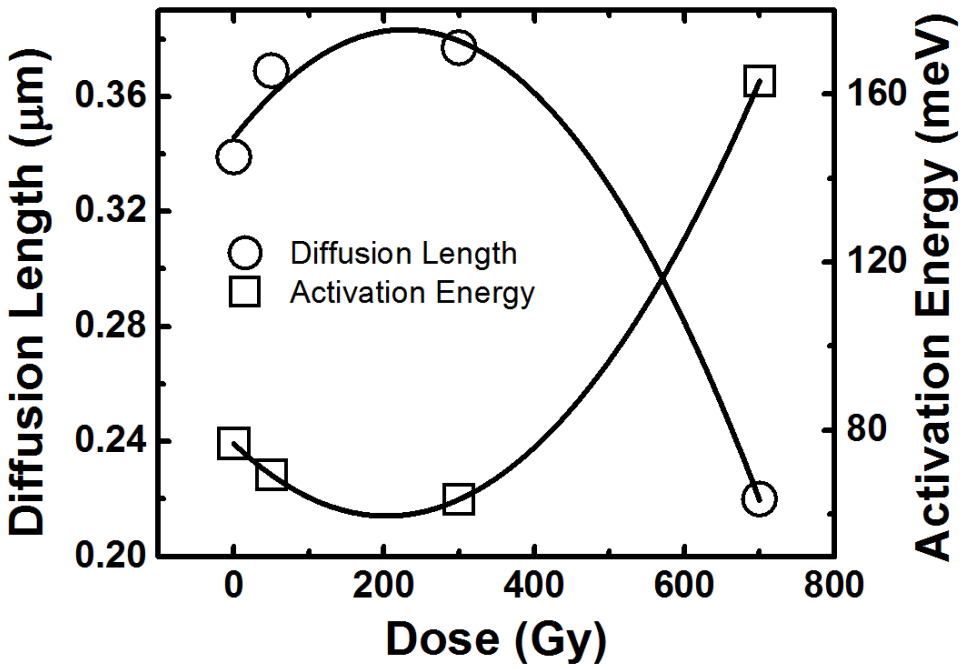

Figure 26. Impact of low dose gamma-irradiation on minority carrier transport (left axis) and associated activation energy (right axis) in AlGaN/GaN HEMT grown by Molecular Beam Epitaxy (MBE).

Figure 26 summarizes the studies of minority carrier transport under low dose of gamma-irradiation for MBE-grown HEMTs. In contrast to the behavior observed in Figure 20 one can see from Figure 26 that the diffusion length of minority carriers exhibits an initial increase for the dose up to 300 Gy before it starts decreasing. The activation energy, also in contrast to Figure 20 exhibits a decrease up to 300 Gy. The behavior in Figure 26 for a low dose of gamma-

irradiation is explained by the phenomenon of internal electron injection and subsequent trapping of Compton electrons on neutral levels, most likely related to nitrogen vacancies.

The primary defects created in AlGaN/GaN HEMTs by gamma-irradiation are Frenkel pairs, produced by Compton electrons having a mean energy of 600 keV. In this respect, gamma-irradiation, in term of its impact, is analogical to internal electron irradiation. The internal electron irradiation by Compton electrons is similar to the irradiation by external electrons produced, for example, by electron beam. The phenomenon of external electron irradiation in GaN material has been previously studied and reported earlier in literature [38, 111, 112]. The key points for the minority carrier transport enhancement for low doses due to internal electron irradiation are as follows:

Compton electrons, generated by in the material by the primary gamma-irradiation are likely to create donor type nitrogen vacancy related defects. Generally, non-equilibrium electrons recombine with holes in the valence band either through band to band transition or a transition that involves neutral metastable levels. However, if an electron is trapped by one of the defect levels, the latter can no longer provides a recombination pathway. As more defects are created due to higher irradiation, more of the non-equilibrium electrons become trapped and recombination cannot proceed through occupied levels. A consequence of slower recombination is an increase in life time, τ, for non-equilibrium carriers in the band (electrons in the conduction band and holes in the valence band) and, as a result, to an increase in diffusion length L, ($L = \sqrt{D\tau}$, where D is the carrier diffusivity).

For gamma-irradiation doses above ~250 Gy, a different phenomenon becomes dominant, which changes the tendency of the diffusion length. The concentration of point

defects, such as nitrogen vacancies, as well as the complexes involving native defects is expected to increase after irradiation. The growth in the trap density causes more frequent ionized impurity (or defect) scattering of the charge carriers which result in the degradation of the carrier mobility (μ). Carrier diffusivity ($D = \frac{kT}{q}\mu$) is a mobility dependent parameter which is directly related to diffusion length($L = \sqrt{D\tau}$). Decrease in diffusion length above ~ 250 Gy is explained via a decrease in the carrier mobility due to the creation of large number of trap states throughout the structure. For high doses of gamma-irradiation, non-equilibrium carrier scattering on radiation induced defects dominates the irradiation induced carrier life-time. Therefore, a decrease in the diffusion length is observed for higher doses in Figure 26. A corresponding increase in the diffusion length activation energy (obtained from the EBIC measurements) observed in Figure (20 and 26) at doses higher than ~250 Gy is related to the involvement of deeper (as compared to the initial irradiation situation) defect created as gamma-irradiation progresses. Note that gamma-irradiation-induced generation of extended defects is also not excluded and could affect the diffusion length and corresponding activation energy. Details on impact of extended defects on minority carrier transport are given in [113].

Figure 27 (a) illustrate the transfer characteristics of AlGaN/GaN HEMTs before and after the 300 Gy dose of gamma-irradiation. For Figure 27 (b) the drain I-V curves were modulated by sweeping the gate voltage from 0 to -3 V with a step of -1 V. The drain saturation current increased from 293 to 382 mA/mm after 50 Gy dose and to 357 mA/mm after 300 Gy dose of gamma-irradiation. Different mechanisms were proposed in the literature to explain such an increase in the current. It is suggested that Compton electrons induced from gamma-irradiations creates donor type defects in the material. These defects are supposed to be nitrogen vacancies that can have activation energy of 80 meV. These vacancies act as a donor and can

contribute electrons to the channel under the gate. It is expected that the density of these defects are small enough not to affect the band bending of the polarization of GaN material. It is also reported that low dose of gamma-irradiation can partially relaxed the strain of AlGaN/GaN HEMTs and can enhance the electron mobility. Also, there are good chances that low dose of gamma-irradiation can produce a decrease of the electrical traps which is resulted an increase in the drain current.

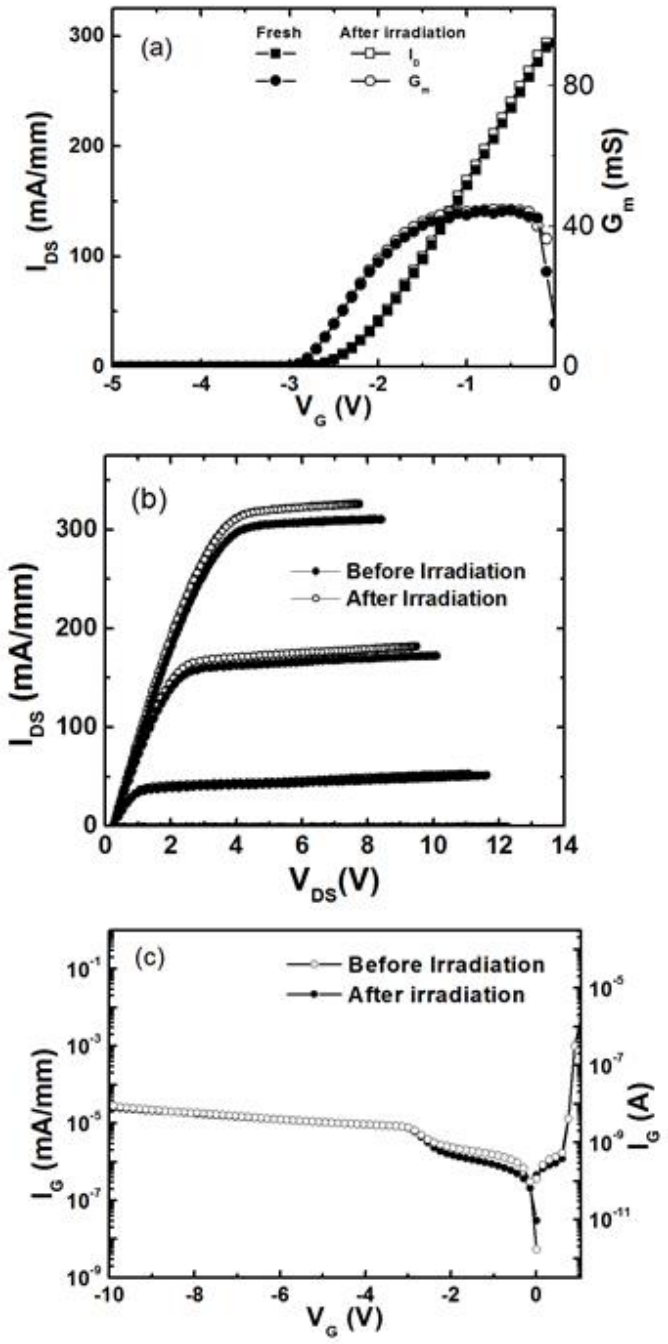

Figure 27. DC I-V Characteristics of AlGaN/GaN HEMTs before and after the gamma-irradiation dose of 300 Gy. (a) Transferred characteristics measured under VDS = +5 V (b) Drain characteristics with initial 0V gate voltage with the increment of -1 V. (c) Gate characteristics under forward and reverse bias.

3.3.2 Second Low Dose Gamma-Irradiation Experiment

To assess the reproducibility of the effects observed from the first experiment on the low dose of gamma-irradiation (Section 3.3.1), as well as to further gain insight into the enhancement induced by the primary gamma-photons; Temperature dependent EBIC experiments were carried out on four Metal-Organic Chemical Vapor Deposition (MOVPE) HEMTs.

3.3.2.1 Device Preparation

The HEMT on Si wafers were grown by Metal Organic Chemical Vapor Deposition (MOCVD) with conventional precursors in a cold-wall, rotating- disc reactor designed from flow dynamic simulations. The growth process was nucleated with an AlN layer to avoid unwanted Ga-Si interactions. The epitaxial stack consisted of an AlGaN transition layer, ~800-nm GaN buffer layer, and 16-nm unintentional-doped $Al_{0.26}Ga_{0.74}N$ barrier layer. The nominal growth temperature for the GaN buffer and AlGaN barrier layers was 1030ºC.

HEMT fabrication began with Ti/Al/Ni/Au Ohmic metallization and RTA in flowing N_2 at approximately 825ºC. Contact resistance, specific contact resistivity, and specific on-resistance were 0.45 Ω-mm, $5x10^{-6}$ Ω-cm^2, and 2.2 Ω-mm, respectively. Inter-device isolation was accomplished by use of a multiple energy N^+ implantation to produce significant lattice damage throughout the thickness of the GaN buffer layer. The ion implantation step maintains a planar geometry in the fabricated device and reduces parasitic leakage paths that may exist in passivated, mesa-isolated HFETs. Immediately following implantation, the wafers were passivated with 70-nm-thick SiN_x in a PECVD chamber maintained at a base plate temperature of 300 ºC. Schottky gate definition was achieved by patterning the gate and selectively removing the SiN_x passivation layer. The contact windows to the Ohmic contact pads were also opened at

the same time as defining the Schottky gate. After SiN_x etching, wider gate patterns were redefined with another photolithography step and contact windows to the Ohmic contact pads were also opened. Ni/Au-based gate metallization was deposited on the gate and Ohmic contact pads simultaneously. The wafers were then passivated with another 400-nm layer of PECVD SiN_x at 300 ºC. The contact windows were opened by dry etching. There was an additional metal deposition for the HEMT with the source field plate. The field plate was connected to the source terminal and extended by 1 µm out over the gate to the gate-to-drain region. The source to gate distance and channel length of the HEMTs with and without the source field plate were kept constant at 1 and 4.7 µm, respectively.

Devices were exposed to cumulative ^{60}Co gamma-irradiation doses of 100, 200 and 300 Gy. Sample irradiation was performed by NORDION, Inc., at room temperature. During the device irradiation, the samples were held in nitrogen ambient, with drain, gate and source contacts kept electrically shorted in order to avoid the influence of self-heating and high electrical field stress effects.

To understand the gamma-irradiation effect on minority carrier transport properties, Electron Beam Induced Current (EBIC) measurements were performed on AlGaN/GaN HEMTs. The EBIC measurements were started prior to gamma-irradiation and then continued on devices subjected to various doses of irradiation. Measurements were carried out between the gate and source under a 20 kV accelerating voltage. Figure 27 (a), (b) shows the device layout and location for measurements. Figure 27(c) represents the superimposed EBIC line scan and secondary electron image in the vicinity of the gate.

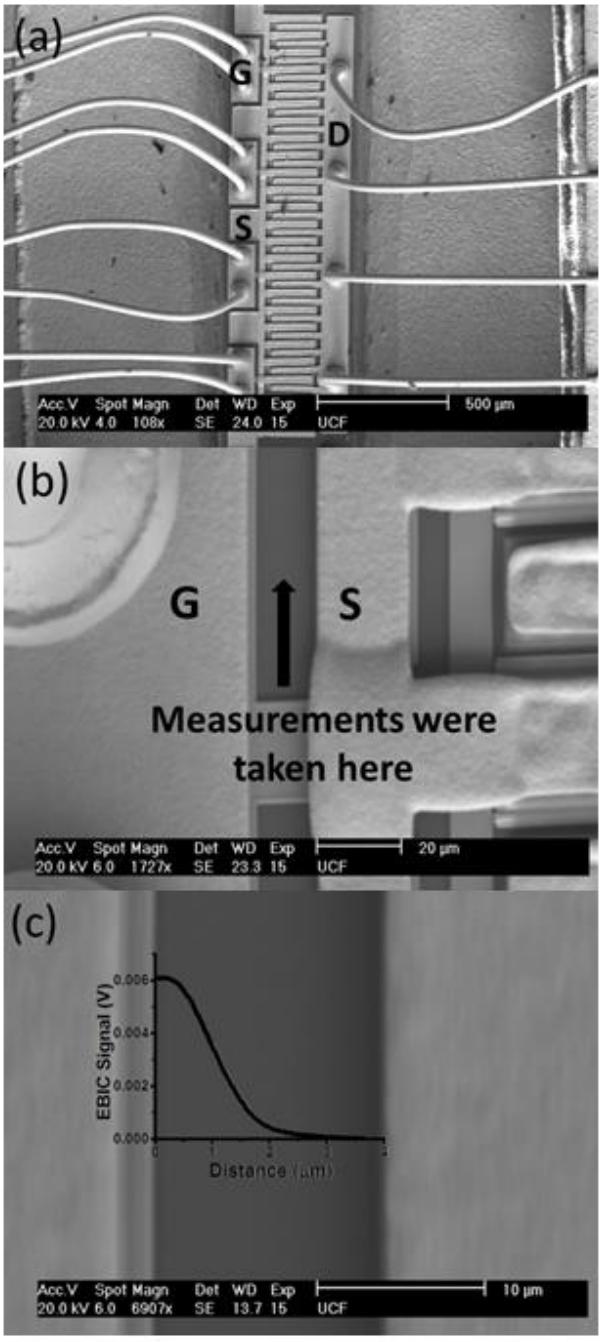

Figure 28. (a) SEM image of AlGaN/GaN HEMT device layout. (b) SEM image indicating location for the EBIC measurements. (c) SEM image with superimposed EBIC signal vs distance.

3.3.2.2 Impact of Gamma-Irradiation on Minority Carrier Transport Properties

A series of variable temperature Electron Beam Induced current measurements were carried out in the vicinity of the HEMTs gate. All experiments were conducted under an accelerating voltage of 20 kV. The temperature-dependent minority carrier diffusion length measurements were also carried out from 25ºC to 125ºC. Line scan of 48 seconds was used for EBIC measurements. For each scan a new location was chosen to refrain from the unintentional influence of the electron beam.

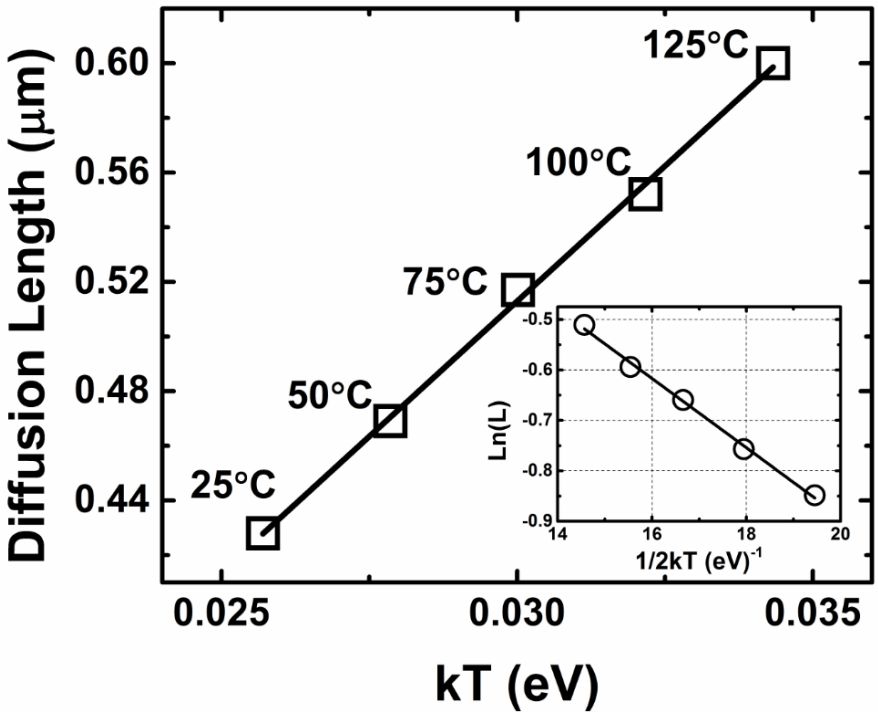

Figure 29. Temperature dependence of L for AlGaN/GaN HEMT subjected to 200 Gy of gamma-irradiation. Inset: Arrhenius plot of the same data yielding the activation energy, ΔE_a, of 68.6 meV. The smaller the activation energy, the more efficient is the thermally activated escape of captured carriers at any fixed temperature.

As the temperature of the sample was raised the diffusion length was shown to be increased. The relationship between diffusion length and the temperature is shown in Figure 29. The value of L increases exponentially with temperature and fitted using equation (10). The activation energy was found from the Arrhenius plot to be 68.6 ± 12 meV. This energy represents the carrier delocalization energy and is related to the increase in the diffusion length due to the reduction in recombination efficiency. This is similar to what we observed for the other AlGaN/GaN HEMTs devices mentioned previously.

EBIC measurements were started prior to gamma-irradiation and then continued on devices subjected to various doses of irradiation. It is apparent from Figure 30 that the diffusion length of minority carriers increases for dose up to ~ 250 Gy with corresponding decrease in the activation energy, 91.2 meV for the standard device to 63.5 meV for the device exposed to 200 Gy. Furthermore, the decay of activation energy with low doses of gamma-irradiation follows a common pattern and observed in other AlGaN/GaN HEMTs as discussed in section 3.3.1. The phenomenon of increase of activation energy with low doses in HEMTs has been attributed to cause of low internal electron injection and subsequent trapping of Compton electrons on neutral levels which are most likely related to nitrogen vacancies. Trapping Compton electrons on V_N - levels prevents recombination of conduction band electrons through these levels. This leads to an increase in the lifetime for non-equilibrium in the band (electrons in the conduction band and holes in the valence band) and as a result an increase in diffusion length.

Starting with the dose of 300 Gy, we observed the deterioration of the HEMTs operation as shown in Figure 31. This trend is similar to what we observed previously and mentioned in earlier section 3.2 and 3.3.1. The possible reason for this damage should be as follows:

(i) Non-equilibrium carrier scattering on radiation induced point defects.

(ii) Decrease of the 2DEG density and mobility due to the creation of trap states throughout the structure.

Reduction in the carrier concentration leads to the increase of the recombination related activation energy in the irradiated devices. This fact has also been observed for proton radiation defects in III-N layers. With the increase of the gamma-irradiation dose the latter factors dominates over increase in the lifetime of Compton electron-induced carrier and hence the increase in the activation energy was observed.

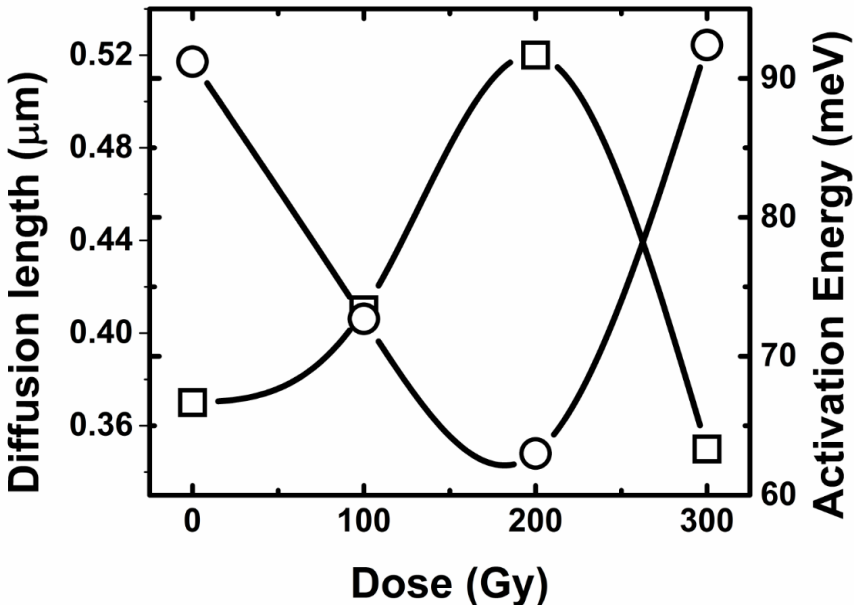

Figure 30. Left axis: Experimental dependence of minority carrier diffusion length (open squares), L, for one of the HEMTs on irradiation dose. Right Axis: Dependence of calculated activation energy (open circles), ΔE_a, on irradiation dose.

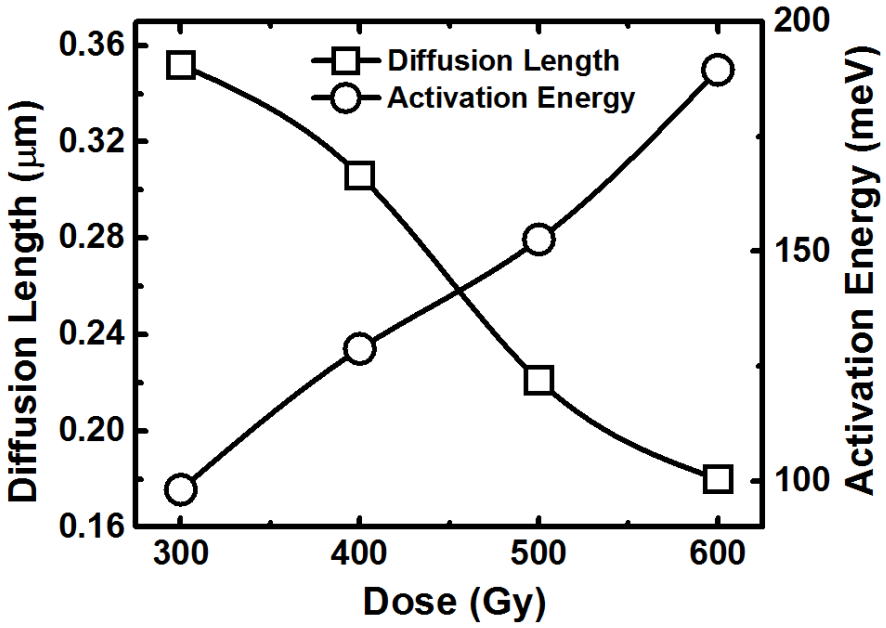

Figure 31. Left Axis: Experimental dependence of the minority carrier diffusion length on irradiation high dose. Right Axis: Dependence of calculated activation energy on higher dose of gamma-irradiation.

3.3.3 Third Low Dose Gamma-Irradiation Experiment

There were seven irradiation series performed on these AlGaN/GaN HEMTs. Devices were exposed to different ^{60}Co gamma-irradiation doses with subsequent exposure from 100 Gy to 1000 Gy. The results from each irradiation series are detailed below with the primary measurements made before and after the irradiation. To understand the gamma-irradiation effect on optical properties of AlGaN/GaN HEMTs, Cathodoluminescence (CL) measurements were performed. Extensive scientific information is obtained by studying the CL spectrum, since its (CL) features depends on the electronic and defect properties of the excited material.

3.3.3.1 Impact of Gamma-Irradiation on Optical Properties

CL measurements were carried out in a Philips XL 30 SEM equipped with Gatan monoCL3 system under a 20 kV accelerating voltage. The temperature dependent measurements were conducted for temperature ranging from 25°C to 125°C in-situ by the external temperature controller and over the wavelength range between 340 and 390 nm. The SEM electron irradiation was carried out in a spot mode to generate the CL spectrum. In all the measurements, CL spectrums were recorded at different locations in order to avoid the unintentional influence of the electron beam. Figure 32 (a) shows the SEM image of the sample and Figure 32 (b) shows where the measurements were taken at six different spots at each temperature.

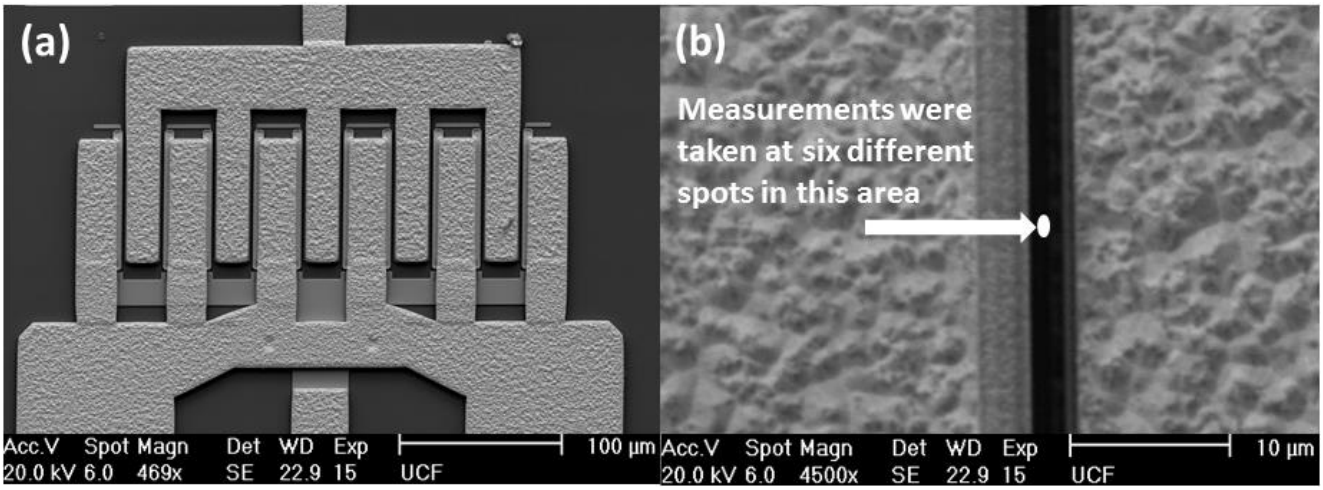

Figure 32. (a) SEM image of AlGaN/GaN device layout. (b) SEM image indicating location of the electron beam spot for CL measurements.

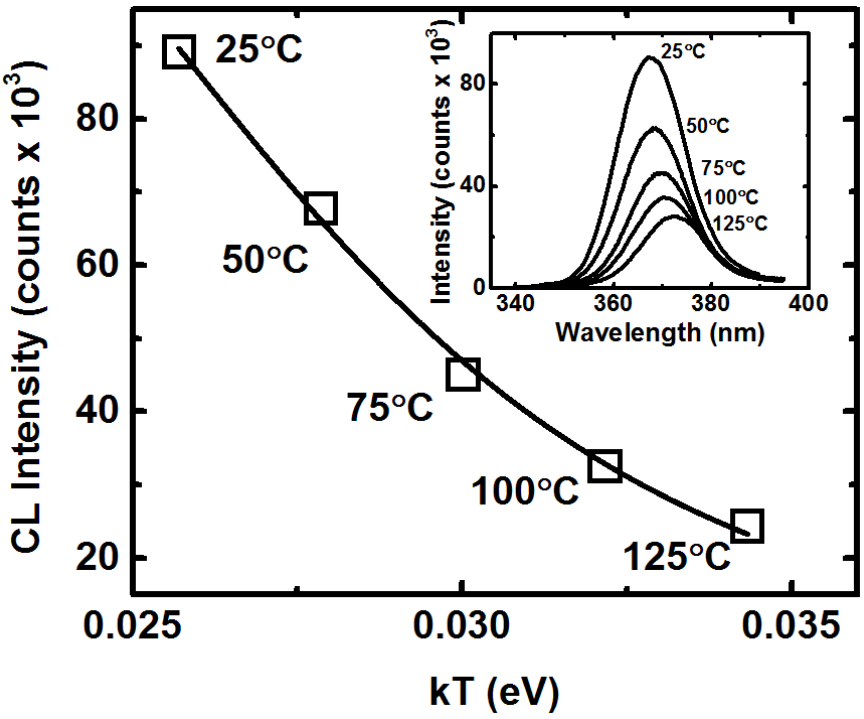

Figure 33. Decay of CL peak intensity with temperature. Inset: CL spectra measurement of AlGaN/GaN reference sample for various temperatures.

Repeating the experiments at higher temperature shows a systematic decay of the CL near band edge intensity (as seen in Figure 33). It is seen that CL intensities approximately follow an exponential decay with increasing temperature, as expected from the equation (12). By fitting the CL intensity and the corresponding temperature intensity to equation 12, we can extract the activation energy of 282 ± 21 meV for the reference device (Figure 33). The activation energy must represent either a barrier to capture a carrier at non-radiative recombination centers, or the thermal activation energy of such centers. The decrease in the frequency of recombination events (CL peak intensity) is because the hole capture cross section is inversely proportional to temperature. CL spectrum also shows characteristic temperature dependence: the emission peak shifts to a higher wavelength (red-shift) as the temperature increases [114-116]. Figure 33 inset shows the small red shift of approximately 47 meV as temperatures increase from 25°C to 125°C. The slight change in the band gap could be due to the expansion or contraction in the interatomic distance.

To understand the gamma-irradiation effect on optical properties of AlGaN/GaN HEMTs, CL measurements were performed on all the devices subjected to subsequent doses of gamma-irradiation. Gamma-irradiation produces native point defects and electrically active defect complexes in the material. For a gamma irradiated material, the concentration of a particular defect depends on the flux of radiation; the threshold energy displacement; the thermal stability of the defect species; pre-existing defects; and the fermi level. The decay of CL peak spectrum caused by the gamma-irradiation is shown in Figure 34. The luminescence spectrum has a maximum around 367.52 nm, which corresponds to energy of ~3.37 eV. The luminescence peak intensity decreased by 12.90 % (after 100 Gy) and 37.23% (after 1000 Gy). Radiation causes the decrease in the CL spectrum intensity by creating localized energy levels in the

material's band gap. These levels act as a non-radiative recombination centers. There are two different mechanisms responsible for the decrease in the CL intensity for low dose (below ~250 Gy) and high dose gamma-irradiation (above ~250 Gy).

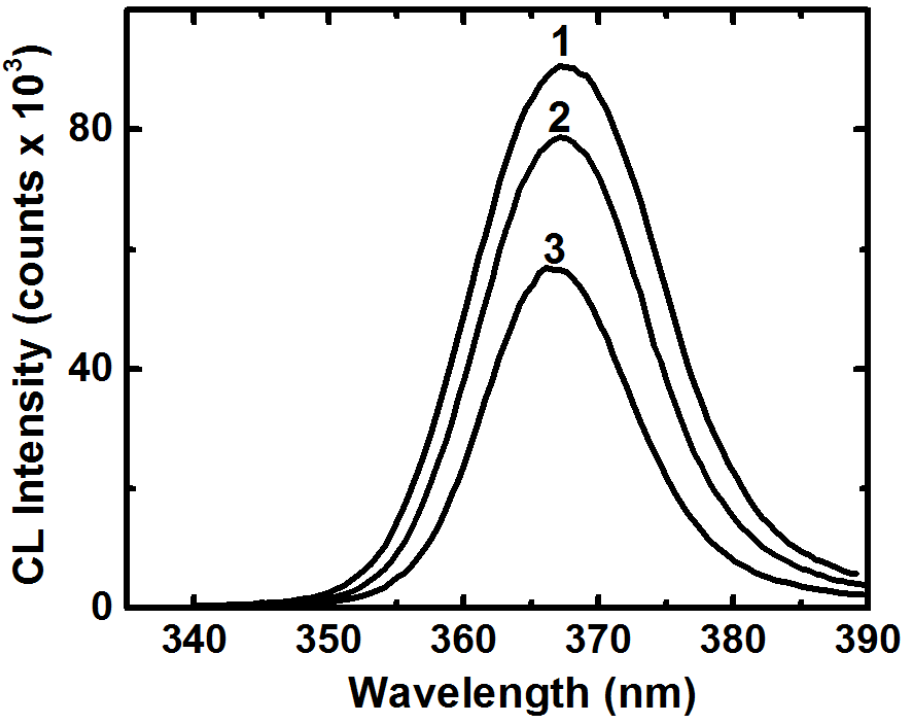

Figure 34. Room temperature CL spectra of AlGaN/GaN devices. Spectrum 1 corresponds to pre-irradiation, Spectrum 2 and 3 corresponds respectively to 100 Gy and 1000 Gy of gamma-irradiation doses.

The decay in the CL intensity below ~250 Gy is due to the Compton Electron Induced effect (Table 10). SEM electron beam generates non-equilibrium electron hole pairs, which recombine either via band to band transition or a transition that involves neutral metastable levels. However, if the non-equilibrium electron gets trapped on defect levels generated by the gamma-irradiation, recombination cannot proceed. The defect levels responsible for this phenomenon are most likely associated with nitrogen vacancies (V_N). Trapping the electrons on

the V_N-levels prevents radiative recombination of the conduction band electrons (generated by the SEM beam) through these levels. As the recombination through a band gap is a dominant process in GaN, trapping a non-equilibrium electron on a meta-stable defect levels in the forbidden gap leads to an increase in the carrier lifetime of electrons in the conduction band and holes in the valence band [38]. Since, the intensity of luminescence is inversely proportional to the non-equilibrium carrier lifetime, the decay in the CL intensity is observed at low doses (below ~ 250 Gy).

Table 10 Room temperature CL peak intensity and activation energy with the dose of the gamma-irradiation.

Dose (Gy)	**CL Peak Intensity (10^3 Counts)**	**Activation Energy (meV)**
Reference	89.2 ± 7.0	282 ± 21
100	78.7 ± 5.6	240 ± 16
200	73.1 ± 6.8	174 ± 15
300	68.6 ± 5.4	263 ± 11
400	60.3 ± 8.2	310 ± 12
500	52.6 ± 7.6	364 ± 8
700	42.8 ± 5.9	392 ± 14
1000	54.8 ± 8.4	380 ± 10

As the dose of gamma-irradiation increases, additional deep traps due to nitrogen vacancies are introduced in AlGaN/GaN devices. The concentration of both isolated native defects such as nitrogen vacancies as well as the complexes involving native defects is expected

to increase after the irradiation. Increasing the gamma-dose continues to decrease the recombination events as more and more electrons are trapped on the defect levels. Increased trapping of carriers and dispersion of charge leads to the decrease in the CL intensity. For higher dose of gamma-irradiation, non-equilibrium carrier scattering on radiation-induced defects dominates over the Compton electron-induced carrier lifetime, and as a result, decrease in the CL intensity is observed.

Temperature dependent CL measurements performed on the devices extracted the activation energy, which (activation energy) decreases for low doses below ~250 Gy and then increases for further higher irradiation as shown in Table 11 and Figure 35. The behavior of the decrease in the activation energy after the low dose gamma-irradiation and the increase for higher doses is similar to the one which is observed through EBIC measurements and reported in section 3.3.2 [109, 117]. The results of CL and EBIC measurements indicate a decrease in the activation energy up to 250 Gy due to the same underlying mechanism of Compton electron-induced increase in non-equilibrium carrier lifetime (Figure 35). Starting with the dose of 300 Gy, the increase in the activation energy is observed. This is consistent with higher density of deep traps induced by larger dose of gamma-irradiation. The increase in the activation energy for high doses may also indicate the creation of large electrically active defect complexes through the addition of new radiation defects to the defects formed at low doses. The difference in the activation energy from optical (CL) and electrical (EBIC) measurements could be due to temperature dependence of carrier diffusivity (L is measured as a function of temperature) or due to different V_N levels (or its complexes) in the material's forbidden gap responsible for capturing the Compton electrons (Figure 30 and Figure 30 inset). Note that carrier diffusivity ($D = \frac{kT}{q}\mu$, where k is Boltzmann constant, T is temperature, μ is mobility and q is elementary

charge) is also a temperature and mobility-dependent quantity which can affect the diffusion length and therefore the calculated activation energy. The defects produced by gamma-irradiation are structure sensitive which could also be the possible reason for the discrepancies between the activation energy.

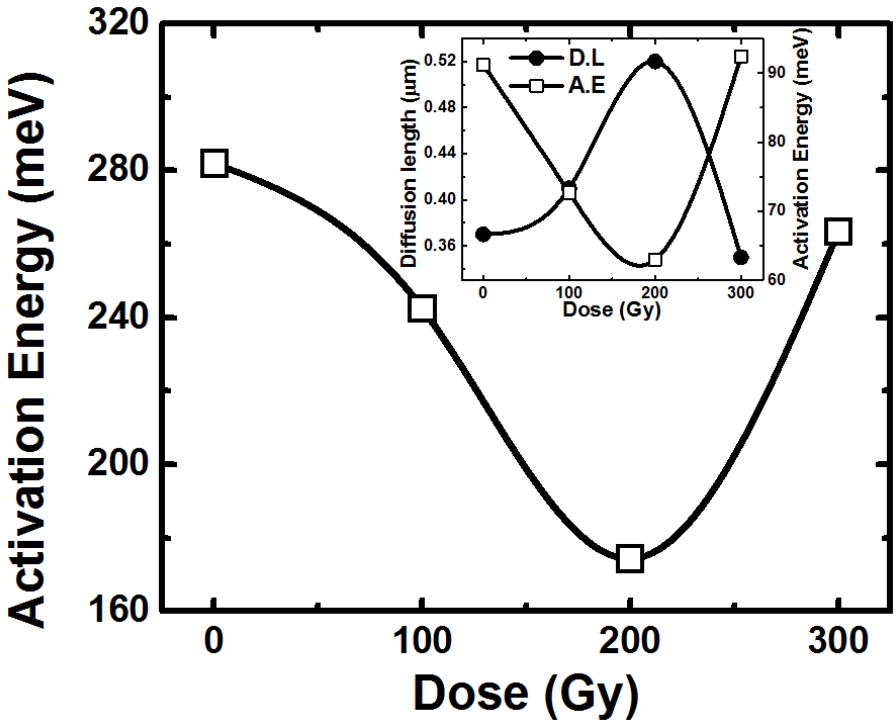

Figure 35. Impact of low dose gamma-irradiation on CL activation energy in AlGaN/GaN HEMTs. Inset: Dependence of experimental diffusion length (closed circles) and associated activation energy (open squares) in AlGaN/GaN HEMTs on irradiation dose from EBIC measurements. Also same as Figure 35 [109].

3.3.4 Fourth Low Dose Gamma-Irradiation Experiment

To enable a direct comparison with the effects observed for low dose (below ~250 Gy) of gamma-irradiation, both EBIC and CL measurements were performed on the same devices. Experiments were conducted on four AlGaN/GaN HEMT devices. Figure 36 (a) shows the Scanning Electron Microscope (SEM) image of the device layout and 36 (b) the position of the CL and EBIC measurements. The AlGaN layer was grown on top of GaN layer by Metal-Organic Vapor Phase Epitaxy (MOVPE) on a sapphire substrate. With the exception of one device (reference device), all other HEMTs were exposed to increasing ^{60}Co gamma-irradiation doses up to 300 Gy; the results were then compared to those from a previous studies of low dose and high dose up to 1000 Gy. The impact of gamma-irradiation on n-channel AlGaN/GaN HEMTs was studied by means of temperature dependent EBIC and CL techniques. As noticed from earlier measurements low (below ~250 Gy) and high doses (above ~ 250 Gy) of gamma-irradiation affects the AlGaN/GaN HEMTs due to different mechanisms. For the dose up to ~ 250 Gy, the improvement of minority carrier diffusion length is likely associated with irradiation induced growing life-time of the non-equilibrium carriers, which is also supported by the decay of the CL intensity. However, with an increased dose of irradiation above ~250 Gy, a decrease in diffusion length was observed which is related to the reduction in the mobility of the charge carriers. The impact of defect scattering is more pronounced at higher irradiation, which leads to mobility degradation. It is shown that calculated activation energy from EBIC and CL measurements are in good agreement with each other, which implies that the same underlying phenomenon is responsible for observed findings.

As both EBIC and CL measurements were performed on the same set of the devices. The correlation between the changes in optical and electric characteristics is revealed; this makes it possible to interpret the mechanism responsible for the radiation effects more reliably.

The following work was originally published in Radiation Effects and Defects in Solids.

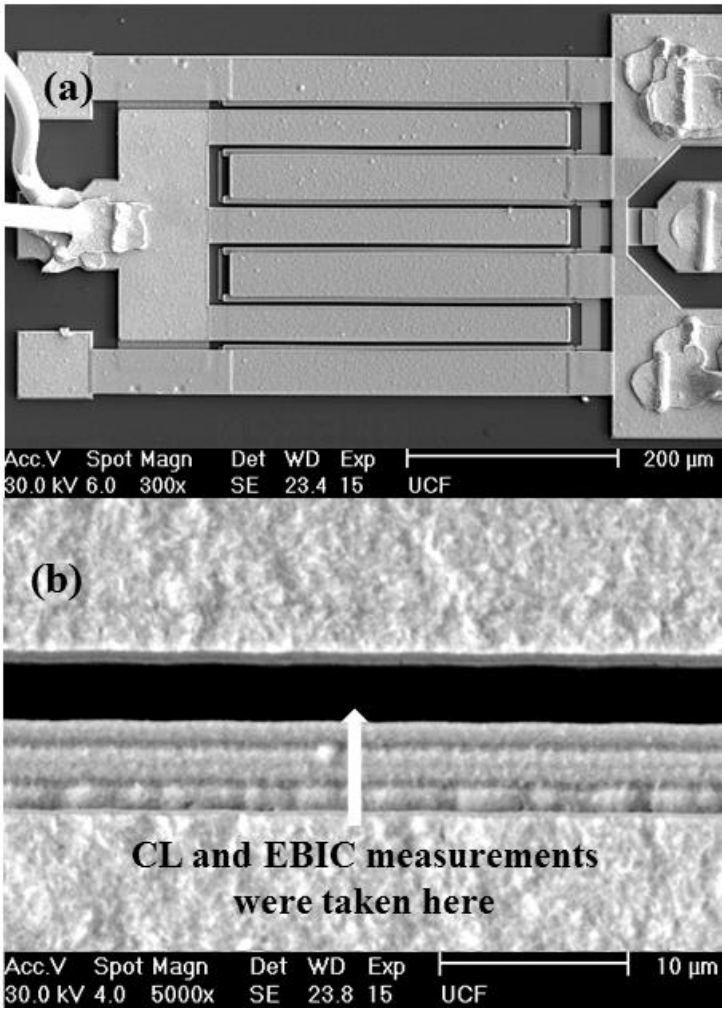

Figure 36. (a) Shows the SEM top view of the AlGaN/GaN HEMTs device layout. (b) SEM image showing the area where Cathodoluminescence and Electron Beam Induced Current measurements were taken.

3.3.4.1 Impact of Gamma-Irradiation on Minority Carrier Transport Properties

The effects of gamma-irradiation on minority carrier transport properties were monitored periodically using the EBIC technique. EBIC measurements were performed in the SEM under a 20 kV electron beam accelerating voltage and for temperature variance of 25^{o}C. For EBIC observation, the variation of the induced current at a Schottky junction is measured in a line scan mode (48 sec) over the specimen area of interest. As beam is moved away from the junction, the current decays, as less minority carriers are able to diffuse to the space-charge region. EBIC measurements were obtained on devices prior to gamma-irradiation and then continued on the same devices subjected to various doses of irradiation.

Temperature dependent EBIC measurements demonstrate the exponential increase of the minority carrier diffusion length as a function of temperature; this is fitted to equation (10). Figure 37 shows the experimental results obtained in this work and Figure 37 inset shows the Arrhenius plot of the same data and obtained activation energy of 188 meV using equation (11).

Figure 38 (a) shows the dependence of the diffusion length (L) and activation energy (ΔE_a) on the dose of the gamma-irradiation as measured by EBIC technique. An increase in minority carrier diffusion length was observed for the low doses of gamma-irradiation (below ~250 Gy). This behavior for low doses of gamma-irradiation can be explained by the phenomenon of internal electron irradiation and subsequent trapping of non-equilibrium electrons on defect levels (26). As discussed in previous section, occupation of the defect levels prevents the recombination of non-equilibrium electron-hole pairs through them which leads to an increase in carrier lifetime of electrons in the conduction band and holes in the valence band.

Minority carrier diffusion length is directly proportional to the lifetime, and thus increases after the irradiation.

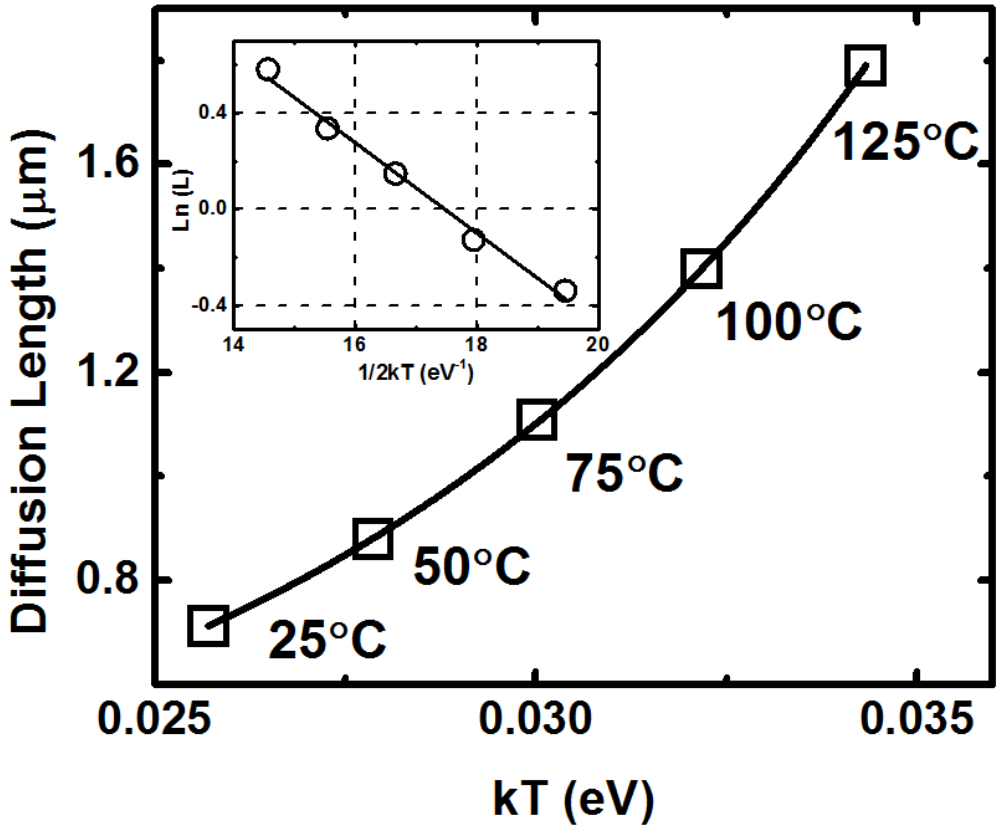

Figure 37. Dependence of diffusion length (L) on temperature in AlGaN/GaN HEMTs. Inset: Arrhenius plot of the same data yielding the activation energy of 188 meV.

However, decrease in the diffusion length for high dose of gamma-irradiation (above ~ 250 Gy) is explained via decrease in the carrier mobility, μ, due to creation of the large number of trap states throughout the structure. The increase in the trap density causes the increased ionized impurity (or defect) scattering of the charge carriers which results in the degradation of the mobility. At higher irradiation, impact of defect scattering is more pronounced which leads to the decrease in mobility. For high dose of gamma-irradiation, non-equilibrium carrier scattering

on radiation induced defects dominates over the irradiation induced increase in the carrier lifetime, and therefore, decrease in diffusion length was observed.

Similar to the diffusion length, the activation energy (calculated using equation (10)) for the pre-irradiated sample decreases for a low dose of irradiation (below ~ 250 Gy). However, for high dose of gamma-irradiation (above ~ 250 Gy), the activation energy were observed to increase. The phenomenon of the initial decrease in the activation energy is attributed to the growing lifetime of non-equilibrium carriers generated by the SEM electron beam. The increase in activation energy (above ~ 250 Gy) indicates the increase in the concentration of native point defects and large electrically active defect complexes. The impact of high dose gamma-irradiation starting from 300 to 1000 Gy on diffusion length and activation energy in AlGaN/GaN HEMTs (Figure 38 b) (11) has already been discussed in section 3.2. The dashed curve is used in Figure 38 (b) in order to emphasize that the obtained results did not consider the information between 0 and 300 Gy. However, these measurements fills the informational gap as far as low dose gamma-irradiation between 0 and 300 Gy is concerned (Figure 38a and 38b). Compton trapping of the electron on the point defects results in an increase in diffusion length and decrease in activation energy until the dose of 300 Gy. The results from this research and previous research are in agreement that starting from 300 Gy dose of gamma-irradiation AlGaN/GaN HEMTs causes the degradation in minority carrier properties of the devices.

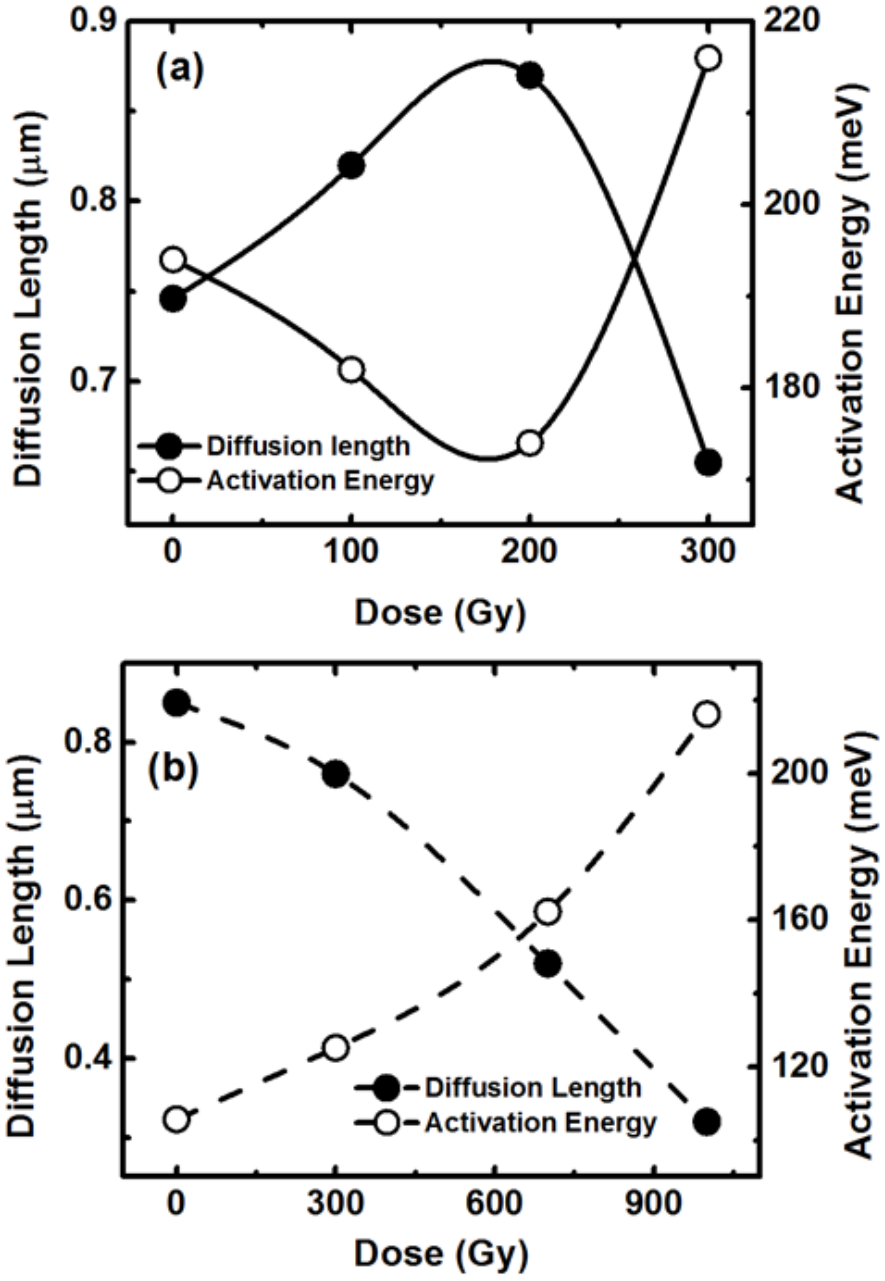

Figure 38. (a) Impact of low dose gamma-irradiation on diffusion length and associated activation energy in AlGaN/GaN HEMTs. Diffusion length and activation energy was extracted from EBIC measurements. (b) Dependence of diffusion length and activation energy on higher dose of gamma-irradiation. After Reference [107].

3.3.4.2 Impact of Gamma-Irradiation on Optical Properties

To understand the gamma-irradiation effect on optical properties of AlGaN/GaN HEMTs, temperature dependent Cathodoluminescence (CL) measurements were performed. The temperature of the sample was varied from 25° C to 125° C in-situ by specially designed hot stage and the external temperature controller. CL peak intensity decreases with increasing temperature as shown in Figure 39. The 20 kV SEM electron irradiation was carried out in a spot mode to generate the CL spectrum. In all the measurements, CL spectrums were recorded at different locations in order to avoid the unintentional influence of the electron beam.

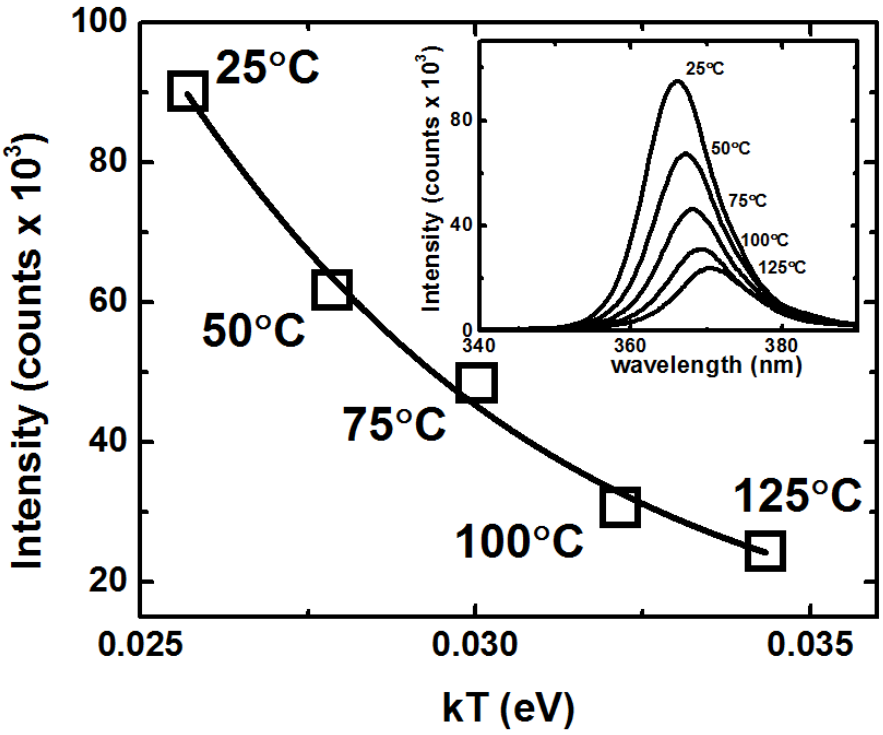

Figure 39. Temperature dependence of Cathodoluminescence peak intensity in AlGaN/GaN HEMTs and the fit using equation (12). Inset: Cathodoluminescence spectra measurements taken at different temperatures.

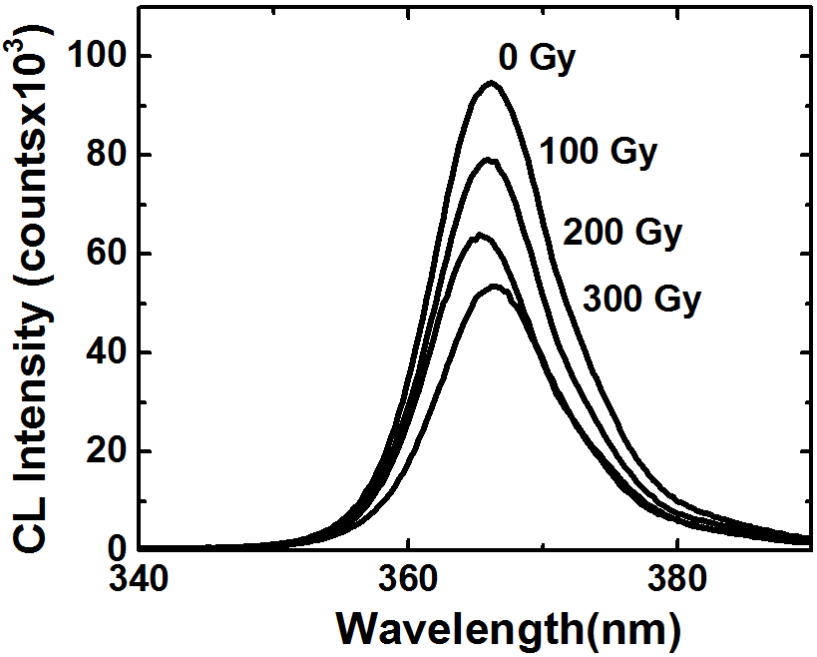

Figure 40. Decay of room temperature Cathodoluminescence intensity in AlGaN/GaN HEMTs with increasing dose of gamma-irradiation. The spectra were taken at 0, 100, 200 and 300 Gy dose of gamma-irradiation.

Figure 40 shows the room temperature CL spectra of AlGaN/GaN HEMTs irradiated with 100, 200 and 300 Gy dose of gamma-irradiation. The observed decrease in the CL peak intensity after the gamma-irradiation provides the direct evidence of the decrease in the number of recombination events. Gamma-irradiation causes the decrease in the CL intensity by introducing defect levels, in the material's band gap, which are involved in the corresponding recombination process. Trapping the Compton electron on these shallow nitrogen vacancy levels prevents radiative recombination of the conduction band electrons through these levels and hence increases the minority carrier lifetme. Since luminescence intensity is inversely proportional to lifetime τ, systematic decay of the intensity was observed after the irradiation. The increase in L

after low dose of gamma-irradiation (below ~ 250 Gy) is consistent with the decrease in the CL intensity (Figure 38a and 40). The results of the EBIC measurements are correlated with the CL measurements in order to demonstrate that same underlying process is responsible for change in diffusion length and CL intensity after gamma-irradiation. This observation also helps to understand the difference in effects induced by the low dose (below ~250 Gy) and high dose (above ~ 250 Gy) of gamma-irradiation.

For gamma-irradiation dose above ~250 Gy, different phenomenon is responsible for the decrease in the CL intensity and decrease in the diffusion length. The concentrations of nitrogen vacancies related defects as well as the complexes involving native defects are expected to increase after irradiation. For the CL intensity, recombination events continue to decrease with increase of gamma-irradiation as more and more electrons are trapped on the defect levels. However, decrease in the diffusion length is explained via decrease in the carrier mobility, μ, due to creation of the large number of trap states throughout the structure.

Another interesting observation shows that the activation energy (calculated using equation (10 and 12)) for the pre-irradiated sample decreases for a low dose of irradiation (below ~200 Gy). However, for high dose of gamma-irradiation (above ~ 250 Gy), the activation energy were observed to increase. It is quite convincing that activation from the EBIC measurements (Figure 38 a) shows exactly the same trend as that of the activation energy from the CL measurements (Figure 41). The phenomenon of the initial decrease in the activation energy is attributed to the growing lifetime of non-equilibrium carriers generated by the SEM electron beam. The increase in activation energy (above ~250 Gy) indicates the increase in the concentration of native point defects and large electrically active defect complexes.

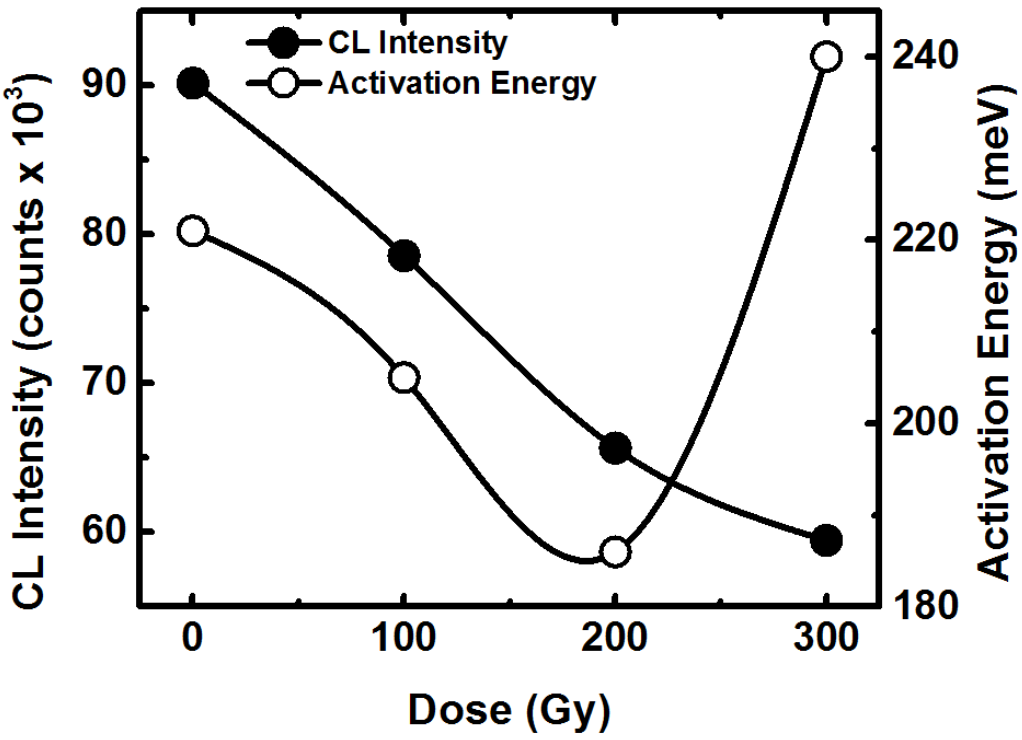

Figure 41. Dependence of Cathodoluminescence peak intensity and activation energy in AlGaN/GaN HEMTs on gamma-irradiation dose. Activation energy is obtained from the Cathodoluminescence measurements using equation (12).

CHAPTER FOUR: SUMMARY AND CONCLUSIONS

This thesis covers the several aspects of impact of gamma-irradiation on minority carrier and optical properties of AlGaN/GaN HEMTs. It started with high dose of gamma-irradiation (above ~250 Gy), where EBIC measurements were performed on different doses of gamma-irradiation up to 1000 Gy. Temperature dependent EBIC measurements allowed acquiring values for the activation energy as a function of dose for AlGaN/GaN devices. I-V measurements were also conducted in parallel to assess the impact of gamma-irradiation on transfer, gate and drain characteristics. EBIC measurements yielded a decrease in diffusion length an increase in activation energy with dose of gamma-irradiation. These measurements gave insight into the correlation between the gamma-irradiation dose and the creation of deeper level traps. Measurements also correlate the device degradation with deterioration of the transport characteristics. Gamma-irradiation induces nitrogen vacancy defects in the AlGaN/GaN material. These vacancies related deep traps acts as a scattering center, which reduce the carrier concertation and increase the recombination related activation energy, which exhibits more and more degradation with gamma-irradiation dose. These traps also results in the degradation of the device I-V characteristics after the irradiation.

From gamma-irradiation, the experiments proceeded to the annealing of the gamma-irradiated devices. All gamma-irradiated devices were annealed at 200°C for 25 minutes. Annealing experiments were performed with the goal of improving device performance and minority carrier transport after gamma-irradiation. Experiments on annealing showed that in addition to fundamental properties (diffusion length and associated activation energy), partial recovery (depending on the dose) in device performance is possible at this temperature.

High dose gamma-irradiation didn't consider the information between 0 and 300 Gy. To understand the effects of low doses (below ~250 Gy) of gamma-irradiation on AlGaN/GaN HEMTs, EBIC and CL measurements were performed on four sets of different devices. The EBIC measurements were started prior to gamma-irradiation and then continued after device exposure to several low doses of gamma-rays. In contrast to the behavior observed for high doses one can see that diffusion length of minority carrier exhibits an initial increase for the dose up to 200 Gy before it starts decreasing. This behavior for the low doses is explained by the phenomenon of internal electron injection and subsequent trapping of Compton electrons on neutral levels, most likely related to nitrogen vacancies. Compton electron trapping on this defect related levels prohibits the recombination via these levels and leads to an increase of non-equilibrium minority carrier (hole) life-time and consequently diffusion length. Similar behavior is observed for the activation energy, which shows a decrease till 200 Gy and then increase after the further irradiation.

To complement EBIC measurements, CL measurements were carried out in the vicinity of the gate at variable temperatures. CL probing also identify the possible levels (defects) generated as a result of gamma-bombardment. A decrease in the CL intensity was observed after the gamma-irradiation. Decrease in the intensity can be explained via trapping of Compton electron on gamma-induced deep levels which prevents the radiative recombination through these levels. Since the intensity of the luminescence is proportional to the rate of radiative recombination, which decreases with increasing lifetime, and therefore the CL decay was observed. Activation energy from both EBIC and CL measurements follow exactly the same trend of initial decrease for low doses (below ~200 Gy) and increase for higher doses (above ~250 Gy). Comparing the activation energy before and after the gamma-irradiation identified

the defect levels and their dependence on the dose of irradiation. Low dose of gamma-irradiation separate the impact of Compton electron effect and that of energetic gamma-irradiation extended and point defects.

In conclusion, low dose of gamma-irradiation demonstrates the potential for considerable performance improvement of AlGaN/GaN HEMTs. It was shown that low dose (below ~250 Gy) and high dose (above ~ 250 Gy) of gamma-irradiation play different mechanism in AlGaN/GaN HEMTs respectively. For low dose of gamma-irradiation, the improvement in minority carrier diffusion length is likely associated with the irradiation induced growing lifetime of the non-equilibrium carriers, which is supported by the decay of the CL intensity. However with the increased dose of irradiation (above ~250 Gy), decrease in the diffusion length was observed which is related to the decrease in the mobility of the charge carriers. The impact of defect scattering is more pronounced at higher irradiation which leads to the degradation of the mobility. Activation energy obtained from both experimental techniques was in good agreement with each other, which suggests the obtained results follow the same phenomenon. This finding has significant importance in wide band gap technology, since the investigation gives the important information about defects in semiconductor heterostructures, especially if additional traps are introduced under external irradiation. Understanding the radiation effects in AlGaN/GaN devices, with various doses of gamma-photons have on carrier transport, recombination and creation of traps play a significant role in determining device performance and reliability, especially for the space borne applications. This information may lead to future development of devices capable of withstanding bombardment by high-energy particles.

APPENDIX: PUBLICATIONS

A.1 Journal Publications

1. Anupama Yadav, Cameron Glasscock, Elena Flitsiyan, Leonid Chernyak, Igor Lubomirsky, Sergey Khodorov, Joseph Salzman, Carlo Coppola, Sebestian Guay and Jasques Boivin, "*Optical and Electron Beam Studies of Gamma-Irradiated AlGaN/GaN High Electron Mobility Transistors*" In-Print for publication in Radiation Effects and Defects in Solids, Manuscript Id: 0023.R1 (2016).

2. Anupama Yadav, Elena Flitsiyan, Leonid Chernyak, Ya-Hsi Hwang, Yueh-Ling Hsieh, Lei Lei, Fan Ren, Stephen J. Pearton, and Igor Lubomirsky, "*Low and moderate dose gamma-irradiation and annealing impact on electronic and electrical properties of AlGaN/GaN high electron mobility transistors"* Radiation Effects and Defects in Solids **170**, 2 (2015).

3. Ya-Hsi Hwang, Yueh-Ling Hsieh, Lei Lei, Shun Li, Fan Ren, Stephen J. Pearton, Anupama Yadav, Casey Schwarz, Max Shatkhin, Luther Wang, Elena Flitsiyan, Leonid Chernyak, Albert G. Baca, Andrew A. Allerman, Carlos A. Sanchez, I. I. Kravchenko, "*Effect of low dose gamma-irradiation on DC performance of circular AlGaN/GaN high electron mobility transistors*" Journal of Vacuum Science and Technology B **32**, 3, 031203 (2014).

4. Casey Schwarz, Anupama Yadav, Max Shatkhin, Elena Flitsiyan, Leonid Chernyak, Vladimir Kasiyan, Lu Liu, Yu Yin Xi, Fan Ren, Stephen J. Pearton, Chien Fong Lo, J.W. Johnson, "*Gamma irradiation impact on electronic carrier transport in AlGaN/GaN high electron mobility transistors*" Applied Physics Letters **102**, 6, 062102 (2013).

A.2 Conference Proceedings

1. Anupama Yadav, Michael Antia, Elena Flitsiyan, Leonid Chernyak, Igor Lubomirsky and Joseph Salzman, "*Cathodoluminescence Studies of Gamma-Irradiation Effects on AlGaN/GaN High Electron Mobility Transistors (HEMTs)"* Electrochemical Society Transactions **69**, 14, 137 (2015).

2. Anupama Yadav, Elena Flitsiyan, Leonid Chernyak, Ya-Hsi Hwang, Yueh-Ling Hsieh, Lei Lei, Fan Ren, Stephen J. Pearton, and Igor Lubomirsky, "*Impact of low dose gamma-irradiation on electronic carrier transport in AlGaN/GaN high electron mobility transistors"* Material Research Society Proceedings **1792** (2015).

3. Anupama Yadav, Casey Schwarz, Max Shatkhin, Luther Wang, Elena Flitsiyan, Leonid Chernyak, Lu Liu, Ya-Hsi Hwang, Fan Ren, Stephen J. Pearton and Igor Lubomirsky, " *Effect of annealing on electronic carrier transport properties of gamma-irradiated AlGaN/GaN high electron mobility transistors*" Electrochemical Society Transactions **61**, 4, 171 (2014).

4. Ya-Hsi Hwang, Yueh-Ling Hsieh, Lei Lei, Shun Li, Fan Ren, Stephen J. Pearton, Anupama Yadav, Casey Schwarz, Max Shatkhin, Luther Wang, Elena Flitsiyan, Leonid Chernyak, Albert G. Baca, Andrew A. Allerman, Carlos A. Sanchez, I. I. Kravchenko, "*Effect of gamma-irradiation on DC performance of circular-shaped AlGaN/GaN high electron mobility transistors*" ECS Transactions **61**, 4, 205 (2014).

LIST OF REFERENCES

1. L'vov, B.V., *Kinetics and mechanism of thermal decomposition of GaN.* Thermochimica acta, 2000. **360**(1): p. 85-91.
2. Van Vechten, J., *Quantum dielectric theory of electronegativity in covalent systems. III. Pressure-temperature phase diagrams, heats of mixing, and distribution coefficients.* Physical Review B, 1973. **7**(4): p. 1479.
3. Yonenaga, I., *Thermo-mechanical stability of wide-bandgap semiconductors: high temperature hardness of SiC, AlN, GaN, ZnO and ZnSe.* Physica B: Condensed Matter, 2001. **308**: p. 1150-1152.
4. Fuchs, M., et al., *Cohesive properties of group-III nitrides: A comparative study of all-electron and pseudopotential calculations using the generalized gradient approximation.* Physical Review B, 2002. **65**(24): p. 245212.
5. Nord, J., et al., *Modelling of compound semiconductors: analytical bond-order potential for gallium, nitrogen and gallium nitride.* Journal of Physics: Condensed Matter, 2003. **15**(32): p. 5649.
6. Look, D.C., et al., *Defect donor and acceptor in GaN.* Physical Review Letters, 1997. **79**(12): p. 2273.
7. Ionascut-Nedelcescu, A., et al., *Radiation hardness of gallium nitride.* Nuclear Science, IEEE Transactions on, 2002. **49**(6): p. 2733-2738.
8. Klein, C.A., *Bandgap dependence and related features of radiation ionization energies in semiconductors.* Journal of Applied Physics, 1968. **39**(4): p. 2029-2038.
9. Mishra, U.K., et al., *GaN microwave electronics.* Microwave Theory and Techniques, IEEE Transactions on, 1998. **46**(6): p. 756-761.

10. Wu, Y.-F., et al., *Very-high power density AlGaN/GaN HEMTs.* Electron Devices, IEEE Transactions on, 2001. **48**(3): p. 586-590.

11. Cai, S., et al., *Annealing behavior of a proton irradiated Al x Ga 1-x N/GaN high electron mobility transistor grown by MBE.* Electron Devices, IEEE Transactions on, 2000. **47**(2): p. 304-307.

12. Gaudreau, F., et al., *Transport properties of proton-irradiated gallium nitride-based two-dimensional electron-gas system.* Nuclear Science, IEEE Transactions on, 2002. **49**(6): p. 2702-2707.

13. Luo, B., et al., *Effect of High-Energy Proton Irradiation on DC Characteristics and Current Collapse in MgO and Sc2 O 3 Passivated AlGaN/GaN HEMTs.* Electrochemical and solid-state letters, 2003. **6**(3): p. G31-G33.

14. White, B., et al., *Electrical, spectral, and chemical properties of 1.8 MeV proton irradiated AlGaN/GaN HEMT structures as a function of proton fluence.* IEEE Transactions on Nuclear Science, 2003. **50**(6): p. 1934-1941.

15. Hu, X., et al., *Proton-irradiation effects on AlGaN/AlN/GaN high electron mobility transistors.* Nuclear Science, IEEE Transactions on, 2003. **50**(6): p. 1791-1796.

16. Hu, X., et al., *The energy dependence of proton-induced degradation in AlGaN/GaN high electron mobility transistors.* Nuclear Science, IEEE Transactions on, 2004. **51**(2): p. 293-297.

17. Karmarkar, A.P., et al., *Proton irradiation effects on GaN-based high electron-mobility transistors with Si-doped Al x Ga 1-x N and thick GaN cap Layers.* Nuclear Science, IEEE Transactions on, 2004. **51**(6): p. 3801-3806.

18. Vitusevich, S., et al., *Effects of γ-irradiation on AlGaN/GaN-based HEMTs.* physica status solidi (a), 2003. **195**(1): p. 101-105.

19. Kelly, J.G., et al., *Dose Enhancement Effects in MOSFET IC's Exposed in Typical 60Co Facilities.* Nuclear Science, IEEE Transactions on, 1983. **30**(6): p. 4388-4393.

20. Huang, T.-y., et al., *Improving radiation hardness of EEPROM/flash cell by N 2 O annealing.* Electron Device Letters, IEEE, 1998. **19**(7): p. 256-258.

21. Prutchi, D., J.L. Prince, and L.J. Stotts, *X-and gamma-ray hardness of floating-gate EEPROM technology as applied to implantable medical devices.* Components and Packaging Technologies, IEEE Transactions on, 1999. **22**(3): p. 390-398.

22. Oiler, J., et al. *Film Bulk Acoustic-Wave Resonator based radiation sensor*. in *Nano/Micro Engineered and Molecular Systems (NEMS), 2010 5th IEEE International Conference on*. 2010. IEEE.

23. Luo, B., et al., *Influence of 60Co γ-rays on dc performance of AlGaN/GaN high electron mobility transistors.* Applied physics letters, 2002. **80**(4): p. 604-606.

24. Polyakov, A., et al., *Electron irradiation of AlGaN/ GaN and AlN/ GaN heterojunctions.* Applied Physics Letters, 2008. **93**(15): p. 152101.

25. Khanna, R., et al., *Effects of high dose proton irradiation on the electrical performance of ZnO Schottky diodes.* physica status solidi (a), 2004. **201**(12): p. R79-R82.

26. Lo, C., et al., *Effects of proton irradiation on dc characteristics of InAlN/GaN high electron mobility transistors.* Journal of Vacuum Science & Technology B, 2011. **29**(6): p. 061201.

27. Luo, B., et al., *DC and RF performance of proton-irradiated AlGaN/GaN high electron mobility transistors.* Applied Physics Letters, 2001. **79**(14): p. 2196-2198.

28. Luo, B., et al., *High-energy proton irradiation effects on AlGaN/GaN high-electron mobility transistors.* Journal of electronic materials, 2002. **31**(5): p. 437-441.

29. Luo, B., et al., *Proton and gamma-ray irradiation effects on InGaP/GaAs heterojunction bipolar transistors.* Journal of The Electrochemical Society, 2002. **149**(4): p. G213-G217.

30. Sonia, G., et al., *High energy irradiation effects on AlGaN/GaN HFET devices.* Semiconductor Science and Technology, 2007. **22**(11): p. 1220.

31. Ling, L., et al., *Neutron irradiation effects on AlGaN/GaN high electron mobility transistors.* Chinese Physics B, 2012. **21**(3): p. 037104.

32. Lv, L., et al., *Study of proton irradiation effects on AlGaN/GaN high electron mobility transistors.* Microelectronics Reliability, 2011. **51**(12): p. 2168-2172.

33. Vitusevich, S., et al., *Low-Frequency Noise in AlGaN/GaN High Electron Mobility Transistors Irradiated by γ-Ray Quanta.* physica status solidi (c), 2003(1): p. 78-81.

34. Aktas, O., et al., *60 Co gamma radiation effects on DC, RF, and pulsed I–V characteristics of AlGaN/GaN HEMTs.* Solid-State Electronics, 2004. **48**(3): p. 471-475.

35. Emtsev, V., et al., *Point defects in gamma-irradiated n-GaN.* Semiconductor science and technology, 2000. **15**(1): p. 73.

36. CHERNYAK, L., et al. *Studies of electron trapping in III-nitrides.* in *Proceedings-Electrochemical Society*. 2004. Electrochemical Society.

37. Lopatiuk, O., et al., *Studies of electron trapping in GaN doped with carbon.* Thin solid films, 2007. **515**(10): p. 4365-4368.

38. Chernyak, L., et al., *Cathodoluminescence studies of the electron injection-induced effects in GaN.* Applied physics letters, 2003. **82**(21): p. 3680-3682.

39. Lawaetz, P., *Stability of the wurtzite structure.* Physical Review B, 1972. **5**(10): p. 4039.

40. Yeh, C.-Y., et al., *Zinc-blende–wurtzite polytypism in semiconductors.* Physical Review B, 1992. **46**(16): p. 10086.

41. Christensen, N. and I. Gorczyca, *Optical and structural properties of III-V nitrides under pressure.* Physical Review B, 1994. **50**(7): p. 4397.

42. Ambacher, O., *Growth and applications of group III-nitrides.* Journal of Physics D: Applied Physics, 1998. **31**(20): p. 2653.

43. Xia, H., Q. Xia, and A.L. Ruoff, *High-Pressure Structure of Gallium Nitride - Wurtzite-to-Rock-Salt Phase-Transition.* Physical Review B, 1993. **47**(19): p. 12925-12928.

44. Vogel, D., P. Krüger, and J. Pollmann, *Structural and electronic properties of group-III nitrides.* Physical Review B, 1997. **55**(19): p. 12836.

45. Vurgaftman, I. and J. Meyer, *Band parameters for nitrogen-containing semiconductors.* Journal of Applied Physics, 2003. **94**(6): p. 3675-3696.

46. Ambacher, O., et al., *Two-dimensional electron gases induced by spontaneous and piezoelectric polarization charges in N-and Ga-face AlGaN/GaN heterostructures.* Journal of Applied Physics, 1999. **85**(6): p. 3222.

47. Ponce, F., et al., *Determination of lattice polarity for growth of GaN bulk single crystals and epitaxial layers.* Applied physics letters, 1996. **69**(3): p. 337-339.

48. Daudin, B., J. Rouviere, and M. Arlery, *Polarity determination of GaN films by ion channeling and convergent beam electron diffraction.* Applied physics letters, 1996. **69**(17): p. 2480-2482.

49. Kowalski, B., et al., *Surface states on GaN (000$\bar{1}$)(1 × 1)—an angle-resolved photoemission study.* Surface science, 2002. **507**: p. 186-191.

50. Huang, D., et al., *Dependence of GaN polarity on the parameters of the buffer layer grown by molecular beam epitaxy.* Applied Physics Letters, 2001. **78**(26): p. 4145-4147.

51. Sumiya, M. and S. Fuke, *Review of polarity determination and control of GaN.* MRS Internet Journal of Nitride Semiconductor Research, 2004. **9**: p. e1.

52. Losurdo, M., et al., *Interplay between GaN polarity and surface reactivity towards atomic hydrogen.* Journal of applied physics, 2004. **95**(12): p. 8408-8418.

53. Han, P., et al., *Polarity dependence of hexagonal GaN films on two opposite c faces of Al2O3 substrate.* 2001.

54. Okumura, H., et al., *Polarity control in MBE growth of III-nitrides, and its device application.* Current Applied Physics, 2002. **2**(4): p. 305-310.

55. Dovidenko, K., et al. *Comparative Study of Typical Defects in III-Nitride Thin Films and Their Alloys*. in *MRS Proceedings*. 1997. Cambridge Univ Press.

56. Nakamura, S., *GaN growth using GaN buffer layer.* Japanese Journal of Applied Physics, 1991. **30**(10A): p. L1705.

57. Uchida, K., et al., *Nitridation process of sapphire substrate surface and its effect on the growth of GaN.* Journal of applied physics, 1996. **79**(7): p. 3487-3491.

58. Posternak, M., et al., *Ab initio study of the spontaneous polarization of pyroelectric BeO.* Physical review letters, 1990. **64**(15): p. 1777.

59. Bernardini, F., V. Fiorentini, and D. Vanderbilt, *Spontaneous polarization and piezoelectric constants of III-V nitrides.* Physical Review B, 1997. **56**(16): p. R10024.

60. Strite, S. and H. Morkoç, *GaN, AlN, and InN: a review.* Journal of Vacuum Science & Technology B, 1992. **10**(4): p. 1237-1266.

61. Lähnemann, J., et al., *Direct experimental determination of the spontaneous polarization of GaN.* Physical Review B, 2012. **86**(8): p. 081302.

62. Ambacher, O., et al., *Two dimensional electron gases induced by spontaneous and piezoelectric polarization in undoped and doped AlGaN/GaN heterostructures.* Journal of applied physics, 2000. **87**(1): p. 334-344.

63. Resta, R., *Macroscopic polarization in crystalline dielectrics: the geometric phase approach.* Reviews of modern physics, 1994. **66**(3): p. 899.

64. Ibbetson, J., et al., *Polarization effects, surface states, and the source of electrons in AlGaN/GaN heterostructure field effect transistors.* Applied Physics Letters, 2000. **77**(2): p. 250-252.

65. Ambacher, O., et al., *Pyroelectric properties of Al (In) GaN/GaN hetero-and quantum well structures.* Journal of physics: condensed matter, 2002. **14**(13): p. 3399.

66. Bernardini, F., V. Fiorentini, and D. Vanderbilt, *Accurate calculation of polarization-related quantities in semiconductors.* Physical Review B, 2001. **63**(19): p. 193201.

67. Trew, R., M. Shin, and V. Gatto, *High power applications for GaN-based devices.* Solid-State Electronics, 1997. **41**(10): p. 1561-1567.

68. Quay, R., et al., *A temperature dependent model for the saturation velocity in semiconductor materials.* Materials Science in Semiconductor Processing, 2000. **3**(1): p. 149-155.

69. Anwar, A., S. Wu, and R.T. Webster, *Temperature dependent transport properties in GaN, Al x Ga 1-x N, and In x Ga 1-x N semiconductors.* Electron Devices, IEEE Transactions on, 2001. **48**(3): p. 567-572.

70. Kranti, A., S. Haldar, and R. Gupta, *An accurate charge control model for spontaneous and piezoelectric polarization dependent two-dimensional electron gas sheet charge density of lattice-mismatched AlGaN/GaN HEMTs.* Solid-State Electronics, 2002. **46**(5): p. 621-630.

71. Smorchkova, I., et al., *Polarization-induced charge and electron mobility in AlGaN/GaN heterostructures grown by plasma-assisted molecular-beam epitaxy.* Journal of Applied Physics, 1999. **86**(8): p. 4520-4526.

72. Shen, L., et al., *AlGaN/AlN/GaN high-power microwave HEMT.* Electron Device Letters, IEEE, 2001. **22**(10): p. 457-459.

73. Zhang, Y. and J. Singh, *Charge control and mobility studies for an AlGaN/GaN high electron mobility transistor.* Journal of Applied Physics, 1999. **85**(1): p. 587-594.

74. Firoz, S. and R. Chauhan, *COMPARISION OF AlGaN/GaN AND AlGaAs/GaAs BASED HEMT DEVICE UNDER DOPING CONSIDERATION.* International Journal of Advances in Engineering & Technology, 2011. **1**(2): p. 12-19.

75. Kucheyev, S.O., et al., *Effect of irradiation temperature and ion flux on electrical isolation of GaN.* Journal of applied physics, 2002. **91**(7): p. 4117-4120.

76. Johannesen, P., et al., *Intrinsic defects in GaN. II. Electronically enhanced migration of interstitial Ga observed by optical detection of electron paramagnetic resonance.* Physical Review B, 2004. **69**(4): p. 045208.

77. Jenkins, D.W., J.D. Dow, and M.H. Tsai, *N vacancies in AlxGa1− xN.* Journal of applied physics, 1992. **72**(9): p. 4130-4133.

78. Tansley, T. and R. Egan, *Point-defect energies in the nitrides of aluminum, gallium, and indium.* Physical Review B, 1992. **45**(19): p. 10942.

79. Look, D.C., et al., *On the nitrogen vacancy in GaN.* Applied physics letters, 2003. **83**(17): p. 3525-3527.

80. Neugebauer, J. and C.G. Van de Walle, *Atomic geometry and electronic structure of native defects in GaN.* Physical Review B, 1994. **50**(11): p. 8067.

81. Bogusl, P., E. Briggs, and J. Bernholc, *Native defects in gallium nitride.* Physical Review B, 1995. **51**(23): p. 17255.

82. Polyakov, A., et al., *Electron Irradiation Effects in GaN/ InGaN Multiple Quantum Well Structures.* Journal of The Electrochemical Society, 2008. **155**(1): p. H31-H35.

83. Saarinen, K., et al., *Ga vacancies in electron irradiated GaN: introduction, stability and temperature dependence of positron trapping.* Physica B: Condensed Matter, 2001. **308**: p. 77-80.

84. Fang, Z.-Q., et al., *Effects of electron-irradiation on electrical properties of AlGaN/GaN Schottky barrier diodes.* Journal of Applied Physics, 2009. **105**(12): p. 123704.

85. Umana-Membreno, G., et al., *60Co gamma-irradiation-induced defects in n-GaN.* Applied physics letters, 2002. **80**(23): p. 4354-4356.

86. Polyakov, A., et al., *Effects of proton implantation on electrical and recombination properties of n-GaN.* Solid-State Electronics, 2000. **44**(11): p. 1971-1983.

87. Chernyak, L., et al., *Electron beam-induced increase of electron diffusion length in p-type GaN and AlGaN/GaN superlattices.* Applied Physics Letters, 2000. **77**(6): p. 875-877.

88. Messenger, G.C. and M.S. Ash, *The effects of radiation on electronic systems.* 1986.

89. Kerris, K.G. and S. Gorbics, *Experimental determination of the low-energy spectral component of cobalt-60 sources*. 1986, DTIC Document.

90. Krtschil, A., A. Dadgar, and A. Krost, *Decoration effects as origin of dislocation-related charges in gallium nitride layers investigated by scanning surface potential microscopy.* Applied physics letters, 2003. **82**(14): p. 2263-2265.

91. Kelly, B.T., *Irradiation damage to solids*. 1966: Pergamon Press Oxford.

92. Zhou, Q. and M. Manasreh, *Thermal annealing effect on nitrogen vacancy in proton-irradiated AlxGa1-xN.* Applied physics letters, 2002. **80**: p. 2072.

93. Cahn, J.H., *Irradiation damage in germanium and silicon due to electrons and gamma rays.* Journal of Applied Physics, 1959. **30**(8): p. 1310-1316.

94. Lyubomirsky, I., M. Rabinal, and D. Cahen, *Room-temperature detection of mobile impurities in compound semiconductors by transient ion drift.* Journal of applied physics, 1997. **81**(10): p. 6684-6691.

95. Hogsed, M.R., et al., *Radiation-induced electron traps in Al0. 14Ga0. 86N by 1 MeV electron radiation.* Applied Physics Letters, 2005. **86**(26): p. 1906.

96. Polyakov, A., et al., *Proton implantation effects on electrical and optical properties of undoped AlGaN with high Al mole fraction.* Journal of Vacuum Science & Technology B, 2003. **21**(6): p. 2500-2505.

97. Zhou, Q., et al., *Observation of nitrogen vacancy in proton-irradiated AlxGa1-xN.* Applied Physics Letters, 2001. **79**: p. 2901.

98. Kanaya, K. and S. Okayama, *Penetration and energy-loss theory of electrons in solid targets.* Journal of Physics D: Applied Physics, 1972. **5**(1): p. 43.

99. Ioannou, D.E. and C. Dimitriadis, *A SEM-EBIC minority-carrier diffusion-length measurement technique.* Electron Devices, IEEE Transactions on, 1982. **29**(3): p. 445-450.

100. Zhu, S.-Q., E. Rau, and F.-H. Yang, *A novel method of determining semiconductor parameters in EBIC and SEBIV modes of SEM.* Semiconductor science and technology, 2003. **18**(4): p. 361.

101. Lopatiuk-Tirpak, O., et al., *Studies of minority carrier diffusion length increase in p-type ZnO: Sb.* Journal of applied physics, 2006. **100**(8): p. 086101.

102. Higuchi, H. and H. Tamura, *Measurement of the Lifetime of Minority Carriers in Semiconductors with a Scanning Electron Microscope.* Japanese Journal of Applied Physics, 1965. **4**(4): p. 316.

103. Boersma, J., J. Indenkleef, and H. Kuiken, *A diffusion problem in semiconductor technology.* Journal of engineering mathematics, 1984. **18**(4): p. 315-333.

104. Chan, D.S., V.K. Ong, and J.C. Phang, *A direct method for the extraction of diffusion length and surface recombination velocity from an EBIC line scan: Planar junction configuration.* IEEE transactions on electron devices, 1995. **42**(5): p. 963-968.

105. Schwarz, C., E. Flitsiyan, and L. Chernyak, *Cathodoluminescence Studies of Electron Injection Effects in Wide-Band-Gap Semiconductors*. 2012: INTECH Open Access Publisher.

106. Bhushan, S. and M. Chukichev, *Temperature dependent studies of cathodoluminescence of green band of ZnO crystals.* Journal of materials science letters, 1988. **7**(4): p. 319-321.

107. Schwarz, C., et al., *Gamma irradiation impact on electronic carrier transport in AlGaN/GaN high electron mobility transistors.* Applied Physics Letters, 2013. **102**(6): p. 062102.

108. Yadav, A., et al., *Low and moderate dose gamma-irradiation and annealing impact on electronic and electrical properties of AlGaN/GaN high electron mobility transistors.* Radiation Effects and Defects in Solids, 2015(ahead-of-print): p. 1-9.

109. Yadav, A., et al. *Impact of low dose gamma irradiation on electronic carrier transport in AlGaN/GaN High Electron Mobility Transistors*. in *MRS Proceedings*. 2015. Cambridge Univ Press.

110. Yadav, A., et al., *Cathodoluminescence Studies of Gamma-Irradiation Effects on AlGaN/GaN High Electron Mobility Transistors (HEMTs).* ECS Transactions, 2015. **69**(14): p. 137-144.

111. Chernyak, L., et al., *Electron beam induced current measurements of minority carrier diffusion length in gallium nitride.* Applied physics letters, 1996. **69**(17): p. 2531-2533.

112. Burdett, W., et al., *Impact of aluminum concentration and magnesium doping on the effect of electron injection in p-Al x Ga 1− x N.* Solid-State Electronics, 2003. **47**(5): p. 931-935.

113. Chernyak, L., et al., *Electron beam and optical depth profiling of quasibulk GaN.* Applied Physics Letters, 2000. **77**(17): p. 2695-2697.

114. Prall, C., et al., *Photoluminescence from GaN layers at high temperatures as a candidate for in situ monitoring in MOVPE.* Journal of Crystal Growth, 2014. **397**: p. 24-28.

115. O'Donnell, K. and X. Chen, *Temperature dependence of semiconductor band gaps.* Applied Physics Letters, 1991. **58**(25): p. 2924-2926.

116. Monemar, B., *Fundamental energy gap of GaN from photoluminescence excitation spectra.* Physical Review B, 1974. **10**(2): p. 676.

117. Kumakura, K., et al., *Minority carrier diffusion length in GaN: Dislocation density and doping concentration dependence.* Applied Physics Letters, 2005. **86**: p. 052105.